Stark-shift microscopy: interaction of a confined electric field with single emitters

von

Senta Miriam Karotke
aus Göttingen, Deutschland

Institut für Physik
Universität Basel

UNI
BASEL

Basel, 2006

Genehmigt von der Philosophisch-Naturwissenschaftlichen Fakultät auf Antrag von:

Prof. Dr. H. Güntherodt
Prof. Dr. B. Hecht
Prof. Dr. A. Meixner

Basel, den 13. März 2006

Prof. Dr. H.-J. Wirz, Dekan

Acknowledgments

I would like to take the opportunity to thank all the people who contributed to my Ph.D. work.

First of all, I am grateful to my supervisor Prof. B. Hecht for giving me the opportunity to do my Ph.D. work in his group at the University Basel. I also thank Prof. H.-J. Güntherodt and Prof. A. Meixner for accepting to be the co-referees for this work.

Special thanks goes to Andreas Lieb for his support in many ways. He devoted plenty of his time for stimulating discussions and always lent a hand when problems in the lab appeared.

I also would like to give my thanks to Jacqueline Y. P. Butter. Throughout this work, we struggled together through many problems in the lab and I was always grateful for her helping hand. I probably never forget the hours we have spent together in adjusting our laser. Many thanks goes to the Nano-Optics group, for many fruitful discussions and for their patient help in man-power for repairing our helium cryostat. I would like to name in person Prof. D. Pohl, Julien Toquant and Hans Eisler and acknowledge their help.

I should not miss the opportunity to mention the electronic workshop, especially Andreas Tonin and H.-R. Hidbert. Many thanks for their patient support of repairing burned-out amplifiers. A kind help for many technical problems I obtained from the mechanical workshop. Special thanks goes to Werner Roth, the good soul of the helium liquefier: he was to any time of the day full of ideas for any kind of technical questions concerning vacuum problems or unplanned orders of cooling liquids.

Many thanks goes to Prof. Schönenberger and his group. I am grateful for the opportunity to use the SEM facilities and for many helpful discussions.

For an enjoyable time during the experimental preparations for the Physics Lectures, I thank Stephan Messmer, Christian Wattinger, Jürg Furer and Zheng Ming Wu. I will never forget the hour-lasting search for lost charges in electrostatic setups or the endless adjustments of any kind of physical experiments.

Abstract

Certain fluorescent molecules doped into crystalline matrices at cryogenic temperature exhibit very narrow zero-phonon absorption lines. The homogeneous broadening of the ensemble of molecules in a matrix allows to address individual molecules by means of a narrow-band tunable laser. The extreme sharpness of the zero-phonon lines allows the sensitive detection of minute spectral changes. The linear or quadratic Stark shift of a molecule's zero-phonon line in presence of an electric field can be used to externally tune the molecule's transition frequency. Since the Stark shift depends on the electric field strength at the molecule's position, inhomogeneous electric fields, e.g. in the vicinity of sharp tips, lead to Stark shifts that depend on the relative spatial position of tip and molecule. As a consequence, the transition frequency of single molecules can be tuned over a wide range by nanometer precise positioning of a biased tip with respect to the molecule. If the laser frequency is kept fixed, a molecule may be pushed into resonance by appropriate positioning of the biased tip.

The work presents a theoretical model to explain the fluorescence pattern as a function of tip position depending on the Stark-shift characteristics of the molecule and on the orientation of the permanent dipole moment difference $\Delta\vec{\mu}$. Furthermore, the interaction of the observed molecule with other molecules or with a two-level system can be detected as a distinct feature in the fluorescence pattern. Experimental data of Stark-shift images on single and on several molecules are presented and compared to the theoretical predictions. The experimental setup consists of a sample-scanning confocal microscope combined with a scanning tip setup operating at cryogenic temperature. The sample consists of single crystals of a matric of p-terphenyl and a fluorescent dye of terrylene. We show that the characteristic fluorescence patterns, obtained as a function of tip position, to a first approximation are circles with a molecule at their origins. It is shown, how the optical resonance of a single molecule can be manipulated by scanning the tip and by changing the parameter settings, such as e.g. the tip-voltage or the detuning. The interaction of a single molecule with a two-level system in the matrix has been directly imaged. The interaction causes a splitting of the fluorescence pattern at the position of the two-level system. Multiple circles can be used to determine the position of nearby molecules. We achieve a precision of position determination of about 50 nm in a single scan, albeit unperturbed molecular resonance frequencies differ considerably and the gap-width is around 3 μm.

Contents

Chapter 1

Introduction

The era of single-molecule detection started with the pioneering experiments by Moerner [1] and Orrit [2]. The optical detection of single molecules at the molecular scale opened a door to a wide-range of research activities in different fields, such as investigations of the resonance line-shape of molecules [3] or of biological processes [4, 5]. These examples underline the great advantage of single-molecule detection: the fluorescence signal of single molecules allows a non-destructive way of observation and molecules are local reporters on the nano-scale *inside* the sample of interest. Scanning probes technique, such as scanning tunneling microscopy (STM) [6] or atomic force microscopy (AFM) [7], have also successfully explored single atoms and molecules, but they are limited to surface investigations. Single-molecule detection techniques, such as excitation spectroscopy, give fascinating insights into the quantum world by removing the ensemble averaging. Only by measuring the response of molecules one by one, the observation of stochastic effects, e.g. quantum jumps [8], imaging of spectral diffusion [9], or the investigation of resonance line-shapes [10] has been possible. Investigation of many single systems results in a distribution, which contains more information than the averaged value alone.

At cryogenic temperatures single molecules embedded in a crystalline matrix are very photostable. The fluorescence signal of a single molecule has been observed on the time scale of hours, allowing extended experiments in time to be done with one and the same single quantum system. The line width of the zero-phonon line (ZPL) of a single molecule is determined by the lifetime of its first excited state and by the strength of the electron-phonon coupling to the matrix. At cryogenic temperature, many of the dynamic processes are frozen out. The molecule can therefore be approximated by a two-level quantum system with a nearly lifetime limited line-width of the ZPL [11, 12]. The narrow ZPL reacts very sensitively to changes in the nearby environment, which makes the single molecule a local reporter of changes in its surroundings. Experiments have been performed to investigate matrix-induced effects, such as spectral diffusion or orientational flips of molecules [3, 10, 13], tip-induced dynamics [14] and coupling effects [15], by making use of the sensitivity of the ZPL to its nano-environment.

The Stark effect of single molecules embedded in a solid matrix has been demonstrated quite early in the era of single-molecule spectroscopy [16], followed by a large variety of experimental works [17, 18, 19]. The tip-induced Stark-shift [20] has been used, e.g. to investigate and manipulate the spectral dynamics of single molecules [14]. Furthermore, the orientation of molecules embedded in a solid matrix has been explored with the help of the Stark effect [21]. Stark effect occurs due to the interaction of an electric field with the molecule, which results in a shift of the molecular energy levels. This level shift causes a shift of the transition frequency of the zero-phonon line. Depending on the geometry of the molecule, a linear shift due to a permanent dipole moment $\Delta\vec{\mu}$ [17], or a quadratic shift due to the polarizability $\Delta\tilde{\alpha}$ [22] is observed. Even higher order Stark effects of single molecules have been detected [23]. The Stark shift of a molecule's zero-phonon line in the presence of an electric field can be used to externally tune the molecule's transition frequency [15, 22].

In today's world of nano-science with its decreasing dimensions of devices, it becomes increasingly important to develop new techniques to investigate and to interact with these devices on the same scale [15, 24]. The dimensions of these devices have already reached the molecular and atomic scale, thus entering the domain where observable quantum processes take place. Single-molecule detection and manipulation offers a fascinating potential to contribute to the basic understanding of such quantum processes, and they fill a gap in experimental techniques, which explore effects on the nano-scale.

The goal of this thesis is to develop a new technique for the the manipulation and the detection of single molecules and their optical properties. The new method, which we call Stark-shift microscopy, offers the unique possibility to control the dynamics of single molecules and their interaction on the nanometer scale. Stark-shift microscopy is performed combining fluorescence excitation spectroscopy for single-molecule detection and the perturbation of the molecular resonance by an externally controlled, inhomogeneous electric field of a sharp, metallized tip. The extreme sharpness of the zero-phonon lines at cryogenic temperature allows the sensitive detection of minute spectral changes in the order of a few MHz [25]. Since the Stark shift depends on the electric field strength at the molecule's position, inhomogeneous electric fields in the vicinity of sharp tips, lead to Stark shifts that depend on the relative spatial position of tip and molecule. As a consequence, the transition frequency of single molecules can be tuned over a wide range by nanometer precise positioning of a biased tip with respect to the molecule. Stark-shift microscopy combines the spatial information gained from the tip scan with the spectral information obtained from the tip-induced Stark shift.

The principle of Stark-shift microscopy is sketched in Fig. 1.1 and explained in
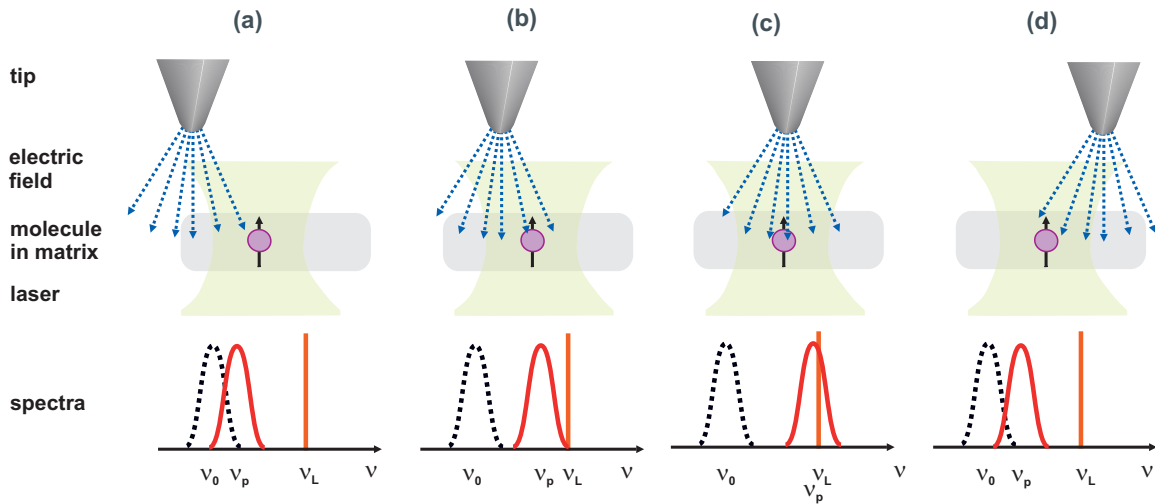
Figure 1.1: Line-scan of the biased tip at a constant height over a single molecule embedded in a solid matrix. The molecule has a certain orientation of the dipole moment and is in the focus of a laser beam, whose frequency is not in resonance with the molecule. The spectra show how the molecular ZPL is tuned into resonance with the laser frequency at certain tip positions. The zero-field resonance of the molecule ν_0 is drawn as a dashed line, the Stark-shifted resonance ν_P is drawn as solid line. The laser frequency ν_L is kept fixed during the tip scan. The Stark shift of the molecule depends strongly on the tip's position. By measuring the fluorescence of the molecule as a function of the tip position, distinct pattern of the fluorescence are expected.

brief in the following. Fig. 1.1 shows a line-scan of a biased tip over a single molecule. The single molecule with a certain dipole orientation is embedded in a solid matrix. An excitation laser, whose frequency is not in resonance with the molecule, is focused on the molecule. A biased metallized tip produces an inhomogeneous electric field with a high field gradient at the position of the nearby molecule. The electric field introduces a Stark shift to the single molecule's ZPL . By scanning the tip at a constant height over the molecule, the electric field strength and electric field orientation at the position of the molecule changes. Hence, the tip-induced Stark shift depends strongly on the tip's position. The spectra in Fig. 1.1 illustrate the principle of Stark-shift microscopy. The zero-field resonance of the molecule is indicated by the dashed peak at ν_0. The excitation frequency ν_L is kept fixed during the tip scan. The field-shifted resonance frequency of the molecule ν_P depends on the tip position. The closer the tip comes to the molecule, the larger the Stark shift. In Fig. 1.1 (c), the tip-induced Stark shift is large enough to push the molecule into resonance with the laser. Obviously, the resonance of the molecule can be tuned in a controlled way by positioning the tip.

We will show that very distinct Stark-shift pattern depending on the relative tip-molecule distance are obtained, by pushing the ZPL in and out of resonance with the laser frequency by a precise positioning of the tip. Molecules with differing resonance frequencies are normally only spatially resolved in several sample scans at

different excitations frequencies. With Stark-shift microscopy, several molecules are resolved in a single spatial tip scan, even though their spectral resonances differ from each other. Such measurements are used for a precise position determination of the molecule. Additionally, interesting effects, caused by the coupling of single molecule to other two-level systems, can be investigated by Stark-shift microscopy.

The thesis is divided into seven chapters. The second chapter presents an overview of the fundamentals of single-molecule spectroscopy and focusses on the low temperatures properties of single molecules. An introduction of the Stark effect of single molecules is given. The interaction between single molecules by dipole-dipole coupling and the interaction between a single molecule and a tunneling two-level-system in the matrix is discussed. Finally, the experimental principles of a confocal microscope, the positioning abilities by piezoelectric elements and the shear-force gap-width control will be introduced.

The third chapter gives an introduction to the sample system, the experimental setup and its imaging capabilities. The sample system is a crystalline matrix of p-terphenyl doped with fluorescent terrylene molecules. The sample properties and the preparation techniques is reviewed. The setup, a confocal microscope combined with a scanning-tip unit, is briefly introduced. The preparation of the etched, metallized glass-fibers as well as the cryogenic setup will be described. An overview of the different modes of operation of the setup is given.

The fourth chapter introduces a theoretical model for Stark-shift microscopy. The chapter presents calculations of the electric fields produced by a tip modelled either as a sphere or as a truncated cone. With the known electric field distribution, the Stark shift depending on the tip position is calculated. These results are used to simulate the Stark-shift pattern depending on the tip position applying the density matrix approach. A theoretical discussion is presented, concerning the influence of different Stark-shift coefficients $\Delta\vec{\mu}$ and $\Delta\tilde{\alpha}$ on the Stark-shift patterns. The chapter concludes with the investigations of additional effects, such as the dipole-dipole coupling or the coupling to a two-level system in the matrix.

The fifth chapter concentrates on the performance of the experimental measurements. The first section gives an theoretical overview of the influence of the different experimental parameters, such as the tip voltage, the gap-width or the detuning. The second section presents an experimental protocol, which we call the five-points measurement, for the determination of suitable parameter settings. The third sections describes an experimental procedure for imaging single molecules by Stark-shift microscopy.

The sixth chapter presents the experimental results. Recorded Stark-shift patterns of single molecules are compared to the theoretical predictions. In the first

part, the influence of the tip voltage and the detuning between the laser frequency and the molecule's resonance on the fluorescent pattern is demonstrated. The second section shows the dependence of the Stark-shift patterns on the gap-width and the orientation of the permanent dipole difference $\Delta\vec{\mu}$. We present the results on the interaction between a single molecule and a tunnelling two-level system of the matrix. The last section then demonstrates the precise position determination of several molecules in a single spatial tip scan.

The seventh and last chapter summarizes the experimental and theoretical results and gives an outlook of future experiments and applications.

Chapter 2

Basics

In this chapter, an introduction of the physical and the technical side of the experimental work of this thesis will be given. The first part is about the fundamentals of single-molecule spectroscopy. This section gives a short summary of the characteristics of single molecules embedded in a solid matrix and the detection at low temperature. Further readings and a detailed introduction can be found in the books on single-molecule detection at low temperature [25] and on nano-optics [26]. Several review papers on single molecule detection give also an overview of the research field [1, 2, 12, 27, 28, 29, 30, 31, 32]. The second section is about the Stark effect of single molecules, which is caused by the interaction of an static electric field with single molecules. The third section introduces the dipole dipole coupling between single emitters. The fourth section discusses the model of a tunnelling two-level system. The chapter is concluded with an introduction of the technical basics, such as the principle of the confocal microscope, the use of piezoelectric elements as positioning elements and the gap-width control by a tuning fork.

2.1 Fundamentals of single-molecule spectroscopy

The investigation of single molecules by fluorescence excitation spectroscopy covers by now a wide range from bio-physics [4] to quantum optics [11]. This alone wide application range shows already how powerful and how flexible this technique is. Single molecules give us not only the possibility to study single quantum systems, but also to have a look into processes inside the sample, such as the flipping of molecular groups in a solid matrix or transport processes through a cell membrane. To understand such processes, the characteristic behavior of single molecules in different environments and the influence of the nearby surrounding on the molecule have been investigated [13, 33]. The basic principle of fluorescence excitation spectroscopy
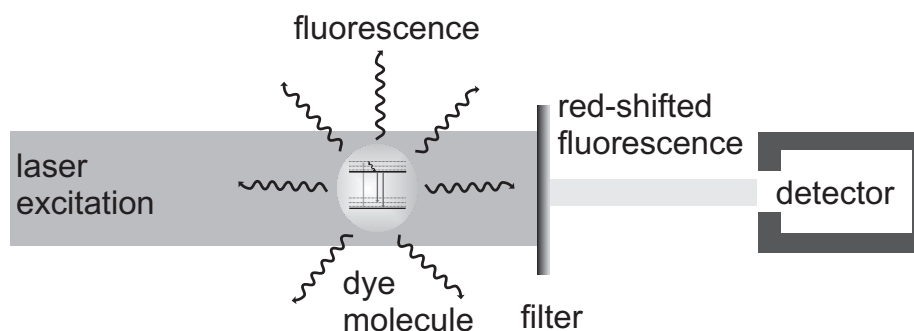
Figure 2.1: Simplified scheme of single molecule spectroscopy: A laser excites a single molecule. By blocking the excitation light by a filter, the fluorescent signal of the molecule can be detected and analyzed by a detector, such as a single-photon counting photo diode, for example.

is sketched in Fig. 2.1. A laser beam is focussed onto a a sample, where the light interacts with a single molecule. If the laser is in resonance with the molecule, the molecule is excited from its ground state to the first excited state. The molecule falls back to its ground state by emitting a photon. This fluorescent signal is then detected by a single photon counting detector. A filter is used to distinguish the fluorescence of the molecule from the excitation laser light. The detector detects only the red-shifted fluorescence. By scanning the laser in frequency, molecules which are in resonance with the laser, can be detected and resolved spectrally in an excitation spectrum. Hence, an excitation spectrum displays the fluorescence of the single molecules as a function of the excitation wavelength.

Even though, the principle of single molecule fluorescence detection seems to be very simple, there are certain requirements for the sample system and the setup, which have to be satisfied. In the following section, an overview of these requirements will be given.

2.1.1 A single molecule embedded in a solid matrix

Dye molecules embedded in a solid matrix were found to be a preferred sample system for single-molecule spectroscopy (SMS). In the optimum case, the solid matrix is a single crystal. Single molecules act very sensitive to their surroundings. By embedding molecules in a crystalline matrix, it is expected that the molecule shows a spectrally stable behavior. Single chromophores in a solid matrix have very distinct properties which are presented in the following.

Energy level scheme

The characteristics of the absorption spectrum of a single molecule embedded in a solid matrix and other photo-physical processes can be explained with the help of a Jablonski diagram, sketched in Fig. 2.2 (a). In this diagram, the electronic energy

levels of the ground state S_0 and the first excited state S_1 of a single molecule are shown. The scheme also shows the vibrational levels of each electronic energy level. Finally, the level, named T_1, is the triplet state.

By absorbing a photon, a transition from the ground state S_0 to the vibrational ground state (resonant excitation) or to the vibrational levels (non-resonant excitation) of the first excited state S_1 is possible. If the excitation into the vibrational levels of S_1 occurs, a relaxation to the vibrational ground state of the excited state is required before a photon can be emitted. The relaxation into the ground state of S_1 is a non-radiative process. A non-radiative process dissipates the energy into phonons and does not emit a photon. This non-radiative process is called internal conversion (IC) and is marked by a wiggling line in Fig. 2.2 (a). The lifetime of the first excited state S_1 of dye molecules can vary between 1 and 10 ns.

There are several pathways from the vibrational ground state of the first excited state to the ground state of the molecule. One path is by emitting a photon and undergoing a transition into the vibrational states of the ground state S_0. This transition results in the red-shifted fluorescence of the molecule. Relaxation from the vibrational levels to the vibrational ground state of S_0 occurs by internal conversion. The direct transition from the vibrational ground state of S_1 to the vibrational ground state of S_0 occurs by emitting a photon with the same frequency of the exciting photon. This transition is a zero-phonon transition. Another path is the relaxation by internal conversion from the vibrational ground state of S_1 into the vibrational ground state of S_0. This is a non-radiative process and no photon is emitted. The third path is a transition to the triplet state T_1. This transition is called inter-system crossing (ISC), where no photon is emitted. Undergoing an inter-system crossing is linked to a spin flip, where the orientation of the spin is reversed. After relaxation into the vibrational ground state of T_1, a transition can occur into the ground state S_0 of the molecule by another inter-system crossing. Since the transition from T_1 to S_0 is spin forbidden, the lifetime of the triplet state is very long and can reach a timescale of ms.

For describing the emission rate of a single molecule, a new parameter is introduced, which is called the the quantum yield Φ. The quantum yield describes the ratio of the radiative and the non-radiative part of the emission:

$$\Phi = \frac{k_r}{k_r + k_{nr}}. \tag{2.1}$$

The rate k_r takes all radiative rates into account, and k_{nr} all non-radiative rates. If the quantum yield is large, the molecule is a good candidate for excitation spectroscopy, since it supplies a large emission signal.
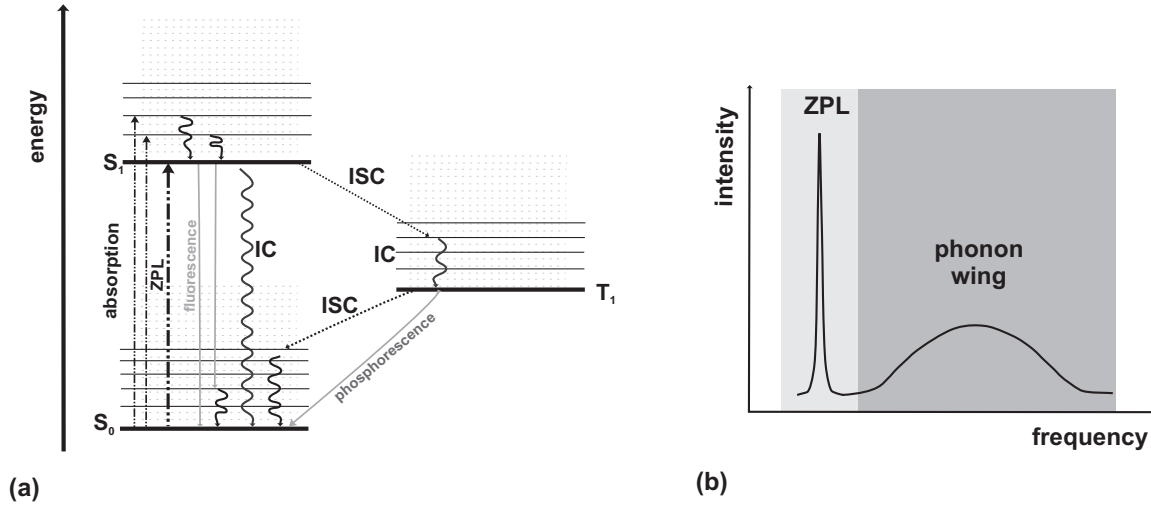
Figure 2.2: (a) Energy levels of the electronic ground state (S_0), the first excited state (S_1) and the triplet state (T_1): the Jablonski diagram. (b) Spectrum of a single molecule showing the zero-phonon line (ZPL) and the phonon wing (PW) for low temperature.

Zero-Phonon line and the phonon-wing

The absorption spectrum of a single molecule is shown in Fig. 2.2 (b). The appearance of the spectrum can be explained with the help of the Jablonski diagram. As can be seen in Fig. 2.2 (a), there are not only electronic levels in the energy level diagram. Each electronic level exhibit also vibronic levels, which appear due to vibration of the molecule and of the surrounding matrix. These transitions contribute to different features in the spectrum. The pure electronic transition without any coupling to phonons results in the zero-phonon line (ZPL), as sketched in Fig. 2.2 (b). Due to the interaction with the phonons, a second band, shifted to the blue, appears, which is called the phonon wing (PW). The respective states have very short lifetimes, which results in very broad, overlapping peaks forming the PW.

At room temperature, there are many phonons in the matrix, and the PW becomes very broad and overlaps with the ZPL. By cooling down to cryogenic temperature, the low energy excitations are frozen out. The ZPL becomes more intense and very narrow and is finally separated from the PW ($T < 20$ K).

Absorption line shape of a single molecule

The line shape of the ZPL of a single molecule embedded in a matrix can be described by a Lorentzian:

$$I(\nu_L) = \frac{\Gamma \nu_R^2}{(2\nu_R^2 + 4(\nu_L - \nu_0)^2 + \Gamma^2)}. \tag{2.2}$$

where ν_L is the excitation frequency, Γ is the homogeneous line width, ν_R is the Rabi-frequency, and ν_0 is the resonance frequency of the molecule. The equation (2.2) is
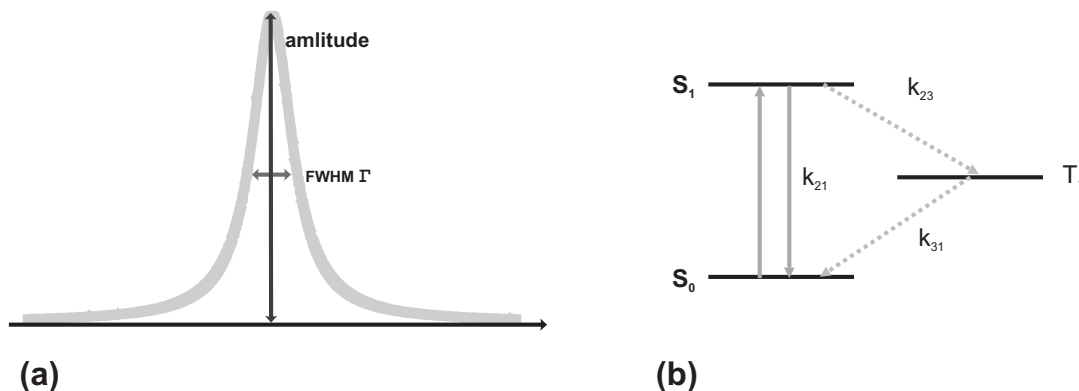
Figure 2.3: (a) ZPL of a single molecule can be described by a Lorentzian line shape at low temperature. (b) Simplified energy level diagram without the vibrational levels, where $k_{i,j}$ indicates the rates between the different states.

derived from the master equation approach of a single emitter coupled to a laser field, including the spontaneous emission. No interaction with a phonon bath is considered. Hence, the Lorentzian line shape is valid only at low temperature. A derivation of this formula is given in Chapter 4.3. In Fig. 2.3 (a) and (b), a Lorentzian line profile is shown with a simplified energy level scheme valid at low temperature. The homogeneous line width Γ is the full width at half maximum (FWHM) of the peak. The line width is directly related to the lifetime of the excited state:

$$\Gamma = \frac{1}{\pi T_2} = \frac{1}{2\pi T_1} + \frac{1}{\pi T_2^*}, \tag{2.3}$$

where T_2 is the overall dephasing time, which is divided in two contributions T_1 and T_2^*. The time T_1 is the lifetime of the first excited state S_1. The time T_2^* is the pure dephasing time. T_2^* depends very strongly on low frequency excitations, such as phonons, for example. At low temperature phonons are frozen out and $T_2^* \rightarrow \infty$. The $\frac{1}{\pi T_2^*}$-term in Eq. (2.3) can be neglected at low temperature ($T < 2K$) and the line width Γ of a single molecule embedded in a solid matrix becomes lifetime-limited [34].

Absorption cross section

The molecule has to absorb a photon to make a transition into the excited state. The absorption of a photon occurs with a certain probability. A primitive picture to describe the probability of absorbing a photon, is to define a virtual area around the molecule, where every passing photon is absorbed. This virtual area is called the absorption cross section σ (ACS). A more sophisticated description, based on a classical picture, can be found in [26], where the ACS is defined as the area where the energy flow between an incoming plane wave and a dipole field of an emitter, is directed towards the emitter. The absorption cross section can be expressed as
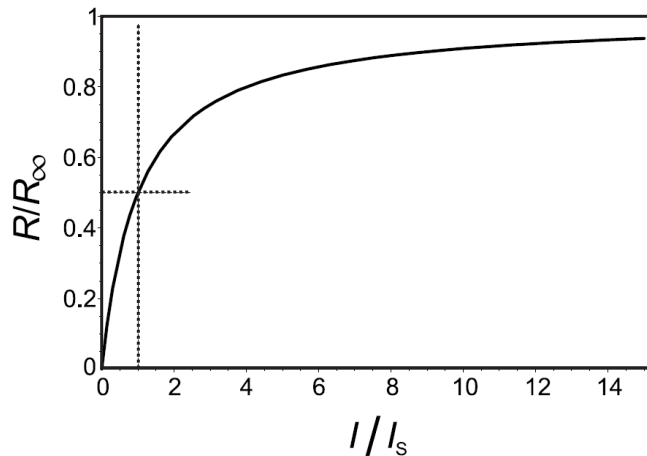
Figure 2.4: Saturation of an optical transition: the emission rate of photons R saturates at a certain threshold, indicated by the dashed lines [26].

[35, 36]:

$$\sigma = c_{DW} c_{FC} 3 \cos^3(\phi) \frac{\lambda^2}{2\pi} \Phi, \tag{2.4}$$

where c_{DW} is the Debey-Waller factor, c_{FC} is the Franck-Condon factor, the term $\cos(\phi)$ describes the orientation of the excitation light and the transition dipole of the molecule, λ is the excitation wave length and Φ is the quantum yield.

The Debey-Waller factor c_{DW} is proportional to the inverse of the electron-phonon coupling, which depends on the temperature:

$$c_{DW} = \frac{I_{ZPL}}{I_{ZPL} + I_{PW}}, \tag{2.5}$$

where I_{ZPL} and I_{PW} are the intensities for the zero-phonon line and the phonon wing, respectively. At increasing temperature ($T \geq 20$ K), when the coupling to the phonons increases, the intensity goes to the PW, and the ZPL disappears. Hence, the Debey-Waller factor also decreases. This factor limits the absorption cross section at higher temperature.

The Franck-Condon factor c_{FC} describes the overlap of the wavefunction of the vibronic levels of the ground and first excited state. A transition is more likely (shows a stronger intensity), if the overlap is large [37]. At low temperature, the overlap of the wavefunctions of the vibrational ground states of the electronic ground state and of the electronic first excited state is larger compared to the higher vibrational levels of these states [38]. This gives rise to a very sharp and intense zero-phonon line.

Saturation

Up a certain excitation intensity threshold, the increase in excitation power results only in an increase in the population of the triplet state. Hence, the emission rate of photons cannot exceed a certain value, see Fig. 2.4. This effect is called saturation. The saturation can be described by the following equation for the emission rate R:

$$R(I) = R_\infty \frac{I/I_S}{1 + I/I_S}, \tag{2.6}$$

where R_∞ is the saturation count rate at infinite strong excitation, I is the excitation intensity and I_S is the saturation intensity at which $R = R_\infty/2$. The two constants R_∞ and I_S can be expressed as follows [26]:

$$R_\infty = \frac{k_{31} k_r}{k_{23} + k_{31}}, \tag{2.7}$$

$$I_S = \frac{(k_r + k_{nr} + k_{23}) k_{31}}{(k_{23} + k_{31}) \sigma}, \tag{2.8}$$

where k_r, k_{nr} are the radiative and the non-radiative decay rate, respectively, σ is the absorption cross section and k_{ij} are the decay rates for the transition as shown in Fig. 2.3 (b). For further information are given in [22, 26].

Increasing the excitation power of the laser leads also to another effect, the broadening of the line width of the resonance. This effect is called power broadening of the ZPL. Power broadening appears, if the saturation of the transition is reached [39]. The dependence of the line width of the ZPL on the excitation power can be expressed as:

$$\Gamma(I) = \Gamma_0 \sqrt{1 + I/I_S}, \tag{2.9}$$

where Γ is the homogeneous line width and Γ_0 is the line width at $I \to 0$.

Finally, also the absorption cross section σ depends on the intensity. The dependence on the excitation intensity can be expressed as :

$$\sigma(I) = \frac{\sigma_0}{1 + I/I_S}, \tag{2.10}$$

with σ_0 as the absorption cross section for $I \to 0$. The absorption cross section is therefore decreased by any finite laser intensity.

2.1.2 Detection of single molecules at cryogenic temperature

The zero-phonon lines of molecules become very narrow at cryogenic temperature and they can be addressed individually by a narrow-band laser. For excitation spectroscopy of single molecules at low temperature, spatial selection and spectral selection are used for single-molecule detection.
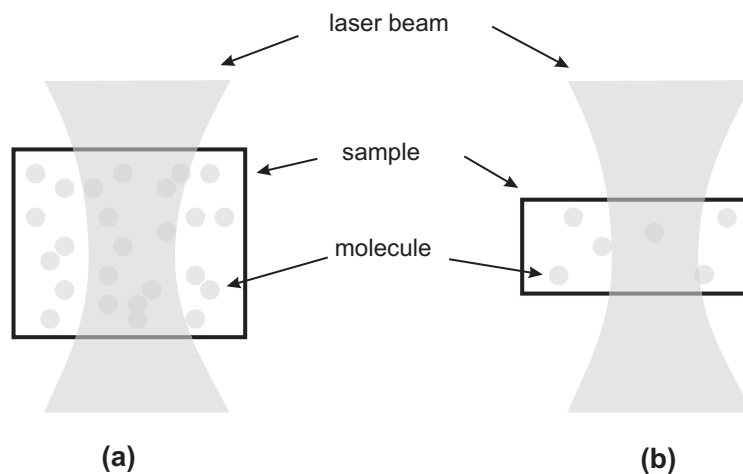
Figure 2.5: Illustration of the spatial selection of single molecules. (a) The thicker the sample and the higher the concentration of molecules, the higher is the possibility to excite several molecules. (b) Reducing the concentration of the fluorophores and the thickness of the sample, as well as focussing the laser on a very small volume, makes the spatial selection of single molecules possible

Spatial selection

Single-molecule detection depends very strongly on the concentration of the molecules in the detection volume. The more molecules are located within the excitation volume, the higher the possibility to excite several molecules, see Fig. 2.5 (a). By reducing the number of molecules in the host matrix, detection of single molecules is facilitated. A second way of reducing the number of molecules in the excitation area is to reduce the excitation volume itself. This can be done by using very thin samples and focussing the laser to a very small volume inside the sample. The method of spatial selection is illustrated in Fig. 2.5.

Spectral selection

Single molecules of the same kind, embedded in a low concentration in a crystalline matrix should show the same transition frequency. A crystalline structure provides a well-defined, homogeneous environment. But no crystal is perfect. The environment in the matrix varies between different locations due to defects such as, e.g. grain boundaries as shown in Fig. 2.6 (a). Therefore, molecules have different surroundings, which results in an shift of their resonance frequencies due to the interaction with the host crystal. This effect leads to inhomogeneous broadening of the ensemble absorption band [40, 41, 42], as shown in Fig. 2.6 (b). The inhomogeneous broadening is therefore produced by a superposition of many individual homogeneous absorption profiles. By reducing the number of molecules, a 'spectral roughness' of the inhomogeneous line can be detected, which is called statistical fine structure [43, 44].
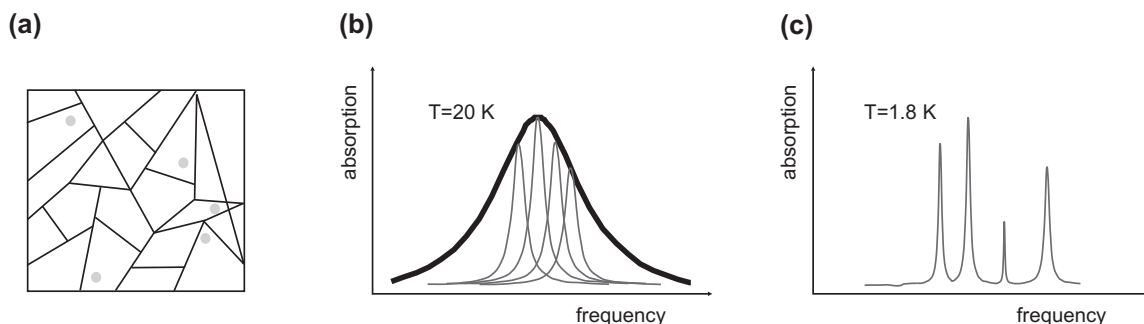
Figure 2.6: (a) Single fluorescent molecules in solid matrix. Since every molecule has a slightly different environment, the transition frequencies differ. The absorption band is inhomogeneous broadened. (b) At higher temperature ($T > 20$ K) the individual resonances of the molecules overlap and form a single absorption band, which is called the inhomogeneous broadened line. (c) At cryogenic temperature, the line width of the ZPL become so narrow, that single peaks can be detected.

At higher temperature ($T > 20$ K), the line width of the molecular resonance is very broad and the resonance peaks of different molecules overlap. This overlap results in a single absorption band and the molecules cannot be addressed separately. The only way to overcome this problem is to work with very low concentration of the chromophores. Since the distribution of the transition frequencies is not homogeneous, the spectral distance between the different ZPL becomes larger at the wings of the inhomogeneous line. Exciting molecules, which are spectrally located at the wings of the inhomogeneous line, simplifies the single excitation as well. At cryogenic temperature, the line widths of the molecules become very narrow. The overlap of the ZPL is much less, but the variety of the transition frequencies is still there. The molecules can be addressed more easily one after the other as shown in Fig. 2.6 (c). Therefore, inhomogeneous broadening allows a spectral selection of single molecules.

Conditions for single-molecules spectroscopy

Molecules embedded in a solid have to satisfy several requirements, to be suitable for single-molecule spectroscopy. These requirements, even though most of them have already been mentioned in the previous discussion, are summarized in the following.

For the detection of single molecules, it has to be assured to have only one molecule in focus and to have a fluorescence signal of the molecule above noise level. Having only one molecule in focus can be done by diluting the sample and reducing the volume (spatial selection) and exciting in the wings of the inhomogeneous line (spectral selection). A high fluorescence signal is determined by several requirements, which can be deduced from Eq. (2.3) for the line width Γ and from Eq. (2.1) for the quantum yield Φ, respectively:

- Stability of the fluorescent signal can be increased by working with single molecules embedded in a crystalline matrix. Choosing a dye-matrix system, where the molecule fits into the crystal lattice without too many distortion, is preferable.

- An intense peak of the ZPL is obtained if the quantum yield $\Phi \approx 1$. Therefore the sample should have a large radiative rate and a low non-radiative rate.

- A narrow peak of the ZPL is obtained in the case of a long lifetime of the first excited state T_1 and for $T_2^* \rightarrow 0$ for low temperature. The excitation intensity should also lie below the saturation to avoid power broadening.

- A large absorption cross section σ is preferable, since the probability to excite the molecule is larger. The excitation occurs at lower power, which minimizes the background.

- The sample system should have a slow inter-system crossing rate k_{23} and a short triplet lifetime to weaken the triplet bottleneck.

Bunching, blinking, bleaching, spectral diffusion - photophysics

There are photo-physical processes, which have not been discussed until now. They are not subject of the thesis, but they appear in one way or the other in the experimental measurements. Therefore, a quick overview is given in the following.

anti-bunching The molecule has to be excited before it can emit a photon. Since the re-excitation depends on the lifetime of the excited state, there is a time period of the molecule where it cannot emit a photon. Therefore, the bright period of a molecule consists of a series of single photons spaced out in time by the lifetime of he excited state in average [45]. This effect is called anti-bunching, sketched in Fig. 2.7.

bunching Another effect is related to the inter-system crossing into the triplet state. Since the triplet state has a comparable long lifetime, the molecule can be get trapped there and does not emit any photons. This trapping causes a dark period in the emission of the molecule. This effect causes a 'binning' of emitted photons, which is called bunching, sketched in Fig. 2.7

photo-bleaching If the molecule stops to fluoresce, the effect is called photo-bleaching. The exact mechanism is not known, but the effect is attributed to chemical modifications. The molecule might undergo some chemical reaction with other molecules or the environment, as for example with oxygen.

Figure 2.7: Single fluorescent molecules emit photons only after they have been excited, which causes anti-bunching of the emitted photons. By crossing over into the triplet state, the molecule exhibits some dark periods without emitting photons. This effect causes some kind of 'binning' of the photons, which is called bunching.

'blinking' and 'spectral diffusion' In experimental measurements, the fluorescence pattern of a single molecule can be interrupted by dark periods. This effect is called the fluorescent blinking. The time scale of the event is in the ms-range. Spectral diffusion of a single molecule is linked to processes in the host-matrix. Due to changes in the nearby surrounding, the frequency of the ZPL can shift spectrally [3]. This effect is called spectral diffusion. The shift of the molecule can occur slowly as a kind of creeping behavior, or it can occur as a sudden jump towards another spectral position.

2.2 Perturbation by an electric field: the Stark effect

The optical transition frequency of a single molecule depends on the spacing of the energy level. By changing the spacing of the energy levels, the ZPL frequency can be tuned. Control of the energy spacing can be achieved, e.g., by an additional, external electric field. The shift of the resonance frequency due to an electric field is called Stark effect. The Stark shift of the ZPL of single molecules has been demonstrated in the 90' by Wild et al. [22] and has found some interesting application since then [15]. The interest in Stark-shift characteristics is also increasing in connection to quantum dots with the intension to use the effect quantum computing.

2.2.1 Single molecule and a static electric field

At low temperature, the complex Jablonski-diagram of a single molecule can be reduced to a two-level system with a ground state G and a first excited state F, as shown in Fig. 2.3 (b). By applying an external electric field, the energy levels can be shifted as shown in Fig. 2.8 (a). The change of the spacing of the ground state and the first excited state, results in an induced Stark shift $\Delta\nu_S = \nu_e - \nu_0$, where ν_0 is the zero-field resonance of the molecule and ν_e the field-shifted resonance (Fig. 2.8 (b)). The overall shift can be detected in a spectrum, where the resonance of the molecule
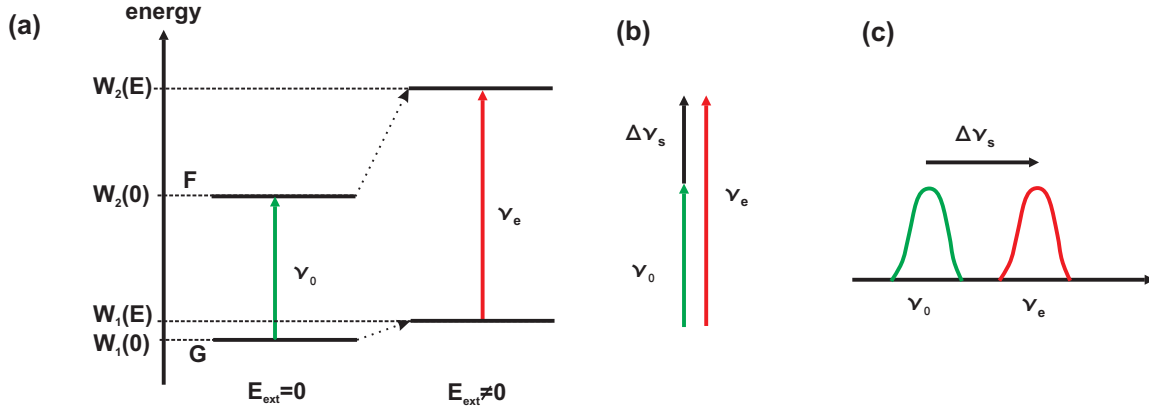
Figure 2.8: Stark shift of a single molecule. (a) Two-level system with G as the ground state and F the first excited state. By applying an electric field E_{ext}, the ground and first energy level are shifted by different values, which results in a different resonance frequency ν_e (b) The overall Stark shift $\Delta\nu_S$ results from subtracting the zero-field resonance frequency ν_0 from the shifted resonance frequency ν_e. (c) The ZPL of a molecule is shifted by $\Delta\nu_S$, which can be observed in the excitation spectrum.

shifts from ν_0 to ν_e due to the interaction with the electric field (Fig. 2.8 (c)).

The electronic energy level W in an electric field can be expressed in a Taylor expansion [25] up to the second order:

$$W_1(E) \;=\; W_1(0) - \vec{\mu}_1 \vec{E} - \frac{1}{2}\vec{E}\tilde{\alpha}_1\vec{E} \tag{2.11}$$

$$W_2(E) \;=\; W_2(0) - \vec{\mu}_2 \vec{E} - \frac{1}{2}\vec{E}\tilde{\alpha}_2\vec{E}. \tag{2.12}$$

Here, (1,2) indicates the ground and the first excited state, respectively, $W_i(E)$ are the energy levels in the electric field (see Fig. 2.8 (a)), $W_i(0)$ are energy levels in zero-field, $\vec{\mu}_i$ and $\tilde{\alpha}_i$ are the permanent dipole moment and the polarizability, respectively. The transition frequencies ν_0 and ν_e can be expressed by the energy difference between the ground G and the first excited state F with the help of Eq. (2.11) and (2.12):

$$\hbar\nu_0 \;=\; W_1(0) - W_2(0) \tag{2.13}$$
$$\hbar\nu_e \;=\; W_1(E) - W_2(0)$$
$$\;=\; W_1(0) - \vec{\mu}_1\vec{E} - \frac{1}{2}\vec{E}\tilde{\alpha}_1\vec{E} - W_2(0) + \vec{\mu}_2\vec{E} + \frac{1}{2}\vec{E}\tilde{\alpha}_2\vec{E} \tag{2.14}$$

As shown in Fig. 2.8 (b), the Stark shift $\Delta\nu_S$ has been defined as the overall shift of the energy levels of the ground and the first excited state. The Stark shift $\Delta\nu_S$ is

obtained up to the first and second order:

$$
\begin{aligned}
\hbar\Delta\nu_S &= \hbar(\nu_e - \nu_0) \tag{2.15} \\
&= W_1(0) - \vec{\mu}_1\vec{E} - \frac{1}{2}\vec{E}\tilde{\alpha}_1\vec{E} - W_2(0) + \vec{\mu}_2\vec{E} + \frac{1}{2}\vec{E}\tilde{\alpha}_2\vec{E} - W_1(0) + W_2(0) \\
&= -\Delta\vec{\mu}\vec{E} - \frac{1}{2}\vec{E}\Delta\tilde{\alpha}\vec{E}. \tag{2.16}
\end{aligned}
$$

Here, $\Delta\vec{\mu} = \vec{\mu}_2 - \vec{\mu}_1$ is the permanent dipole different between the ground and the first excited state, and $\Delta\tilde{\alpha} = \tilde{\alpha}_2 - \tilde{\alpha}_1$ is the difference in polarizability between the ground and the first excited state. The first term in Eq. (2.16) is the linear Stark shift and the second term is the quadratic Stark shift. When plotting the Stark shift versus the electric field, the linear Stark shift is a straight line and the quadratic term is a parabola. The Stark shift of a single molecule depends on the Stark-shift coefficient $\Delta\vec{\mu}$ and $\Delta\tilde{\alpha}$. These two coefficients are defined by the symmetry of the molecule and by the influence of the nearby surrounding of the molecule. The change of permanent dipole moment and of the polarizability can be expressed as:

$$
\Delta\vec{\mu} = |\Delta\mu| \begin{pmatrix} \sin\phi\cos\theta \\ \sin\phi\sin\theta \\ \cos\phi \end{pmatrix} \quad \text{and} \quad \Delta\tilde{\alpha} = \begin{pmatrix} \Delta\alpha_{aa} & \Delta\alpha_{ab} & \Delta\alpha_{ac} \\ \Delta\alpha_{ba} & \Delta\alpha_{bb} & \Delta\alpha_{bc} \\ \Delta\alpha_{ca} & \Delta\alpha_{cb} & \Delta\alpha_{cc} \end{pmatrix}.
$$

Here, $\Delta\vec{\mu}$ is expressed in spherical coordinates, with ϕ as angle with the z-axes and θ as the angle in the (x,y)-plane. The polarizability is a tensor, depending on the geometry of the molecule.

Dipole moment

The linear Stark effect depends on the *permanent* dipole difference between the ground and the first excited state. To make this point perfectly clear, the permanent dipole difference is expressed as:

$$
\Delta\vec{\mu} = \langle g|\vec{\mathbf{d}}|g\rangle - \langle e|\vec{\mathbf{d}}|e\rangle, \tag{2.17}
$$

with the ground state $\langle g|$ and the excited state $\langle e|$ and $\vec{d}$ as the dipole moment.

2.2.2   Matrix and a static electric field

Typically, the molecules that are investigated, are embedded in a solid matrix. What has been discussed so far with respect to the Stark shift is valid for molecules in vacuum. Therefore, the electric field at the position of the molecule is changed by the matrix. The local electric field $\vec{E}_{loc}$ is the electric field at a certain position inside the matrix depending on the externally applied electric field. The influence of the matrix is taken into account by the Lorentz factor f_L. The Lorentz-model averages the electric field over the whole sample and assumes it to be proportional

to an averaged constant f_L [46]:

$$\vec{E}_{loc} = f_L \vec{E}_{ext} = \frac{\epsilon + 2}{3} \vec{E}_{ext}. \tag{2.18}$$

The effect of the matrix is taken into account by the dielectric constant ϵ. If the matrix is anisotropic, the dielectric constant depends on the direction in the crystal and becomes a tensor. There is an additional field inside the matrix, $\vec{E}_{int}$, which is due to the geometry of the matrix molecules and their charges. The internal field can also shift the resonance of the molecule and induces, for example, a permanent dipole moment to the fluorescent molecule. The effect of the internal field can be seen, if the Stark shift of a molecule is not zero under zero-field conditions. The total field $\vec{E}_{tot}$ around the molecules's position is expressed as:

$$\vec{E}_{tot} = \vec{E}_{loc} + \vec{E}_{int}. \tag{2.19}$$

Taking the total field at the position of the molecule into account, the Stark shift can be expressed up to the second order as:

$$\Delta\nu = -\Delta\vec{\mu}\left(f_L \vec{E}_{ext} + \vec{E}_{int}\right) - \frac{1}{2}\left(f_L \vec{E}_{ext} + \vec{E}_{int}\right)\Delta\tilde{\alpha}\left(f_L \vec{E}_{ext} + \vec{E}_{int}\right). \tag{2.20}$$

2.3 Dipole-dipole coupling

Single molecules, which are separated by a distance r_{12} smaller than the excitation wavelength λ, can interact by the electric Coulomb interaction. The requirement for the distance can be expressed as [47]:

$$kr_{12} < 1, \tag{2.21}$$

with $k = \frac{2\pi}{\lambda}$ as the wavenumber. In the following discussion, only two molecules are considered, as shown in Fig. 2.9 (a). They are described by two two-level systems, as sketched in Fig. 2.9 (b). The two single molecules are described by $|a_i\rangle$ and $|b_i\rangle$ with (i=1,2) for the ground and the first excited state, respectively. An additional assumption is, that the wavefunctions of both molecules are only slightly overlapping. With this assumption, the molecules can be treated separately and the interaction term is a small perturbation. The interaction term j can be derived from a classical picture. One of the dipoles oscillates and generates a radiation field. Into this electric field, the second dipole is placed [48]. The interaction is described by:

$$W_{int} = -\vec{\mu}_2 \vec{E}_1, \tag{2.22}$$

where $\vec{\mu}_2$ is the dipole moment of molecule 2 and $\vec{E}_1$ is the electric field of the oscillating dipole of molecule 1. Taking the real part of Eq. (2.22), the dipole-dipole interaction j in Eq. (2.23) is obtained [48]. The dipole-dipole interaction j between
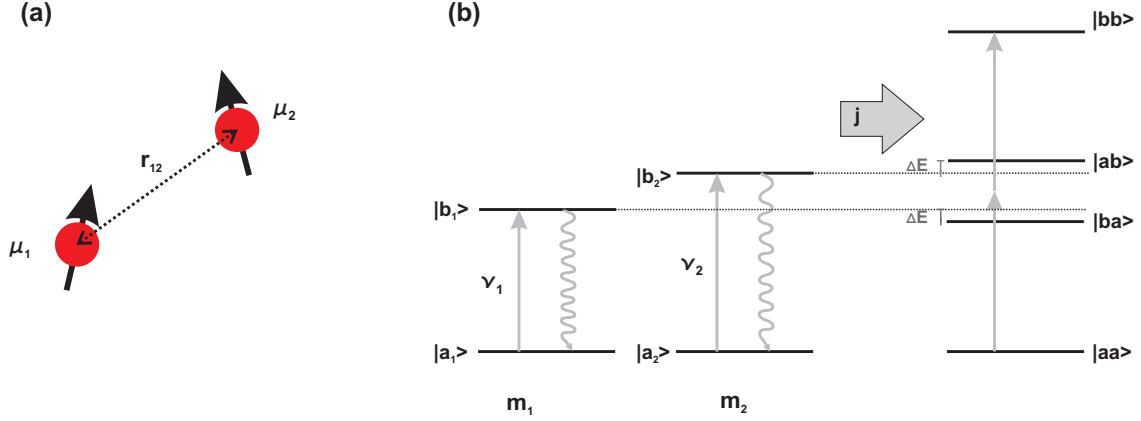
Figure 2.9: (a) Spatial orientation of the two molecules, where r_{12} is the distance between them and μ_i are the dipole moments. (b) Notation for the interaction between two single emitters, with $|a_i\rangle$ as the ground states and $|b_i\rangle$ as the first excited state. By introducing the coupling j to the systems, an additional energy splitting ΔE appears.

two molecules can be written as [49]:

$$j = \frac{3\sqrt{\Gamma_1\Gamma_2}}{4(k_0 r_{12})^3}\left[(\hat{\mu}_1\hat{\mu}_2) - 3(\hat{\mu}_1\hat{r}_{12})(\hat{\mu}_2\hat{r}_{12})\right]. \tag{2.23}$$

Here, Γ_i with $i = 1, 2$ are the line widths of the transitions, $\hat{\mu}_i$ with $i = 1, 2$ are the transition dipole moments and $k_0 = \frac{\nu_1 - \nu_2}{2c}$ is the average wave number with $\nu_{1,2}$ as the transition frequencies of the molecules.

The system of two interacting two-level systems can be transformed into a new eigensystem. The new eigensystem is a single four-level system with an additional energy spacing ΔE, as sketched in Fig. 2.9 (b). In the case of two identical molecules ($\nu_1 = \nu_2$), the additional energy spacing is equal to the dipole-dipole interaction j. Considering two molecules with different transition frequencies, the additional spacing is

$$\Delta E = \pm\sqrt{\Delta\nu_m^2 + j^2}, \tag{2.24}$$

with $\Delta\nu_m = \frac{\nu_2 - \nu_1}{2}$. The new eigenstates of the system are denoted as $|aa\rangle$ and $|bb\rangle$ for the ground and the highest excited state, respectively, and $|ab\rangle$ and $|ba\rangle$. The Hamiltonian of the coupled system in a laser field can be expressed as:

$$H = H_1 + H_2 + H_{int}, \tag{2.25}$$

where H_1 and H_2 describe molecule 1 and 2 in a laser field, respectively, and H_{int} is the dipole-dipole interaction j. The Hamiltonian H_i with $i = (1, 2)$ of a single

molecule in a laser field can be written as

$$H_i = \frac{\hbar \nu_i}{2}(-\sigma_z) - \vec{d}_{egi}\vec{E}\cos(\nu_L t)\sigma_x \qquad (2.26)$$

where

$$\sigma_z = \begin{pmatrix} 1 & 0 \\ 0 & -1 \end{pmatrix} \text{ and } \sigma_x = \begin{pmatrix} 0 & 1 \\ 1 & 0 \end{pmatrix},$$

are the Pauli matrices, ν_i is the resonance frequency of the molecule i, $\vec{d}_{egi}$ is the transition dipole moment of the emitter i, and $\vec{E}$ is the laser field, varying with frequency ν_L. The system can now be described by the time evolution of the density matrix using the Hamiltonian of the complete system of Eq. (2.25):

$$\dot{\rho} = -\frac{1}{\hbar}[H, \rho]. \qquad (2.27)$$

Dipole moment

The coupling of the excitation light of the laser to the molecule is determined by the orientation of the electric laser field $\vec{E}$ and the orientation of the transition dipole moment $\vec{d}_{eg}$, as just derived in Eq. (2.26). If the orientation between $\vec{E}$ and $\vec{d}_{eg}$ is perpendicular to each other, the excitation of the molecule is not possible. Here we point out, that the interaction is based on the *transition* dipole moment $\vec{d}_{eg}$ between the ground and the first excited state, in contrast of the Stark effect, which depends on the permanent dipole moment difference. The dipole moment can be expressed as:

$$\vec{d}_{eg} = \langle g|\vec{\mathbf{d}}|e\rangle, \qquad (2.28)$$

with $\langle g|$, $\langle e|$ as the ground and the first excited state, and $\vec{\mathbf{d}}$ as the dipole operator. This dipole moment has to be distinguished from the dipole moment difference $\Delta\vec{\mu}$ defined in Eq. (2.17).

2.4 Tunnelling two-level system

Optical spectroscopy has been a powerful tool for probing the structure and the dynamics of solids [10, 50, 51]. The local environment has a large influence on the transition frequency of a chromophore. A model to describe the environment of a single molecule in the matrix at low temperature, is the tunnelling two-level system (TLS) [52, 53]. Originally, the TLS model has been developed to describe low-temperature anomalies of glasses [54, 55], such as the anomalous heat capacity. The environment is modelled as double-wells of a potential-energy surface along some collective coordinates of atomic displacements [56]. At low temperature, the energy levels of the double-well potentials are reduced to the two lowest energy eigentates, the TLS. The model also finds application in crystalline matrices and low-temperature glasses [57, 58, 59, 60]. There are a few crystal systems, where the motion of some atomic
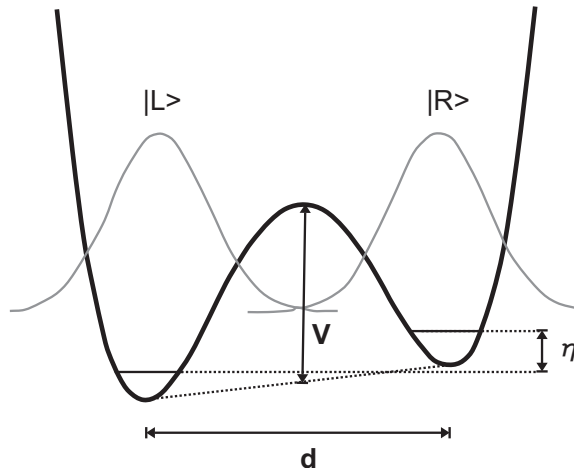
Figure 2.10: Double-well potential of a matrix two-level system, with the two localized basis states $|L\rangle$ and $|R\rangle$.

groups, as e.g. the methyl in p-terphenyl, can take place, even at cryogenic temperature [25]. These methyl groups can flip their orientation due to coupling to low-energy excitations, such as phonons. The flipping can be described by the two lowest, localized states in a double-well potential as shown in Fig. 2.10. These two states form a single TLS and the orientational change of the atomic group is described by quantum-mechanical tunnelling between the two states. The Hamiltonian of the TLS is given [61]:

$$H = \frac{1}{2} \begin{pmatrix} \eta & \Delta_0 \\ \Delta_0 & -\eta \end{pmatrix}. \tag{2.29}$$

Here, η is the asymmetry of the TLS as indicated in Fig. 2.10. The tunnelling matrix element Δ_0 is proportional to the overlap of the wave functions in the two wells and can be written as:

$$\Delta_0 \propto \exp\left(-2d\sqrt{(2mV)}/\hbar\right). \tag{2.30}$$

Here, d is the width of the potential barrier between the two energy minima along the generalized coordinates, m is the tunnelling quantity and V is the height of the energy barrier. The eigenstates of the Hamiltonian in Eq. (2.29) can be expressed as:

$$|-\rangle = \cos(\phi)|L\rangle + \sin(\phi)|R\rangle \tag{2.31}$$
$$|+\rangle = -\sin(\phi)|L\rangle + \cos(\phi)|R\rangle \tag{2.32}$$

where $\tan\phi = \Delta_0/\eta$. The corresponding energy eigenvalues are:

$$E'_\pm = \pm\frac{E'}{2} = \pm\frac{1}{2}\sqrt{\eta^2 + \Delta_0^2} \tag{2.33}$$

The two-level system has been used to describe the variety of line shapes of molecules [56, 61, 62]. The interaction between two-level systems in the matrix and single
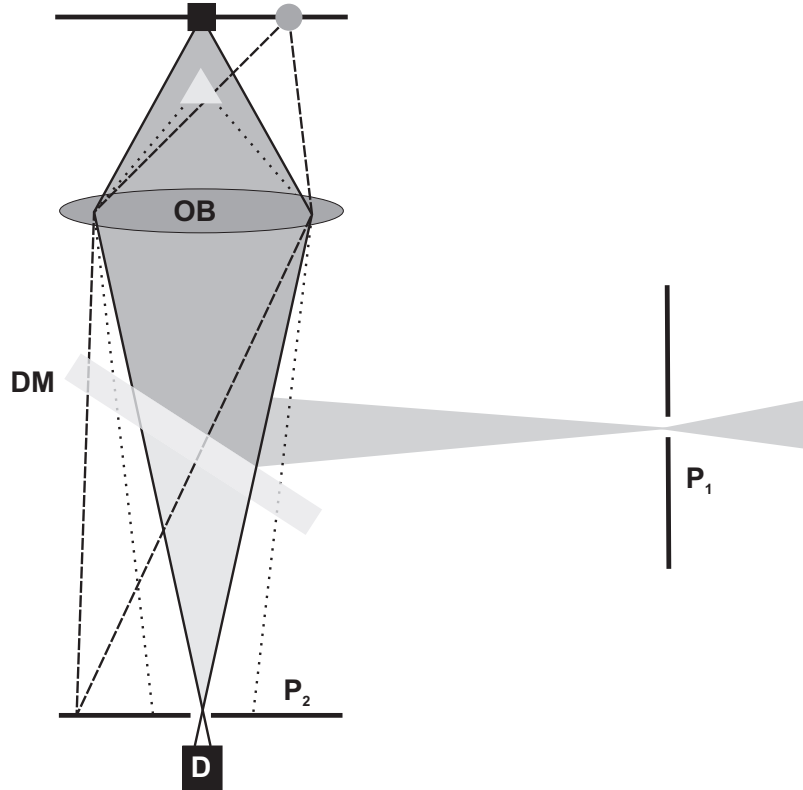
Figure 2.11: Principle of confocal microscopy. P_1 and P_2 are pinholes, OB is the objective, DM is a dichroic mirror and D is the detector. For detailed explanation, see text.

molecules leads, for example, to a splitting of the spectrum of the single molecule, as seen by [58, 60] or frequency jumps [63]. In general, the transition frequency of a single molecule ν can be divided into a static component ν_0 and a dynamic component ν' [61]. If more than one TLS is located in the surrounding of a molecule, the molecular transition frequency can be described:

$$\nu(t) = \nu_0 + \sum_i \nu_i' \zeta_i(t), \tag{2.34}$$

with $\zeta_i(t) = 0$, if the i-th TLS is in its ground state, and $\zeta_i = 1$, if its in the excited state. The static component ν_0 is to the transition frequency of the molecule, if there are no flipping TLS nearby or if the TLS is in its ground state. The dynamic component ν_i' is induced to the molecule, if a nearby TLS flips its state. This component ν_i' determines the line shape of the molecule. Using this model, it can be explained why single molecules, embedded in the same matrix, show a variety of line shapes [10].

2.5 Technical basics

The experimental setup used in this thesis consists of a confocal microscope for single-molecule detection and a scanning-tip unit for Stark-shift imaging. In the following

section, the technical basics are introduced. The principle of confocal microscopy is discussed. The scanning unit as well as all kind of position facilities at low temperature are based on piezoelectric elements. Therefore, an introduction of piezoelectric elements and of their modes of operation, such as slip-stick motion, is given. Finally, the gap-width control by the tuning fork technique is presented.

2.5.1 Confocal microscopy and optical detection

Excitation spectroscopy is performed using confocal microscopy [25, 26, 64]. The principle of a confocal microscope is sketched in Fig. 2.11. Laser light is used to illuminate the sample. The excitation path of the laser light goes from the first pinhole P_1 to the dichroic mirror DM, where it is reflected into the objective OB. The objective focusses the light onto the sample. The sample signal is collected by the same objective and focussed onto the second pinhole P_2. The detector behind the second pinhole detects the signal. The two pinholes are adjusted in such a way, that the laser illuminates the same spot of the sample from which the detector detects the signal. The pinhole in the excitation path and the pinhole in the detection path define a con-focal volume. As sketched in Fig. 2.11, there are three objects in the excitation area of the laser. The square is inside the confocal volume and its signal is focused by the objective on the detector D. The circle is located in the focal plane defined by the excitation pinhole P_1, but its signal does not hit the detector pinhole P_2 due to its position to the optical axis. Therefore, the emission from the circle position is effectively blocked. The triangle is not situated inside the confocal volume. Neither the excitation light is focussed onto its position, nor its emission is focussed at the position of the detector. By scanning the sample, the different objects can be imaged and discriminated. Confocal microscopy is limited by diffraction at the rim of the lenses. Therefore, if two objects are separated by a distance, which is smaller than the diffraction limit, they cannot be resolved. This separation limit, the resolution r, can be expressed as:

$$r = 0.61 \frac{\lambda}{NA},$$

(2.35)

where λ is the excitation wavelength and NA the numerical aperture of the objective. In an optimized experimental setup, the size of the pinholes matches the resolution r. With an excitation wavelength of $\lambda = 580$ nm and $NA = 0.85$ of the objective, the resolution is limited to $r = 416$ nm.

The advantage of using confocal microscopy is the effective blocking of the background signal. The excitation as well as the detection is limited to a spot-size area, defined by the pinholes. No scattered light of a bright spot in the excitation area can overlay the signal of a nearby dimmer spot, as long as the distance between these two spots is larger than the focal spot of the excitation light.
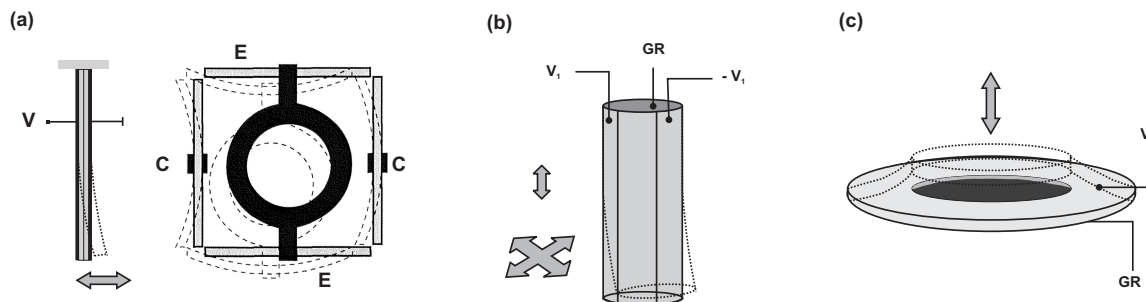
Figure 2.12: Principle of the positioning possibilities. (a) Scanning unit for the sample: the bimorph-scanner. (b) Scanning unit for the tip: the tube piezo. (c) Fine focussing of the sample: disk piezo.

2.5.2   Piezoelectric actuators: positioning elements

At low temperature, a convenient and accurate way of scanning or positioning the different parts of the setup is by piezoelectric actuators. Piezoelectric elements can be moved or bent by applying a voltage. The direction depends on the sign of the voltage and the polarization of the piezo. The advantage of cryogenic temperature condition is, that the typical hysteresis of the piezo-elements disappears.

Scanning facilities

Two different piezoelectric elements are used as scanning facilities. Stripe bimorph piezos form a scanner for the sample, shown in Fig. 2.12 (a) and a tube piezo is used as scanning element for the tip, shown in Fig. 2.12 (b). The sample-scanner consists of 4 bimorph-piezo-elements, which are arranged as sketched in Fig. 2.12 (a). On the left side, a single bimorph-element is shown. By applying a voltage over the piezo-electric layers, the element bends. Depending on the mounting point, the piezo-element bends differently. The four bimorph piezos are arranged in pairs, whereas one pair is fixed in the center (indicated by the 'C'), and one pair is fixed at both edges (indicated by the 'E'). The movement of the scanner is sketched on the right side. The black ring is the sample holder. A more detailed description can be found in [65].

The tip is scanned by a tube piezo, which has four outer segments and an inner electrode, as shown in Fig. 2.12 (b). The inner electrode is set to ground. The four outer electrodes are contacted electrically in opposite pairs. The voltage on the two electrodes of one pair has always the opposite sign. In this way, the tube piezo bends as sketched in Fig. 2.12 (b). With four electrodes on the tube piezo, the piezo can scan or be positioned in the x,y-plane. By changing the voltage on the inner electrode, the tip can also be moved in the μm-range (room temperature) in the z-direction. The operation of the experimental setup is presented in Chapter 3.2.3.
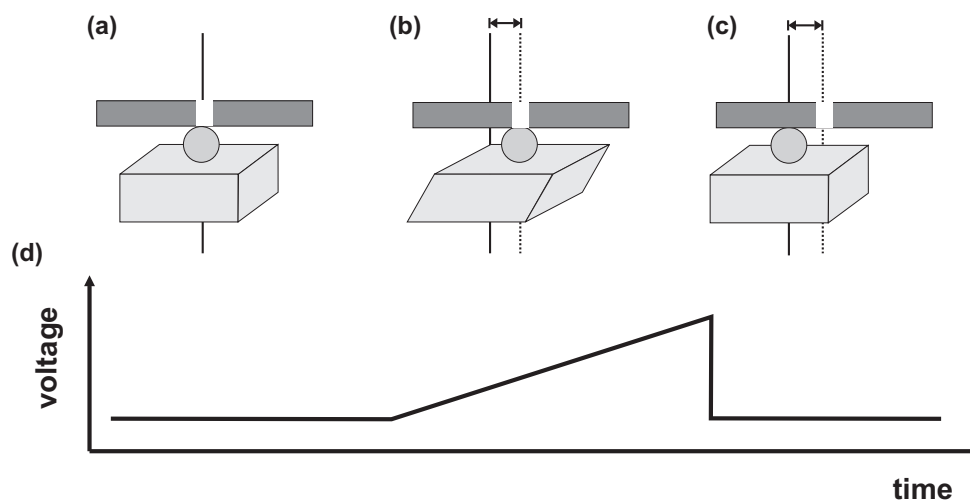
Figure 2.13: Principle of the slip-stick motion. Upper row shows the movement of a plate, which is positioned on the shear-piezos. Lower row shows the driven voltage applied to the shear-piezos.

Positioning facilities

Besides the scanning facilities, piezo-electric elements are used for focussing and positioning. For this application, a disk piezo-element and shear piezos are used. The principle of a disk bender is sketched in Fig. 2.12 (c). The piezo element is a disk with a center hole. By applying a voltage over the upper and the lower electrode, the inner part of the disk bender is moved up or down.

The positioning over distances in the mm-range is done by the slip-stick motion technique. For this technique, shear piezo-elements are used, which shear sideways by applying a voltage. The principle of the slip-stick motion is sketched in Fig. 2.13. Fig. 2.13 (a)-(c) show the movement of the shear-piezos. On top of the piezo a small sapphire ball is glued on which a top plate rests. Fig. 2.13 (d), shows the time dependence of the driving voltage . Starting from left to right, the voltage is increased by a slow voltage ramp. The piezo shears sideways together with the sapphire ball and the top plate. Then, the voltage is switched of suddenly, and the piezo jumps back to the starting position. Due to inertia, the top plate stays at its position. As can be seen by the white mark on the plate, the plate is moved to the right. The slip-stick motion technique operates reliably as long as the contact between the sapphire ball and the top plate is optimized. If the top plate is too light, the contact can be improved by additional little magnets which pull the to plate towards the sapphire balls. Further information is given in Ref. [65]. By placing two shear piezos on top of each other in a perpendicular orientation, a movement in 2 dimensions is achieved.
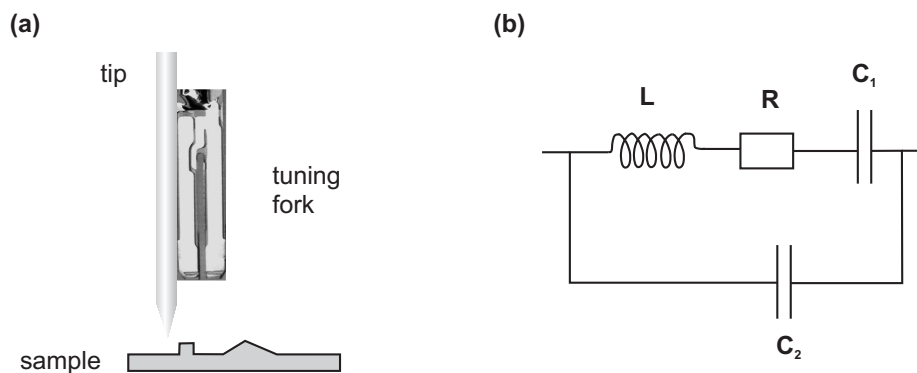
Figure 2.14: (a) Tuning fork sensor in shear-force configuration. (b) Equivalent electric circuit for a piezoelectric sensor.

2.5.3 Tuning fork gap-width control

One possibility of the gap-width control between the tip and the sample is the tuning fork technique. For this purpose, commercially available tuning forks are used. The tuning fork is a piezoelectric element. By oscillating the prongs, a varying current is induced, which can then be detected. The activation of the oscillation of the tuning fork can be done electrically or by a swing quartz. Due to interaction with the surface, the frequency and the amplitude of the oscillation changes. Detecting the change of the amplitude or of the frequency makes the tuning-fork a very sensitive tool for the gap-width control. In Fig. 2.14 (a), a tuning fork in shear-force configuration is shown. In this configuration, the two legs of the fork are oriented perpendicular to the sample surface. A tip is glued to the prongs. The interaction of the tip with the sample surface changes the tuning fork signal, which can then be used for the gap-width control. In Fig. 2.14 (b), the equivalent electric circuit of a piezoelectric sensor is shown. The sensor can be modelled by an oscillating circuit parallel to a capacitor. The operation of the tuning fork in liquid helium is more difficult, but possible [66]. Nevertheless, for most of the time an optical control by eye has been used for positioning the tip during the experiments. Further information on tuning fork sensors for different applications can be found in Ref. [67, 68, 69] for scanning probe microscopy and in Ref. [70, 71, 72] for scanning near-field microscopy.

Chapter 3

Sample system, setup and experimental procedures

The present chapter gives an overview of the properties and the preparation techniques of the sample system. The design of the experimental setup, consisting of a confocal microscope combined with a scanning-tip unit, is briefly described. A detailed description can be found in [66, 73]. The chapter is concluded with a section about the performance of the setup, where the imaging capabilities are presented.

3.1   Sample system

In chapter 2.1.2 the requirements for single molecule spectroscopy have been presented. Apart from other systems, a crystalline sample which meets all the requirements is a matrix of para-terphenyl with dye molecules of terrylene. In the following, both components are shortly specified. Then an introduction of the properties of the sample is given, focussing on the stoichiometry, on the optical properties and on the Stark-shift characteristics.

3.1.1   Properties

The sample of p-terphenyl doped with a small amount of terrylene has been a preferred system for single-molecule spectroscopy and has been under investigation for a long time. Various experimental studies have been carried out at different temperatures, such as investigation of pressure effects [33], persistent hole burning [76], fluorescent lifetime measurements [77], light-induced spectral jumps [13, 78] and Stark-shift measurements [21, 74, 75, 79]. The properties of this crystal system are presented in detail in Ref. [80, 81, 82].

Matrix: para-terphenyl ($C_{18}H_{14}$)

The structure of a para-terphenyl molecule is shown in Fig. 3.1 (a). The molecule consists of three benzene rings which are connected by C-C bonds. p-terphenyl forms
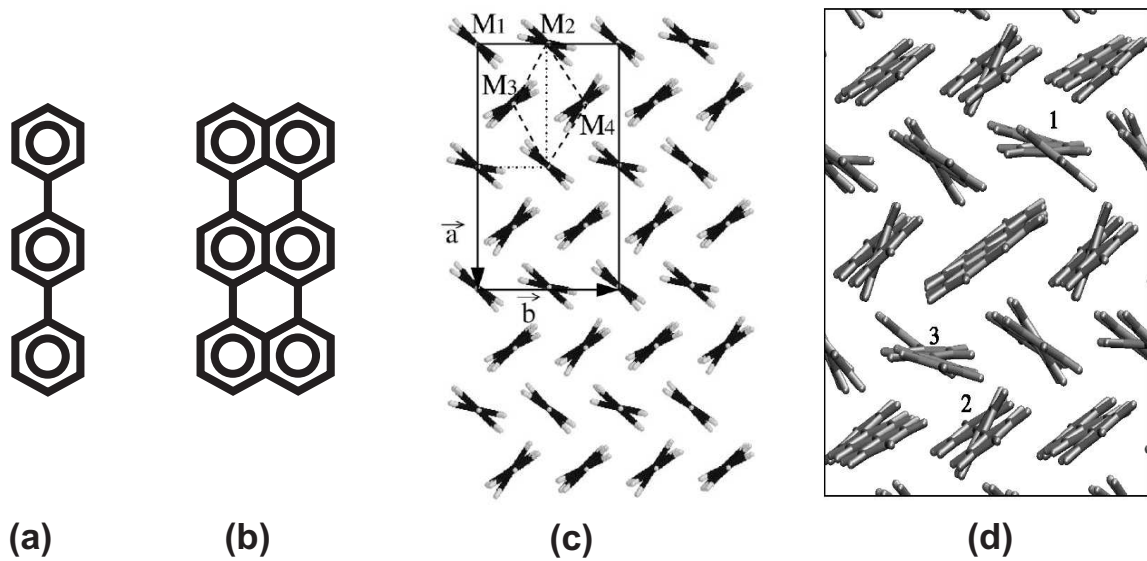
Figure 3.1: Sample system. (a) Structure of a para-terphenyl molecule: the matrix. (b) Structure of a terrylene molecule: the fluorescent dopant. (c) Para-terphenyl crystal with the c-axis perpendicular to the paper plane. The dashed line shows the low temperature unit cell, the dotted line the room temperature unit cell. The points M_1 to M_4 mark the four inequivalent positions at which the terrylene molecule can replace a *p*-terphenyl (figure taken from [74]). (d) Mono-substitution of terrylene in *p*-terphenyl at the M_3 position (figure taken from [75]).

a crystal, in which all molecules are aligned with their longest axis parallel to the c-axis of the crystal, shown in Fig. 3.1 (c). The figure shows a perspective along the c-axis and only the orientation of the benzene-rings can be seen. At room temperature the benzene rings form a non-planar structure because of repulsive forces between the rings. The center ring can have two tilted orientations with an angle of $\pm 13°$ to the plane which is formed by the two outer phenyl-rings. This flipping of the orientation can be described by a double well potential which is called the tunnelling two-level system of the matrix. At room temperature, the distribution of these two conformations of the center phenyl ring is random (dynamic equilibrium). A p-terphenyl crystal has a monoclinic unit cell with two molecules per cell at room temperature. At lower temperatures ($T < 193.3$K), the center rings become fixed in one position ($= 13°$ or $-13°$), alternating in orientation from neighbor to neighbor. Hence, the symmetry elements of this crystal structure are reduced. The unit cell undergoes a transition to a triclinic unit cell with four molecules per cell. For convenience, a pseudo-monoclinic unit cell can be chosen with 8 molecules per cell. A more detailed description of the crystal structure, investigated in coherent and incoherent neutron scattering experiments, can be found in reference [83]. For a theoretical work on the disordered-ordered transition, see [84]. In Fig. 3.1 (c) all three unit cells are shown. The c-axis of the crystal points into the paper plane. The p-terphenyl molecules are aligned with their longest axis along the c-axis. The dashed line indicates the low temperature triclinic unit cell, the solid line the pseudo-monoclinic cell and the dotted line the high-temperature monoclinic unit cell. The crystal grows mainly in the a-b plane, which leads to thin crystal flakes.

The optical characteristics, such as the fluorescence excitation spectrum and the quantum efficiencies of thick p-terphenyl crystals at room temperature are discussed in [85]. An important aspect for the present work is that p-terphenyl is fluorescent in the short-wave ultra-violet region. However, since the spectral range of interest for the experiments is the visible range, above wavelengths of 560nm, the optical activity of p-terphenyl does not interfere with the measurements.

Dye: terrylene ($C_{30}H_{16}$)

The terrylene molecule consists of 6 benzene rings as shown in Fig. 3.1 (b) and is twice as large as a p-terphenyl molecule in one dimension. The molecule is much more rigid than a p-terphenyl molecule. Orientational flips of the center rings are not possible in contrast to p-terphenyl molecules. The properties of a fluorescent dopant are strongly influenced by the matrix. Therefore all properties of terrylene will be presented in relation to the p-terphenyl matrix.

Crystals: Stoichiometry, optical properties and Stark-shift characteristics

Doping a p-terphenyl crystal with terrylene molecules, a logical consequence of the relative size difference would be, that one terrylene molecule replaces two p-terphenyl

unit cell	optical site	frequency [nm]	wavenumber [cm^{-1}]	photostable
M_1	X_4	577.9	17304	yes
M_2	X_3	578.3	17293	no
M_3	X_1	580.4	17230	no
M_4	X_2	578.5	17286	yes

Table 3.1: Assignments of the four main optical sites in the terrylene/p-terphenyl crystal system, see references [75, 80, 81]. The first column shows the four inequivalent sites of the crystal; second column assigns the crystal sites to the optical sites; third and fourth column are the excitation frequency and the wavenumber $k = \frac{1}{\lambda}$, respectively; last row defines, which optical sites is photostable.

molecules in the unit cell. However, quantum-chemical calculations and their comparison to experiments have revealed that only one p-terphenyl molecule is replaced by one terrylene molecule [74, 75]. The longest axis of the terrylene molecule is aligned parallel to the longest axis of the p-terphenyl molecules. There are four inequivalent positions inside the unit cell of the p-terphenyl crystal, where one p-terphenyl molecule can be replaced by one terrylene molecule. These four sites are named M_1 to M_4, as labelled Fig. 3.1 (c). The four sites M_1 to M_4 provide different surroundings for the terrylene, given by the different orientation and tilt of the middle phenyl ring of the p-terphenyl molecule. As mentioned in the chapter 1, the optical resonance of single molecules reacts very sensitively to changes in the local environment. Consequently, terrylene molecules positioned at different crystal sites exhibit different optical excitation frequencies. These four possible excitation frequencies define the four optical sites X_1 to X_4 of terrylene molecules embedded in a crystalline matrix of p-terphenyl. The direct assignment of the crystal site M_1 to M_4 to the optical site X_1 to X_4 has been very difficult [74, 75, 80, 81]. Nevertheless, the result, presented in table 3.1, has been obtained experimentally and theoretically.

A photostable state of the chromophore is required for excitation spectroscopy. It is known from experimental measurements that only dye molecules positioned at X_4 and X_2 sites are photostable [74, 75]. Molecules at the X_1-site show some reversible spectral jumps which can be controlled by an electric field. This effect has been used for an optical switch [13, 21]. Dye molecules at the X_3-site are very unstable, since they jump to, so far, unknown spectral positions on a very short time scale. Reviews of a detailed characterization of the p-terphenyl/terrylene-system can be found in [80, 81, 82]. Table 3.2 summarizes the optical properties at cryogenic temperature, such as the line width Γ, the quantum efficiency ϕ_f and the saturation intensity I_{sat}.

The orientation of the transition dipole moment lies along the long axis of the terrylene molecule [86]. Consequently, the transition dipole moment of terrylene is aligned along the c-axis of the crystal. The orientation of the transition dipole mo-

saturation intensity I_{sat} [W/cm^2]	quantum efficiency ϕ_f	line width Γ_0 [MHz]	lifetime T_1 [ns]
22.7	~ 1	48.1 ± 4.9	4.2 ± 0.1

Table 3.2: Optical parameter of terrylene in a p-terphenyl matrix. Values are taken from references [77, 80].

ment and the electric field of the excitation light determines the interaction between the molecule and the laser, as described in Eq. 2.26. Since the electric field of the excitation light is also parallel to the c-axis, it is more difficult to excite the terrylene molecule. Therefore, only molecules with at least a small angle to the c-axis can be excited. The orientation of the dipole moment along the c-axis also implies a high saturation intensity.

Crystals of p-terphenyl are anisotropic. As mentioned in chapter 2.2.2, the dielectric constant of such an anisotropic matrix is a tensor and depends strongly on the crystal orientation. However, simplifying the calculation of the local field E_{loc} from Eq. (2.18), the mean value for the Lorentz-constant f_L can be used:

$$\vec{E}_{loc} = \bar{f}_L \vec{E}_{ext}, \tag{3.1}$$

The mean value of the Lorentz-constant f_L can be approximated by [87]:

$$\bar{f}_L = 1.254. \tag{3.2}$$

The local field at the position of the dye molecule determines its Stark shift. As discussed in chapter 2.2, the permanent dipole moment difference $\Delta \vec{\mu}$ and the change in polarizability $\Delta \tilde{\alpha}$ of the molecule define the Stark effect. The free terrylene molecule is centrosymmetric. This symmetry excludes a permanent dipole moment of the terrylene molecule. A free centrosymmetric molecule shows therefore only a quadratic (or higher order) Stark effect. Consequently, a terrylene molecule would show a pure quadratic Stark shift, if the molecule is built into the p-terphenyl matrix without being distorted or twisted in any kind. But, as already mentioned, the terrylene molecule is twice as large as a p-terphenyl molecule. It is therefore not very likely, that the terrylene is built into the matrix without any additional stress. This strain field can introduce a shift or broadening of the resonance frequency peak [33], as well as a permanent dipole moment [74]. On account of the induced dipole moment, terrylene molecules show both, a linear and a quadratic part of the Stark shift. The appearance of the Stark shift is used by some groups as a measure of quality for their sample. If the Stark shift is close to pure quadratic, the terrylene is suppose to be built into the crystal undistorted. The sample is therefore classified a 'good' sample.

dopant	matrix	lin. Star shift [MHz/(kV/cm)]	quad. Stark shift [MHz/(kV/cm)^2]	$\Delta\mu_{ind}$ [D]	$\Delta\alpha$ [Å^3]
terrylene	polyethylene	-	-	1	-
terrylene	naphtalene	2.8	0.1	0.01	50
pentacene	p-terphenyl	0.002-0.056	-0.022	0.002-0.57	10 - 22

Table 3.3: Stark-shift parameter of terrylene in a matrix of polyethylene [17] and a matrix of naphtalene [90] and pentacene in a p-terphenyl-matrix [16].

Finally, the orientation of the dipole moment difference $\Delta\vec{\mu}$ and the polarizability $\Delta\tilde{\alpha}$ is of interest. Since $\Delta\vec{\mu}$ is induced by the matrix, the orientation cannot be easily assigned. Consequently, it depends on the way the terrylene molecule is squeezed in its position. The polarizability is a tensor. For some molecules, as for pentacene, the polarizability has been estimated and also measured for free molecules in a supersonic-jet experiment [88]. Unfortunately, these kind of measurements have just been started with terrylene [89]. The values for terrylene from crystal measurements vary and are ergo only usable as guidelines. Values for the p-terphenyl/pentacene system can be also used as an estimation. Values for $\Delta\vec{\mu}$ and $\Delta\tilde{\alpha}$, as far as known, are summarized in Table 3.3.

The Stark shift of terrylene in p-terphenyl shows some interesting features. It has been seen in experiments, that molecules at the X_1 site show a kind of anomalous Stark shift. The Stark shift switches between an quadratic Stark shift and an linear Stark shift. This anomalous shift seems to depend on sudden flips of the center rings of neighboring p-terphenyl molecules. This new configuration (called XY-site) induces a different dipole moment to the terrylene molecule. It shows now a strong, mainly linear, Stark-shift behavior [21, 74, 79]. Results from these measurements are shown in Fig. 3.2 (a). Since the state of the molecule, being in X_1 or being in XY, can be externally controlled by an electric field, the idea came up, to use this method to control single quantum systems. The experimental investigation of the anomalous Stark shift also shows, that the orientation determination of the dipole moment and the polarizability is very difficult. The orientation always depends on the surroundings. In another experiment, a large, charged gold particle has been used to induce a Stark-shift to a single molecule. The Stark shift of the molecule has been deduced from spectra taken at varying tip position. With this method of analysis, Stark-shift maps of the molecule depending on the position of the gold particle have been measured, as shown in Fig. 3.2 (b). The Stark-shift maps have been used to localize single molecules.
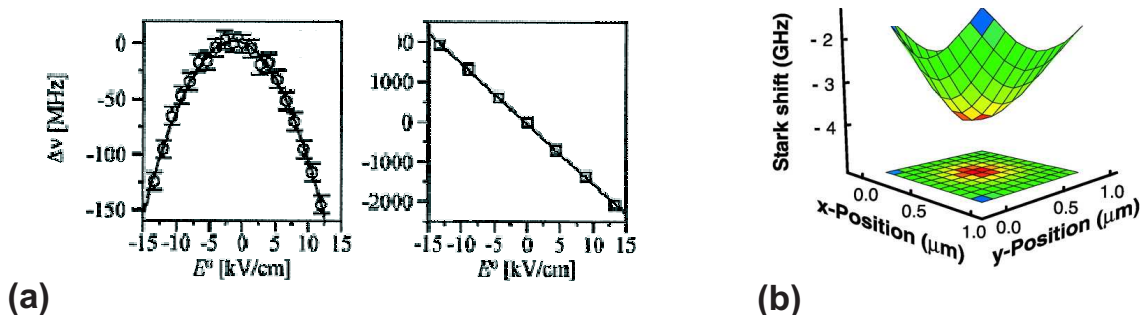
Figure 3.2: Recent work on the Stark-shift of terrylene in p-terphenyl. (a) Anomalous Stark-shift of the X_1 site, see [78]. (b) Stark-shift map of one single terrylene molecule, see [15].

3.1.2   Preparation

The preparation of single-crystalline, homogeneous samples of the p-terphenyl/terrylene-system is not an easy task. As discussed above, both molecules are quite different in size. Therefore, the physical characteristics, such as the melting point and sublimation temperature strongly differ from each other. This fact makes it most demanding to produce homogeneous samples with a reproducible ratio of matrix and dopant molecules. Two different kind of sample preparation techniques have been used in this work. The first data sets have been taken with single-crystal flakes, which have been produced by the cold-finger-sublimation technique. The crystal flakes have a thickness up to 20 μm. Since the Stark shift depends very strongly on the tip-molecule distance, a sample thickness of 20 μm is too thick for Stark-shift measurements. Another problem of the sublimation crystals has been the accumulation of dye molecules at the grain boundaries, which makes it difficult to detect single molecules, even at low temperature. For these reasons we have investigated an alternative preparation technique, the spin-coating technique, which produces a film of micro-crystals. The thickness of these crystals lies between 50 to 150 nm, which is compatible with the Stark-shift measurements. The disadvantage of these micro-crystals are the higher strain and stress fields, which naturally exist inside these fast-growing crystals. These fields might cause a stronger spectral diffusion and a broadening of the zero-phonon lines, which has not been observed in the experiments.

Glass plates

Thin glass slides are used as sample holder for both kind of samples. The thickness of the slides is $0.09 - 0.12$ mm. In order to avoid an background signal from impurities, the plates were cleaned according the following protocol. First, the surface has been cleaned with lint-free tissues and ethanol. Afterwards, the plates have been baked in an oven (5 hours at 500°C).

The first data sets of Stark-shift measurements have been taken without a defined counter electrode. Later on, the glass plates have been used as a defined counter electrode. For this purpose, a very thin layer of Titanium ($\sim$ 3 nm) has been evaporated on one side of the glass plate after the baking process. This thin layer is still transparent for the laser light and the losses of the fluorescent signal are small. The electric resistance of this thin Ti layer has been a few kΩ. The sample has been prepared on the metal-free side.

Cold-finger sublimation technique

For the cold-finger sublimation method, a glass flask with a water-cooled glass finger has been used [65, 91]. The apparatus is sketched in Fig. 3.3. At the beginning, the glass flask is filled with a small amount of a powdered mixture of the matrix and the fluorescent molecule. Normally, 1g of p-terphenyl is mixed with a few tiny grains (3 to 5) of terrylene. The flask is evacuated ($p \sim$ 2-4 mbar) by a rough pump and in a next step, it is flushed with nitrogen gas. Afterwards the flask (with closed valve to the nitrogen gas bottle, cooling cycle of cold finger does not run) is emerged into an hot oil bath ($T = 220°$C) in a glass pot. The temperature of the bath is controlled by a heating spiral inside the oil, a heating plate from below the glass pot and a magnetic stirrer, which assures a homogeneous temperature distribution inside the oil bath. In a first step, the powder mixture of p-terphenyl/terrylene is melted. The flask is removed from the oil bath. The crystallized mixture of p-terphenyl/terrylene is then pulverized in a ceramic mortar into a very fine powder. The melting process and the following pulverization result in more homogeneous powder of p-terphenyl/terrylene (slightly pink powder). In a second step, the powder is filled back into the glass flask, which is again evacuated and flushed with nitrogen gas (pressure is kept at 50 mbar, closed valve system). The cooling cycle of the cold finger is switched on (water/ethylene glycol mixture) and the temperature is set to $T = 110°$C. When the temperature is stable, the flask is again emerged into the oil bath ($T = 180°$C, below melting temperature). The sublimation process starts and it takes a few hours to obtain crystals of a reasonable size. A typical thickness of these crystal is around 20 μm and the size is a few mm large. The crystal flakes grow along the a/b-plane and are therefore attached to the cold finger with their thinnest side. They stay perpendicular to the surface. This has the advantage of an easy harvest after the sublimation is finished. The flakes are harvested carefully from the cold finger, and deposited on cleaned glass plates, where they stick by van der Waals forces.

Some properties of the sublimated crystals are summarize in Fig. 3.4. In Fig. 3.4 (a) a picture, taken by a light microscope in dark-field mode, is shown. The crystal sticks to the glass slide. One can see that the crystal does not lie perfectly flat on the surface, because some interference fringes appear. The crystal never sticks to the glass surface without inducing stress to the crystal. This might influence the spectral stability of the single molecules. Additionally, the flake has more than one crystal layer,
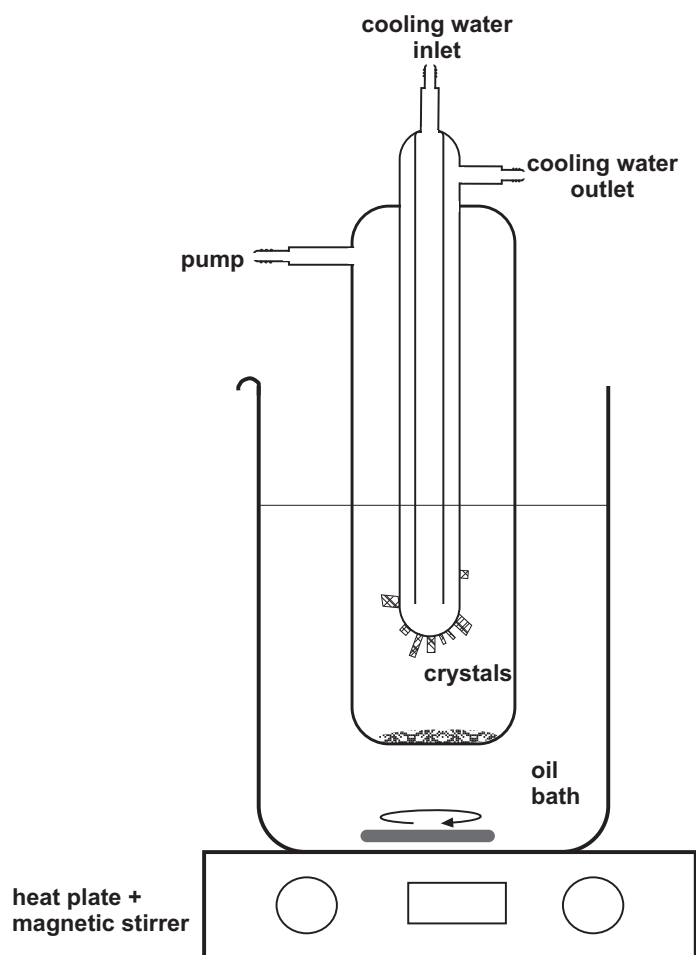
Figure 3.3: Cold finger sublimation apparatus (simplified): A glass pot with regular oil (heatable up to 200 °C) is placed on top of a heat plate with a magnetic stirrer. The cold finger has a left outlet to the rough pump for evacuation and an outlet to the pressure gauge (the connection to the pressure gauge is on the back side and not shown here). On top is the inlet for the cooling liquid. On the right side is the outlet for the cooling liquid to close the cycle to the liquid pump. The mixed-molecule powder is placed at the bottom of the glass flask. On the cold finger, the sublimation of the crystals starts and the crystals grow along the a/b-plane perpendicular to the finger surface.
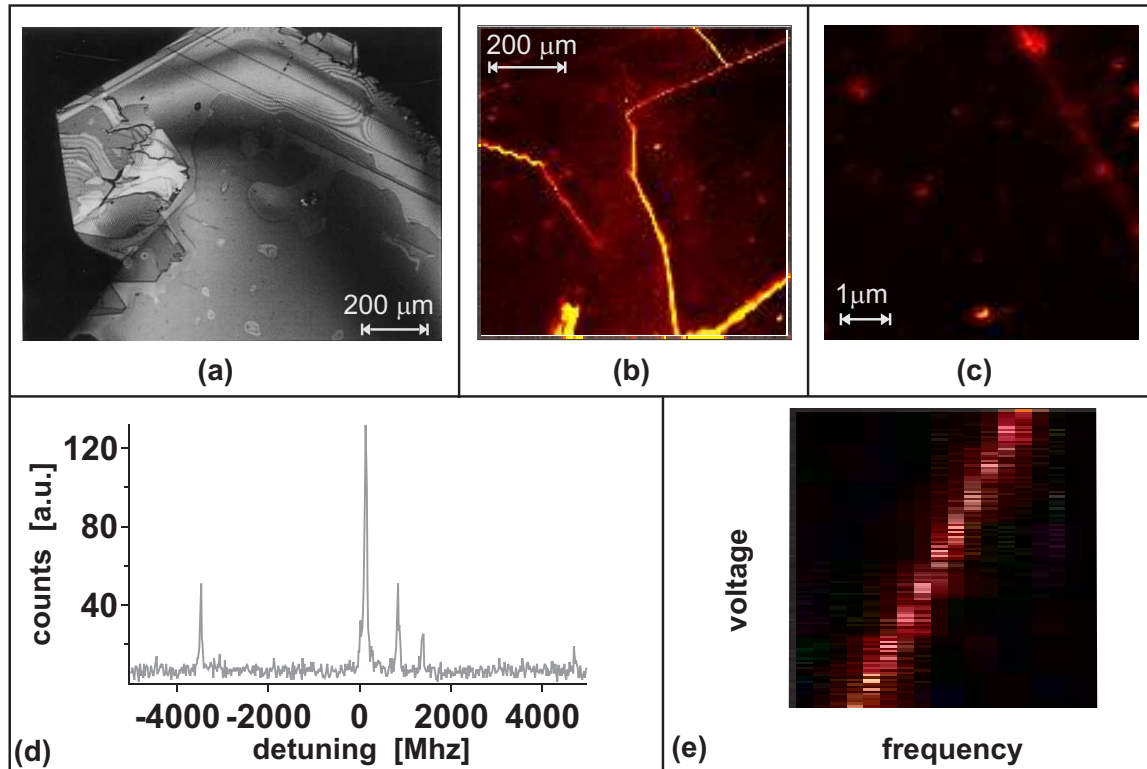
Figure 3.4: Summary of typically observed characteristics of the sublimation crystals. (a) Light microscope picture (dark-field mode) of a crystal flake lying on a glass plate. Interference fringes show that the crystal does not lie flat on the surface. (b) Confocal image of a crystal flake at room temperature. Most of the fluorescent molecules accumulate along the grain boundaries of the crystal flake. (c) Confocal image at $T = 1.8$ K. Several fluorescent spots are detected at rather high laser power $P \sim 1\mu$W. (d) Excitation spectrum at $T = 1.8$ K, with several molecules with linewidths between $\Gamma \sim 50 - 60$ MHz. (e) Stark-shift characteristic of a single molecule at $T = 1.8$ K. The applied voltage is plotted over the excitation frequency of the laser: dominant linear Stark shift is detected.

as seen on the left side by the step-like structure. In Fig. 3.4 (b), a typical confocal image at room temperature is shown. Even though fluorescence is detected over the whole scan range, it is obvious that most of the dye molecules are accumulated at the grain boundaries. The boundaries appear as bright lines in the image. In Fig. 3.4 (c) a confocal image at cryogenic temperature ($T = 1.8$ K) is shown. Several bright spots are detected, spread out over the whole scan range. The smaller spots belong typically to single molecules (spectrum not shown here). In the upper right corner, even the grain boundary becomes visible as a dim line, since the image is taken at rather high laser power $P \sim 1\mu$W. A spectrum, containing several molecules, is presented in Fig. 3.4 (d). The spectrum is taken at the position of a larger fluorescent spot in the confocal image. The scan range of the laser frequency is 10 GHz. The line width of these molecules are between $\Gamma \sim 50 - 60$ MHz by a laser power of $P \sim 30$ nW. This correspond quite well to the predicted value of 48 MHz [80]. Fig. 3.4 (e) shows

the Stark shift of a single molecule in a the sublimation crystal at $T = 1.8$ K. In this image excitation frequency of the laser is plotted over the applied voltage. The resonance of the molecule shifts towards higher frequencies. A dominant linear Stark shift is observed which has been quite typical for the sublimation crystals.

Spin-coating technique

The second method for growing fluorescent crystals is the spin coating technique. The method is described in [92]. We adapted it to our needs. The matrix molecules and the fluorescent molecules are dissolved separately in toluene. Both solutions are slightly over-saturated, with a slight precipitate at the bottom of the solution. The saturated solution of p-terphenyl has to be replaced by a fresh one every second week. The p-terphenyl seems to precipitate and to form some kind of unsolvable crystals or cluster. With such an old solution, the result of the spin coating technique has been a distribution of very few, large and non-fluorescing crystal on the glass plate. No such problem has been experienced with the terrylene solution. Different mixing ratios of the two saturated solutions have been tested. A mixing ratio of 1/3 of the saturated p-terphenyl solution and 2/3 of the terrylene solution results in highly fluorescent micro-crystals. A mixing ration of 50/50 of both saturated starting solutions results in less concentrated micro-crystals. For mixing, the solutions are kept in the ultrasonic bath for 30 minutes (temperature of the bath has been around 40 °C). A cleaned glass plate (metallized side down) was fixed on the spinning disk with two thin stripes of scotch tape. A droplet of 20 to 25 μl of the mixed solution is then placed in the middle of the spinning glass with a suitable micro-pipet as shown in Fig. 3.5. The droplet is immediately stretched out as a thin film over the whole glass plate. After 30s, the toluene is evaporated and the spin-coater can be stopped. With this technique, a thin film of micro-crystals is produced. The typical thickness of these micro-crystals lies between 50 and 150 nm and the size is a few μm large.

The typically observed properties of the micro-crystals are summarized in Fig. 3.6. In Fig. 3.6 (a) a light microscope image in dark-field mode is shown. The micro-crystals are spread out homogeneously over the whole glass surface. They appear in various sizes, ranging from 0.4 to 1.7 μm. Fig. 3.6 (b) shows an AFM image of the sample. Some micro-crystals show a step-like topography near their edges. The surface of the crystals looks very smooth, which is an indication of nicely grown crystals. Fig. 3.6 (c) shows a typical confocal image at room temperature. The micro-crystals appear as bright spots of varies sizes between 4 and 30 μm. No single molecules can be distinguished in the fluorescent signal, since the concentration of the dye molecule is high. In Fig. 3.6 (d) a confocal image at $T = 1.8$ K is shown, recorded with a laser power of $P \sim 0.8\mu$W. Several single molecules are located in the image. The number of observed molecules within the maximum scan range is typically higher as compared to the sublimation crystals. The stripy pattern of the fluorescent spots, visible on the left side of the image, comes from vibration of the sample scanner, which
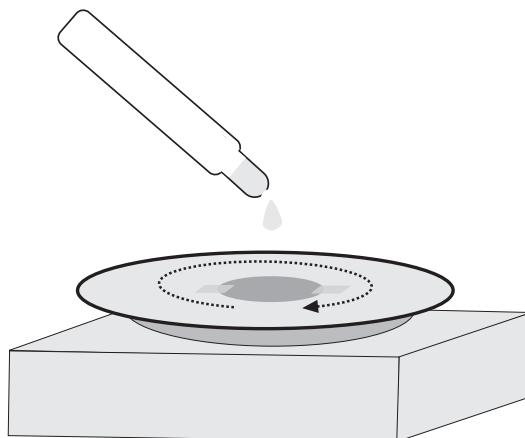
Figure 3.5: Sketch of the setup for the spin-coating technique. On top of the disk, the glass plate is fixed with two little stripes of tape. A little droplet of 20-25 μl of the mixed molecule solution is placed in the middle of the spinning plate with a suitable micro-pipet. The droplet is stretched out over the glass plate and small micro-crystals are formed after the evaporation of the solvent.

were later eliminated. In Fig. 3.6 (e) an excitation spectrum with a frequency range of 20 GHz is shown. Several molecules are detected. The line width of the resonances vary between 20 and 80 MHz. The line width of molecules in the micro-crystals are typically smaller as the one observed in the sublimation crystals. Single molecules in the micro-crystals typically show a dominant quadratic Stark shift as shown in Fig. 3.6 (f). The molecule exhibit a Stark shift of $\Delta\nu = -140$ MHz by applying a voltage of $V = 150$ V to the tip. A combination of the linear and quadratic Stark-shift is also observed quite often.
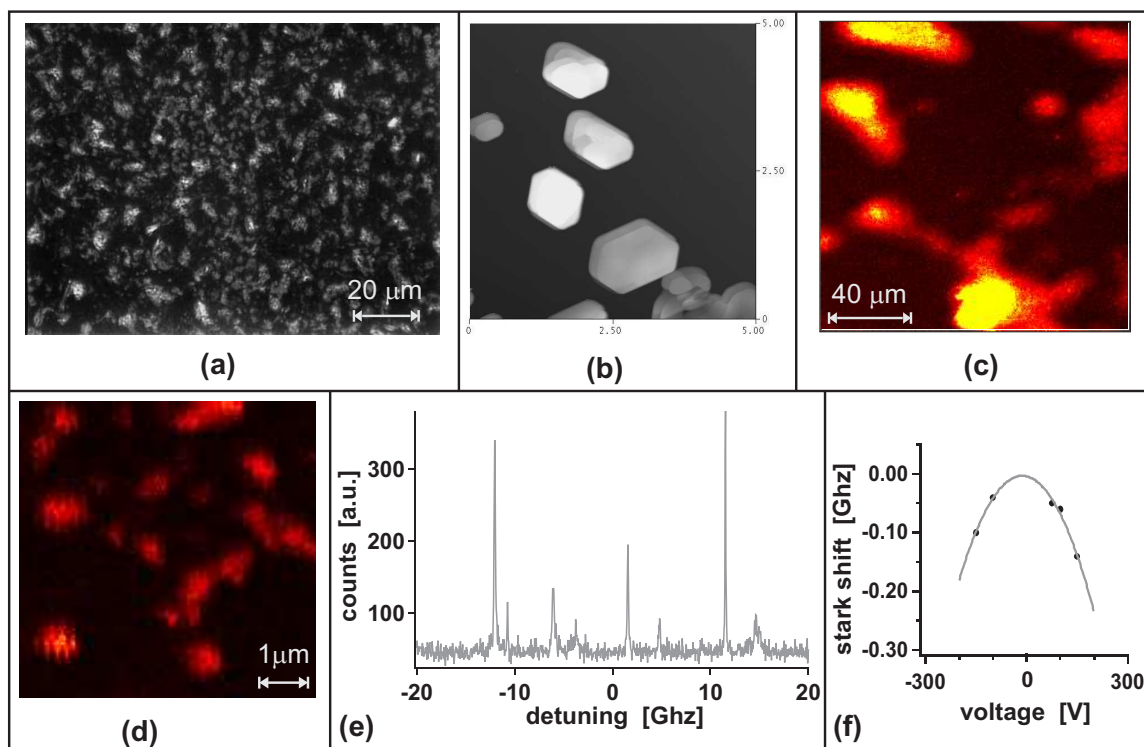
Figure 3.6: Summary of typically observed characteristics of micro-crystals prepared by the spin-coating technique. (a) Light microscope picture in dark-field mode. The micro-crystals are distributed over the whole surface of the coverslip. (b) AFM picture of single micro-crystals. Scan range is $5 \times 5 \mu$m. Color scale is not calibrated. Besides some small steps, the surfaces of the crystals are very smooth, an indication for a nicely grown crystal. (c) Confocal image at room temperature. The fluorescent molecules seem to be well distributed over the micro-crystals. (d) Confocal image at $T = 1.8$ K. Several fluorescent spots are detected. (e) Excitation spectrum at $T = 1.8$ K with several molecules in one laser scan with line width between $\Gamma \sim 20 - 80$ MHz. (f) The Stark-shift shows a dominate quadratic dependence.

3.2 Stark-shift microscope for low temperature

The setup used in this work can be divided in two parts, which have been described in detail elsewhere [66, 73]. One part is a confocal microscope and the second part is a scanning tip setup for Stark-shift microscopy. The setup for single-molecule detection is a sample-scanning confocal optical microscope (SCOM) adapted for cryogenic operation in a liquid helium bath cryostat. On top of the confocal microscope, an additional scan head is mounted. The scan head hosts a scanning-tip setup for the Stark-shift microscopy. The following section is divided in several parts summarizing the technical details and functions of the elements of the setup. The first part describes the confocal microscope with focus on the optical path and the light source. The next section concentrates on the scanning-tip design, the tip preparation and the electrical contact to the tip. Since there is a large variety of positioning elements with an electrical control system, the third sections gives an overview of the positioning control.

3.2.1 Optical detection system: the confocal microscope

The principle of a confocal microscope has been already discussed in section 2.5.1. The confocal volume is defined by two pinholes. The pinhole in the excitation path is defined by the diameter at the fiber exit and the pinhole of the detection path is defined by the active area of an avalanche photo diode. The microscope itself is designed as a sample-scanning microscope. In this way, the alignment of the laser beam is less critical as compared to a laser-beam-scanning setup. The scanning of the sample is done by special arrangement of bimorph-piezo elements, as shown in section 2.5.2. The microscope objective is installed inside the liquid helium cryostat. By placing the objective as close as possible to the sample, a high numerical aperture is achieved.

Optics

The optical path of the system is sketched in Fig. 3.7. The laser system, consisting of an Ar^+-ion laser and a continuous-wave ring dye laser, provides the excitation light which is monitored by a wavemeter (Burgleih) and a spectrum analyzer (TROPEL 240). This part of the setup is located in room 1. The light is coupled into a single-mode glass fiber (FIB 1) and guided to a power stabilizer (CRI, LS-Pro-VIS) in room 2. After passing the power stabilizer, the laser beam goes through a telescope setup formed by lenses L1 and L2, to increase the diameter of the beam from about 1.5 mm to 10 mm. The increase of the beam diameter guarantees a complete filling of the microscope objective entrance aperture, which guarantees a diffraction limited spot on the sample. Passing through a filter wheel (FW), the laser beam is reflected from a wedge (W) and coupled into the objective (microthek, Na=0.85, ×60) inside the cryostat via a 45° mirror. The same objective collects the emitted red-shifted fluorescent signal and the reflected laser light (red path). The fluorescent signal passes the
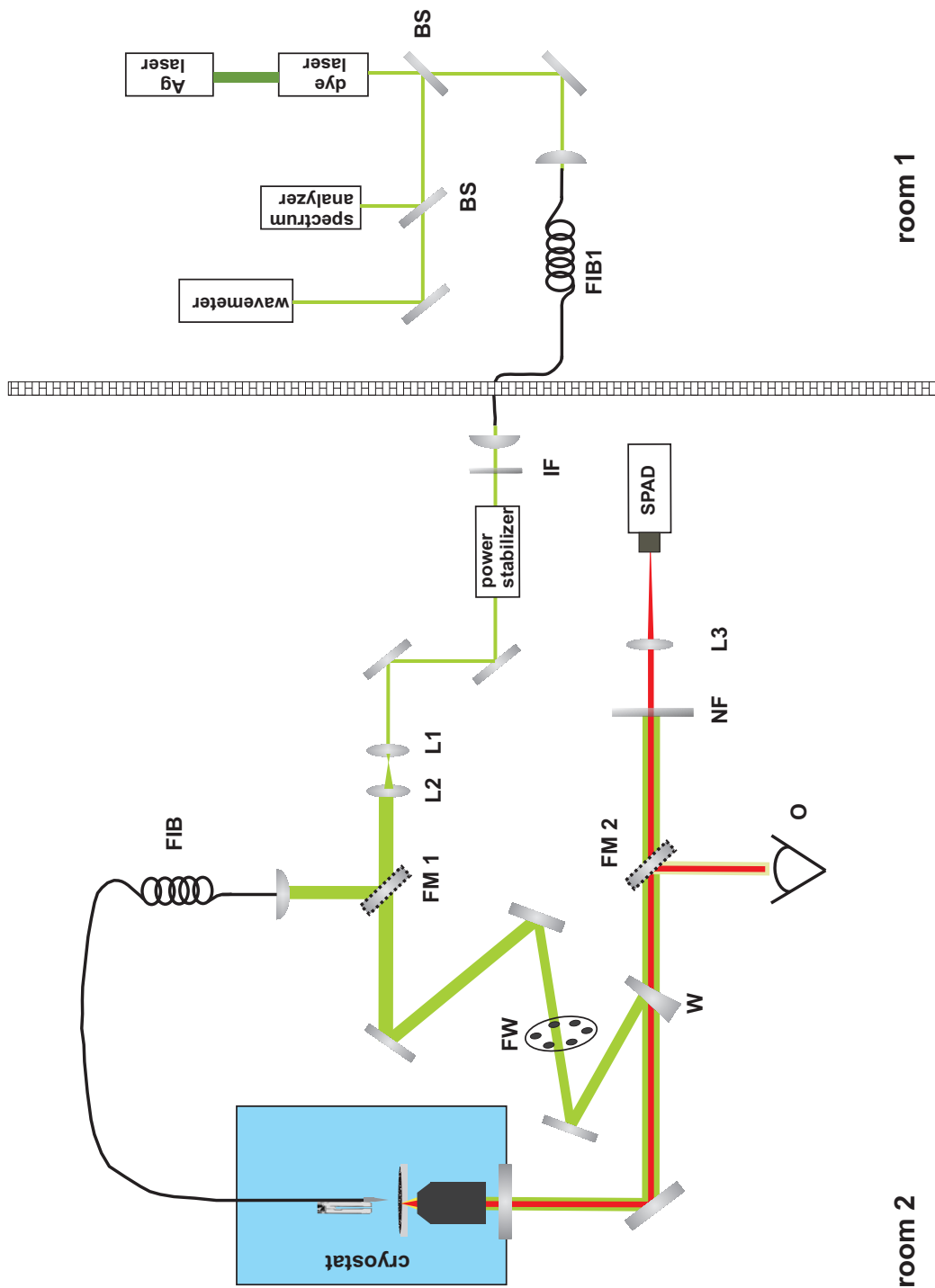
Figure 3.7: Optical detection system. Room 1: An Argon-Ion-laser pumping a dye laser; beam splitter (BS) guiding a small portion of light to the wavemeter and the spectrum analyzer; Fiber (FIB1) guiding the light to the next room. Room 2: power stabilizer, telescopic setup (L1 and L2); flippable mirror (FM1) to direct the light either to the tip (FIB2) or to the confocal microscope; filter wheel (FW), wedge (W) to the cryostat and to the detection device; flippable mirror (FM2) directs the light either to the ocular or to the single-photon counting avalanche photo diode (SPAD) through a notch filter (NF) and a focussing lens (L3)

notch filter (NF), where the reflected excitation light and the resonance fluorescence are blocked. The red-shifted fluorescence of the sample is focussed by lens L3 on a single-photon counting avalanche photo diode (SPAD). The SPAD (PerkinElmer, SPCM-CD2801) is connected to a counter, which is read out by a computer. The fluorescence signal of the sample can also be directed to a video camera or to an ocular for observation by eye using a flippable mirror (FM 2). Another flippable mirror (FM 1) behind the telescope setup opens the possibility to couple the laser light through an optical fiber (FIB 2) into the metallized tip. The metal layer of the glass fiber tip is transparent for the laser light. The light transmitted via the objective can be observed by the video camera. This signal has been used to locate and position the tip over the objective. A detailed description of the operation of the scanning-tip setup is presented in section 3.2.2. A description of the operation of the sample-scanning confocal microscope is given in section 3.2.3, including a top-view of the microscope in Fig. 3.12.

Light source

In chapter 2.1.2, the characteristics of single molecules at low temperature have been introduced. If single molecules are to be addressed one after the other, a laser is required which has an even narrower line width than the single molecules and it must be tunable in frequency. A laser system, meeting these two requirements, is a tunable single-mode continuous-wave dye laser (Coherent, 699-21) pumped by a continuous-wave Argon Ion laser (Spectra Physics, Model 2045; Coherent, INNOVA300). The Argon Ion laser is used at a wavelength of $\lambda \sim 514$ nm and is driven with an output power of $P = 4 - 5$ W. The single mode dye laser can be tuned over a wavelength range of ~ 570 nm to ~ 610 nm (using Rhodamine6G as fluorescent dye). The output power of the dye laser depends on the wavelength and lies between $P = 300 - 500$ mW, which is more than enough for excitation spectroscopy. The optical bandwidth of the dye laser is 1-2 MHz and the frequency can be scanned over a range of 30 GHz. The drift stability of this laser system has been characterized (see [65]).

3.2.2   Scanning tip setup

The second part of the Stark-shift microscope is the scanning-tip unit. Detailed design description can be found in [65, 66]. The performance of the setup is discussed in section 3.3.

Design of the scanning-tip unit

The tip setup is arranged on top of the of the confocal microscope as shown in Fig. 3.8. The whole unit can be moved independently of the confocal microscope above the sample (SP) and the objective (OB). On the left and right side of the tip unit, mounted on the bulk unit of the confocal microscope, there are two 16-pin electrical connectors (EC 1 and EC 2). The cables for the electric elements of the
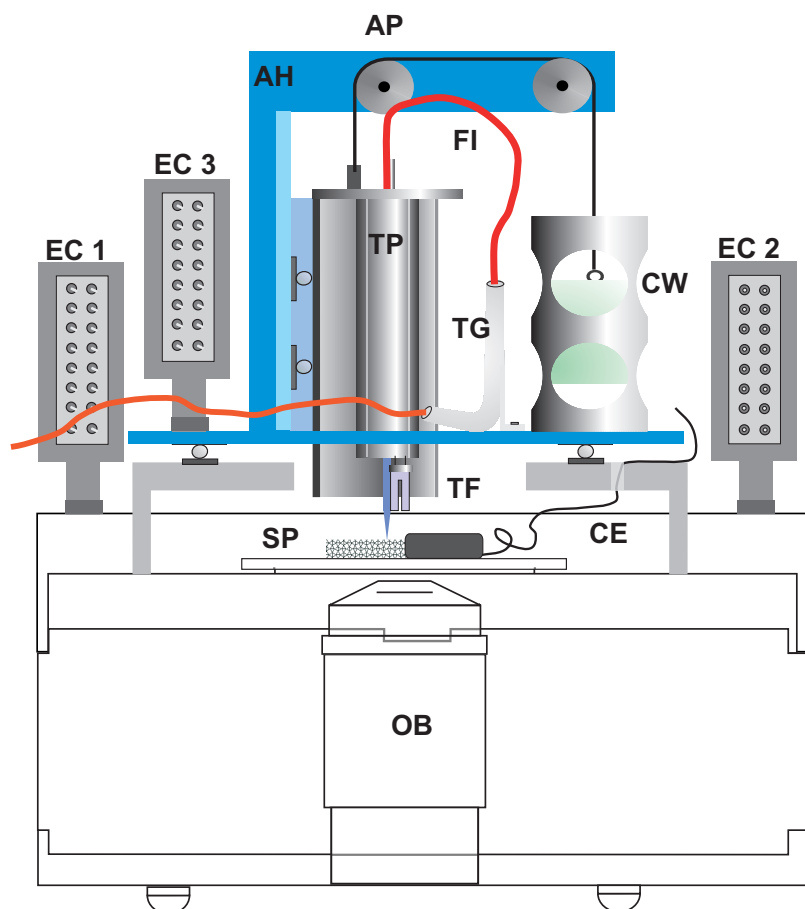
Figure 3.8: Side view of the scanning-tip unit, which is placed on top of the confocal microscope. The bulk unit hosting the objective (OB) is outlined at the bottom. Above the objective, a disk piezo with the sample holder (SP) is positioned. The sample holder can be grounded (CE) to act as a counter electrode to the tip. The scanning-tip unit rests on a slip-stick device on top of the objective. EC 1-3 are three electrical 16-pins connectors. The fiber (FI) tip is attached to the tuning fork (TF). The fiber end is guided through the tube piezo (TP) and a small metal tube (TG) towards the outside. The tube piezo (TP) scans the tip. It can be approached through a hole in the base plate of the tip unit to the sample (SP). The approach of the tip is done by a vertical slip-stick device. A counter weight (CW), which is attached to the tube piezo by a thin Kevlar thread, is necessary for a smooth movement upwards. The Kevlar thread is guided by two pulleys (AP) mounted on an arm-shaped holder (AH).

tip unit go to the 16-pin electrical connector (EC 3), mounted on the movable base plate of the tip unit. This cable guiding system avoids entanglements of cables and guarantees free movements of the tip unit. The base plate of the tip unit rests on the slip-stick positioning unit, which has been introduced in section 2.5.2. The whole tip unit can be positioned precisely in the μm-range above the objective. The base plate of the tip setup has a round hole in the center through which the tip, attached to a tuning fork (TF), can be approached to the sample (SP). A detailed description of the tip preparation follows in section 3.2.2. The glass fiber also has to be guided to avoid entanglement. Therefore, the fiber (FI) goes through the tube piezo (TP) and is afterwards guided through a metal tube (TG) to the side. By using a fiber coupler, the etched glass fiber is connected to another glass fiber to the outside. The tube piezo serves as scanning element for the tip. The approach of the tip to the sample is also based on slip-stick motion. Here, the slip-stick drive is vertically mounted on an arm-shaped holder (AH). The scanning unit, tube piezo with tuning fork and tip, hangs on a thin thread (Kevlar29), which goes over two pulleys (AP) to the counter weight (CW). The counter weight is necessary for a smooth movement in vertical direction. The mechanism for the positioning and the approach is explained later in section 3.2.3.

Tip preparation

The choice of a suitable tip has been critical. On the one hand, the tip should have the smallest diameter possible to ensure a high electric field gradient. This requirement would be perfectly satisfied with an etched metal tip, where diameters of 10 nm can easily be reached. On the other hand, the tip has to be positioned over the objective, a process which requires visual control through the microscope objective. The easiest way to achieve this is to use glass fiber tips covered with a transparent metal layer. With this design, light can be coupled into the glass fiber and the transmitted fraction of this light can be observed via a video camera. This signal can be used for positioning of the tip. Even though the metallized glass-fiber tips do not have a tip diameter as small as bulk-metal tips ($\sim$60 nm in the best case), the glass tips have been chosen for the sake of an easier positioning procedure inside the cryostat. Another disadvantage of these glass tips, beside the larger tip diameter, is the fact, that even smaller damages of the tip render it useless for further Stark-shift measurements, since the metal layer is rubbed off. Such damage could occur during the cool-down procedure (thermal forces acting on the thin metal layer) or, in a more destructive way, by an incautious approach to the sample. Therefore, immense care has to been taken in preparing and in handling such metallized glass-fiber tips.

The preparation of the glass-fiber tips is done by the tube etching process [93]. Thereby the protecting plastic coating of the glass fibers acts as a capillary for the acid. This capillary effect results in sharp tips inside the coating tubes. The etching is done by dipping the glass fibers in a teflon pot filled with HF acid (40%) with a
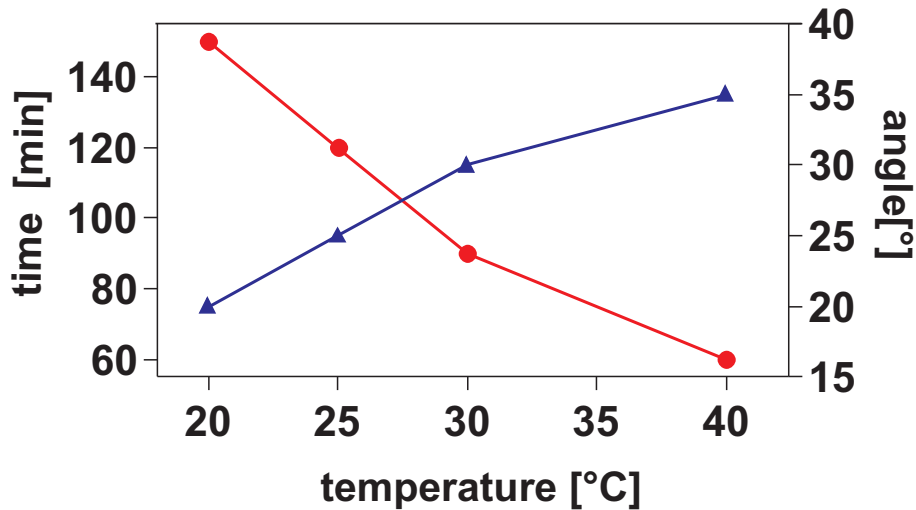
Figure 3.9: Guideline for the time required for tip etching at different temperatures. The temperature has also an impact on the opening angle of the tip. Graph based on the experience of J. Toquant.

thin over layer of trimethylpentane. The pentane layer avoids acid vapor acting on the metal of the fiber holder. The etching time depends on the ambient temperature. The higher the temperature, the shorter is the time for the etching process, see Fig. 3.9. The opening angle of the tip depends also on the temperature. The lower the temperature, the larger is the opening angle. However, the opening angle has not been a critical parameter for the Stark-shift experiment. After the etching, the plastic coating is removed by dipping the fiber tips in hot sulfuric acid (95-97%). The acid is washed off by leaving the tips in pure water.

After the etching procedure the metallization process follows. There are several requirements, that the metal layer has to fulfill. First of all, the metal layer has to be thin. A thin metal layer ensures transparency and is required for the positioning the tip inside the cryostat. A thin metal layer also ensures a small final diameter of the tip. Even though it is thin, the electrical resistance of the metal layer, should be still comparably low (in the range of $k\Omega$). Otherwise a high voltage has to be applied to produce a strong enough electric field. The metal should also not oxidizes too fast. In the case of a too thin layer, it might happen, that the complete layer becomes non-conducting because of oxidation. For a well defined field at the apex of the tip, a smooth, not a grainy surface is preferred.

For the metallization process, thermal evaporation or sputtering have been used. As materials, mainly Aluminium or Silver has been evaporated. The thickness of the metal layer has been varied between 20nm and 60nm. The thickness of the evaporated metal layer has been measured by a quartz crystal balance. The measured metal thickness is only an estimation, since the distance and the orientation of the tips and the quartz to the evaporation source are different.
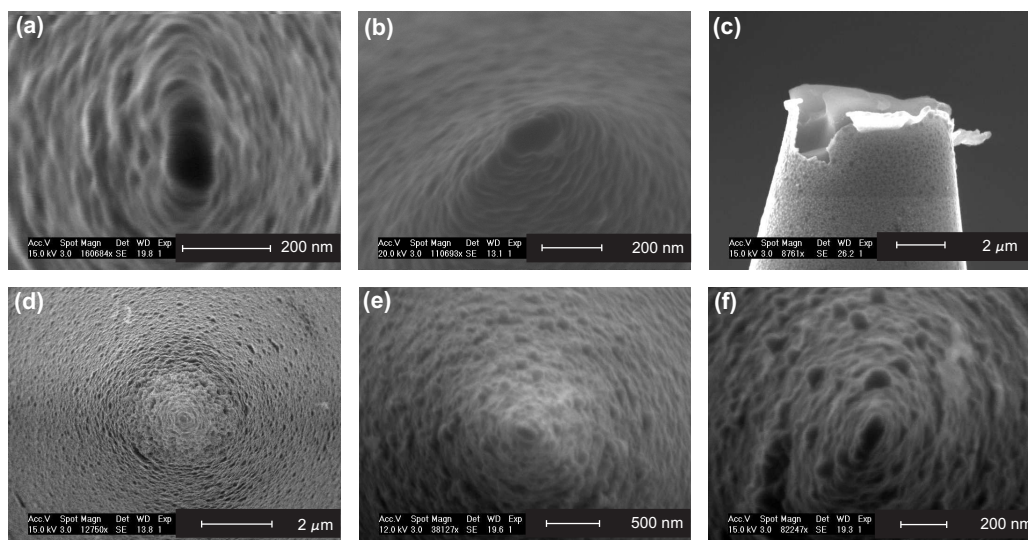
Figure 3.10: SEM images of different tips. (a) Top view of glass tip, evaporated with 30nm of Al. (b) Tilted view of the same tip. (c) Side view of a Ag tip after an experiment, where the tip has been crashed. The metal thickness is supposed to be 40nm, but the SEM picture reveals a thickness of 65nm. (d)-(f) Top view of different glass tips with different scales and thicknesses,(d) 20nm Ag, (e) 40nm Ag and (f) 40nm Ag.

The metallized glass-fiber tips typically have a resistance in the range of kΩs and a tip diameter ranging from 30nm up to 100nm. The shape of the tip after the metallization process, has been very often irregular. In Fig. 3.10, SEM pictures of varies tips are shown. First of all, it is apparent that the surface is grainy. However, since the tip apex is normally formed by a single grain, the surface of the tip cone does not matter very much for the experiment. The tip apex itself has an elliptical shape instead of a round one. This form, indeed, can have an influence on the experimental results, since the electric field shape defines the fluorescent pattern of the molecules. Nevertheless, the influence of the elliptical shape has hardly ever been seen in the experimental data. Fig. 3.10 (c) shows a crashed Ag tip. The thickness of the metal layer is supposed to be 40 nm (according to the quartz), but in the SEM image, it looks more like 65 nm. The thickness of the metal layers is thicker by a factor of ~1.6.

Electrical contact to the tip

One of the main difficulties of the tip setup has been to guarantee a good and reliable electrical contact to the tip even at low temperature. Another important point has been the insulation of the metallized part of the glass fiber from the tube piezo, through which the fiber is guided. The design was supposed to be simple and suitable for low temperature. It also had to be light to avoid extra weight for the approach mechanism, since the slip-stick motion is very sensitive to small changes of the weight.
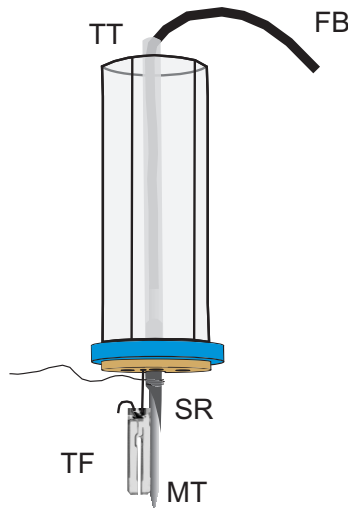
Figure 3.11: Electrical connection to the metallized tip (MT), which is glued to the tuning fork (TF). The fiber (FB) passes through the small piece of a syringe (SR) to which the wire is glued. The fiber then is guided through the tube piezo (transparent). The metallized part of the glass fiber is insulated from the inner electrode by a teflon tube (TT).

Last but not least, the contacting procedure has to be fast, since the fiber tip cannot be stored in air for a long time to avoid damages or contaminations.

A close-up of the scanning tube piezo element is shown in Fig. 3.11. The tube piezo is sketched transparent. A round plate is glued at the bottom of the piezo, to which the tuning fork is attached. For the electrical insulation of the tip from the tube piezo, a thin teflon tube has been used. The teflon tube is obtained by stripping off the teflon coating from an electrical wire commonly used for low temperature. The length of this teflon tube is longer than the tube piezo itself, so that it sticks out a short distance at the top and at the bottom of the tube piezo. To achieve an electrical contact, a piece of a metal syringe is inserted at the lower end of the teflon tube. A wire is attached to the syringe by using a conducting two-component glue (Epo-Tek E4110). The wiring to the syringe could be done before attaching the tip. The wired syringe could be used for many runs of the experiment. The fiber has just to be pushed through the metal and the teflon tube. This construction shortens the contacting procedure considerably. The sharp end of the syringe offers a kind of groove in which the metallized fiber lies. Finally, the tip is glued to the tuning fork by a small drop of UV drying glue. The tuning fork, which is attached with only one leg to the tube piezo, could be slightly bend in such a way, that the fiber is pressed even more against the metal groove of the syringe. By adding a little droplet of silver paint on the groove, a good electrical contact (R $\sim$ few kΩ) to the tip is obtained.

For applying the voltage to the tip, a power supply is connected to the tip. Since for the first experiment there has not been a counter-electrode on the glass plates,
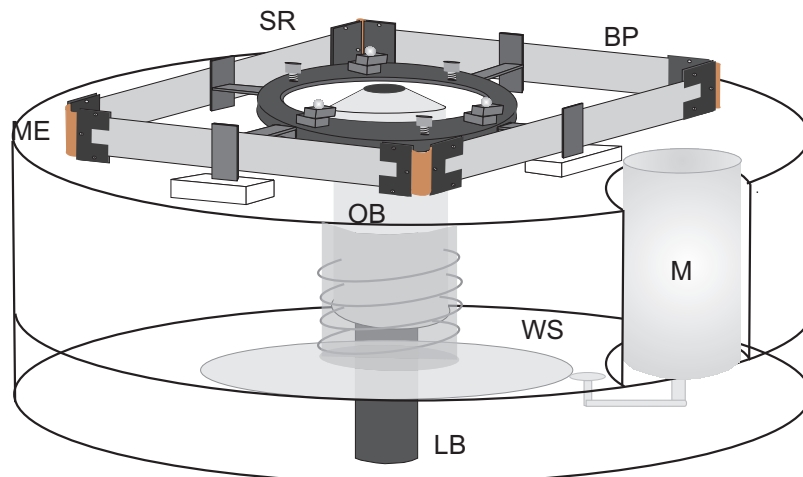
Figure 3.12: The scan unit of the confocal microscope. The bulk unit, which hosts the microscope objective, the scanner and the sample holder (not shown here), is drawn transparent. Starting from the top, the three sapphire balls on piezo stacks and the three magnets form the slip-stick device for the sample positioning. The black ring (SR) itself rests on the four bimorph piezos (BP), which are hold together by flexible, metal edges (ME). This is the scanning unit for the sample above the objective (OB). The objective can be moved up and down by a motor (M) (visible on the side) connected by a tooth-wheel system (WS)

the voltage has to be quite high to induce enough charges on the tip. The power supply has been a high-voltage amplifier, which could be controlled externally by a potentiometer. The amplifier has a voltage range of $U = \pm 400$ V.

3.2.3   Focussing and positioning possibilities

The setup offers a large variety of scanning and positioning possibilities. In the following an overview is given, how each element in the setup can be adjusted to a desired position. Generally, there is for each degree of freedom a coarse and fine positioning available (for a summary see table 3.4). A sketch of the positioning elements is shown in Fig. 3.12 for the confocal microscope and in Fig. 3.8 for the scanning-tip unit.

Focussing of the laser

For confocal imaging, the laser has to be focussed onto the sample (Fig. 3.12). Coarse focussing is done by moving the objective by a stepper motor (Princton Research Instrument, size A), which is suitable for high-vacuum and low temperature operation. The the motor (M) drives the objective by a tooth-wheel system (WS). The drawback of this system of operation are the vibrations introduced by the movement of the stepper motor. These vibrations can even cause a shift of the whole tip setup, which is placed on top of the confocal microscope (see Fig. 3.8). Therefore, after the

element to move	direction	purpose	element	adjustment	control
objective	z	focus laser light on sample	stepper motor	rough	external control unit
sample	z	focus laser light on sample	disk piezo	fine	potentiometer
sample	x,y	changing sample area	shear piezo	rough	joystick
sample	x,y	scanning sample	bimorph piezo scanner	fine	computer
sample	x,y	positioning sample over objective	bimorph piezo scanner	fine	computer
tip unit	x,y	positioning tip over objective	shear piezo	rough (fine)	joystick (computer)
tip	z	tip approach	shear piezo	rough (fine)	joystick (computer)
tip	x,y	scanning tip	tube piezo	fine	computer

Table 3.4: Overview of the piezo elements and their functions.

positioning of the tip is accomplished, the motor cannot be used anymore. The fine positioning of the focus is done by a disk piezo-element (Piezomechanik, CBM100/35-35/070), on which the sample holder is placed. The principle of a disk-piezo has been introduced in chapter 2.5.2. The position of the sample holder (SP) on the disk piezo (DP) is sketched in Fig. 3.13 (a) in a side view. By using the disk piezo, the sample can be moved in z-direction to adjust the focus in the range of $\pm 30\,\mu$m at room temperature (manufacturer information) and about $\pm$ 200nm at low temperature (estimation by own experiences). The room temperature range is probably less, since the center hole of the disk-bender had to be enlarged for the sample holder.

Positioning and scanning of the sample

In Fig. 3.13 (a), a side view of the stark-shift microscope is shown, where the slip-stick drive (shear piezo, Staeveley, EBL#2, PSI-5H4G) for the horizontal positioning of the sample (SP) on the disk (DP) is highlighted. In the side view, the shear-piezos with little sapphire balls on top are visible. The slip-stick drive has been introduced in section 2.5.2. The scanning of the sample is done by a piezoelectric bimorph-scanner (shear piezos, Piezo Systems, T220-H4 SS-X). The functioning of the bimorph scanner has been introduced in section 2.5.2.
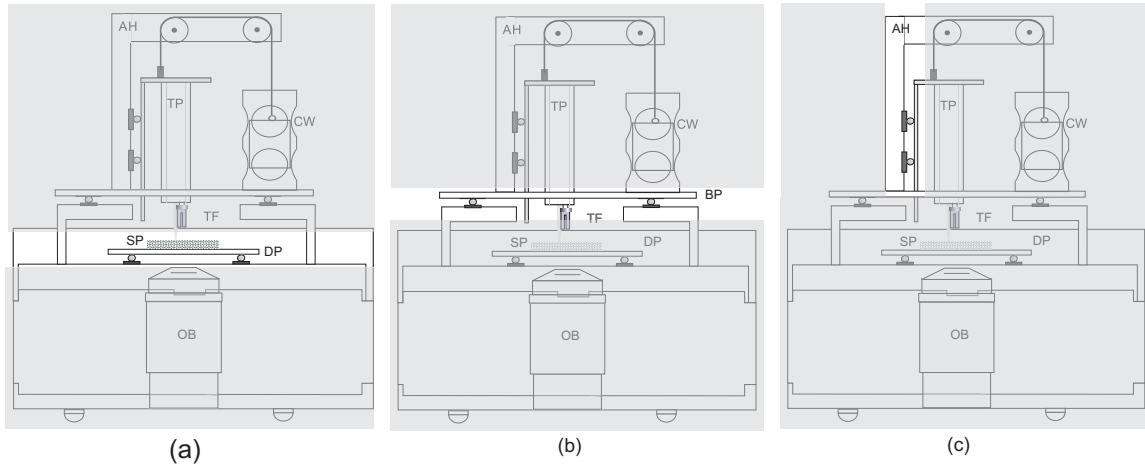
Figure 3.13: Side view of the Stark-shift microscope with the three different slip-stick motion drives highlighted. The slip-stick devices consist out of shear-piezo stacks with little sapphire balls glued on top. (a) Horizontal positioning of the sample (SP) and the disk piezo (DP). (b) Horizontal positioning of the tip (TF) by moving the whole scanning tip unit mounted on the base plate (BP). (c) Vertical approach of the tip (TF).

Positioning and scanning of the tip

The positioning of the tip is achieved by following a protocol: First, the tip has to be positioned horizontally over the objective. In a second step, the tip has to be approached towards the sample and finally, the tip has to be scanned over the sample.

The lateral positioning of the tip over the objective is done by moving the whole tip setup by slip-stick drive. In Fig. 3.13 (b), the slip-stick drive for the horizontal movement of the scanning-tip setup, mounted on the base plate (BP), is highlighted. The weight of the tip setup is already enough to ensure a reliable slip-stick motion. No magnets are necessary to provide an additional force between the sapphire plate and the sapphire balls. In the case of the tip positioning, there is no additional possibility for a fine positioning. This problem has been solved by a 'fine' tuning of the movement over the electronics. A single pulse can be send to the shear piezos in such a way, that a single slip-stick step is possible. Together with the tuning of the amplitude of the pulse, a finer positioning of the tip over the objective is possible.

For the vertical approach of the tip towards the sample another slip-stick drive is used. The design is discussed in detail in [65]. An anodized aluminium holder, hosting the tube piezo with the fiber tip, runs directly over four sapphire balls arranged in vertical orientation, as highlighted in Fig. 3.13 (c). A thin steel bar is screwed to the back of the aluminium holder and guarantees the attractive interaction with the magnet. The magnet are mounted between the four stacks of piezos used for the slip-stick motion. Since the magnetic attraction is not enough to guarantee an upwards

movement, the aluminium holder hangs on a thin thread connected to a counter weight (CW). The counter weight is slightly lighter than the aluminium holder with the tube piezo. The vertical slip-stick drive has been used to bring the tip in shear force contact with the sample [66]. The same electrical 'fine' tuning as for positioning the tip in the horizontal direction is applied. Sending just a single pulse to the shear piezos guarantees a fine approach.

Finally, the scanning of the tip is accomplished by a tube piezo (TP) (Staveley, EBL#2, 4 outer electrodes). The function of a tube piezo has also been explained in section 2.5.2. The tube piezo with the tuning fork and the tip attached to it, can be scanned in a range of $5 \times 5\mu$m at cryogenic temperature.

Approach control of the tip

The approach of the tip has been controlled by a tuning fork shear force system [66]. This sensitive approach mechanism has been introduced in section 2.5.3. However, the attachment of the tip to the tuning fork combined with the electrical contact raises some problems. The fiber is attached at too many points and the resonance of the tuning fork is damped to almost zero. Because of this strong damping, the observation of the tip approach has been changed. The gap-width can be roughly controlled by a visual observation of the transmitted laser light through the tip. The light, transmitted through the fiber, is observed through the objective on the video camera. The procedure is carried out as follows. First, the reflection of the sample is brought in the focus and the position of the reflection is marked on the screen of the camera. Then, by flipping the mirror (FM1, Fig. 3.7), the light is guided through the fiber. The fiber is approached until the transmitted laser spot from the tip apex is also in the focus. The tip is moved in plane until the transmitted spot coincides with the marked spot of the screen. This way of approach has the drawback, that one assumes that the light escapes at the very apex of the tip. If light comes out at the apex side, the fiber is crashed during the approach. Furthermore, each fiber shows another pattern if positioned in the focus. The pattern of the transmitted spot has to be investigated at room temperature without the sample, to get a feeling for the right moment to stop the approach.

Calibration of the scan range

The bimorph-sample-scanner is calibrated by using a test pattern. A silicon grating is imaged in back-reflection mode with different scan ranges. The low-temperature scan-range is estimated by assuming it to be 10% of the room-temperature range. The scan range at low temperature is determined to be 10μm$\times 10\mu$m. For the tube piezo, only the low temperature scan range is of interest. The back-reflection pattern of a chess-board patterned silicon grading with known dimensions is imaged on the screen of the video camera. The scan range of the tip has been also measured on the video by observing the transmitted laser light on the screen. By comparing the scan
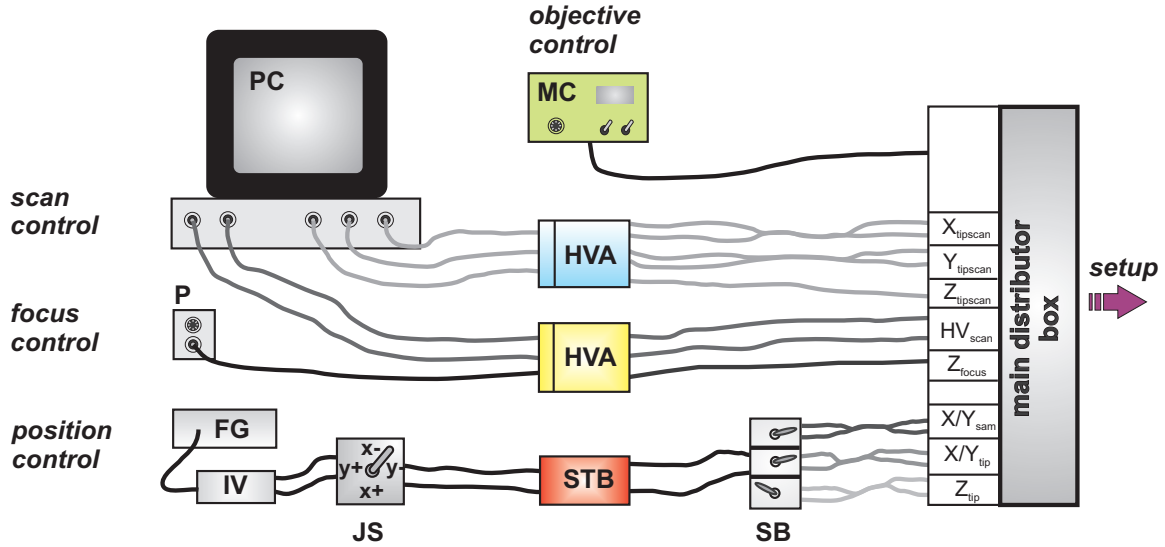
Figure 3.14: Overview over the electronic control system. The scan control is done by the computer (PC). The objective has its own control box (MC). The adjustment of the disk piezo is done by a potentiometer (P). HVA1 and HVA2 are high voltage amplifiers and STB is a saw-tooth booster, which amplifies the signal for the piezo-elements. FG is a function generator and IV is a voltage converter. JS is a joystick for the slip-stick motion control of the shear piezos. SB is a switch box to avoid cross talks between the different shear piezo drives. All cables come together in a main distributer box, from where they are guided to the cryostat.

range of the tube piezo with the imaged pattern of the silicon grating, the scan range of the tube piezo is determined. The maximum scan range of the tip is 5μm$\times 5\mu$m.

Electronic control system

The remote control of the positioning elements is done electronically. The control of the piezo elements is partly taken over by the computer, partly done by hand, see Fig. 3.14. The stepper motor of the objective has a control box of its own, the objective control (MC). From there, the objective can be driven up and down continuously, in single or half-steps. The control of the scans (scan control in Fig. 3.14), either for the bimorph-sample-scanner (two electrical connections) or the tube-piezo tip-scanner (three electrical connections), is carried out by the computer program of the PC. The electronic cable connections and driving signals of the different piezoelectric elements can be described as follows:

- **tube piezo (blue mark):** From the computer, the signal for the tube piezo goes to the high voltage amplifier (HVA1) and then over the cable-divider box ($X_{tipscan}$, $Y_{tipscan}$, $Z_{tipscan}$) to the setup. There are four signals (ramp-formed) for the 4 outer segments of the tube piezo (X,Y) and one signal (constant) for the inner electrode (Z).

- **bimorph scanner (yellow mark):** The driving signal for the bimorph-scanner goes from the computer to a second high voltage amplifier (HVA2) and then over the cable-divider box (HV$_{\text{scan}}$) to the setup. The piezos are driven in pairs. One pair is driven continuously with a ramp-like signal for performing a line-scan of the sample. The second pair is driven with a constant voltage signal, which is increased after each line-scan of the first piezo-pair. In this way, a 2-dimensional scan of the sample is achieved. For the movement control, see section 2.5.2.

- **disk piezo (yellow mark):** The control of the disk piezo has a potentiometer with which the output of the high voltage amplifier (HVA2) to the piezo (Z$_{\text{focus}}$) is adjusted.

- **shear piezos (red mark):** A function generator sends out the ramp-like signal which is also inverted (IV). Both signals are controlled by a joystick (JS), to address the four directions of a piezo-stack for slip-stick motion independently. The saw-tooth booster (STB) amplifies the signal. There is a switch box (SB) to address only one of the three slip-stick motion systems (sample positioning, tip positioning or tip approach). The switch box avoids cross talks between the different slip-stick devices. Afterwards, the sample (X/Y$_{sam}$), or the tip unit (X/Y$_{tip}$) can be positioned, or the tip can be approached to the sample (Z$_{tip}$).

3.2.4 Data acquisition

The data acquisition is done by a computer and a commercially available software. The first software has been the control program ECS, DSP-Scan6.0. Even though this software is designed to control a STM or AFM, the functions can be used to control an optical microscope. The program is able to read in the signal of the APD and to control the movement of the two scanners separately (the sample scanner and the tip scanner). The sample scanner and the tip can be put to a desired and fixed position. The laser frequency can be driven as a continuous frequency sweep or set to a fixed value. There is also the possibility to control the approach of the tip by the tuning fork shear force signal (amplitude sensitive). The data acquisition has been changed to a labview 6.1 system later on (National Instruments, NI PCI-6229 Mseries).

3.2.5 Cryogenic setup

A liquid helium bath cryostat is used for cooling the Stark-shift microscope down to cryogenic temperature. The design of the cryostat has to be suitable for optical measurements. Therefore, two windows are built into the bottom plates of the cryostat,

allowing optical access to the setup. Since the optical path goes through the helium bath, spectroscopic measurements are not possible as long as the liquid helium is above the boiling point. Liquid Helium below T=4.2 K has a gas-like index of refraction of n=1.026, which is close to the one of air (n=1). Optical measurements are only possible in the superfluid state of the liquid helium, which is reached by reducing the pressure above the helium bath. This direct pumping on the helium bath is the most ineffective way of cooling, but it is a fast method for cooling the massive setup and produces a homogeneous temperature distribution during measurements.

The cryostat itself is divided into three layers, the helium chamber (1), the nitrogen shield (2) and the vacuum thermal-isolation chamber (3), as shown in Fig. 3.15. The inner chamber serves as the liquid-helium chamber and the setup chamber. The microscope is immersed completely in the liquid-helium bath. The top plate of the cryostat hosts the openings for the helium transfer line, for the liquid helium level meter (AMI, Model 135) and for the electrical connections to the setup. One of the two windows, W1, is built into the bottom plate of the setup chamber for optical access. The first window W1 is in direct contact with the helium bath, which puts a high thermal stress on the glass and the sealing. Regular exchanges have been necessary.

The insulation of the liquid helium chamber from the outside is accomplished by a combination of a vacuum chamber (3) and a liquid nitrogen shield (2), as shown in Fig. 3.15. The vacuum chamber is connected to a turbo pump. The pressure is kept on the order of $p \sim 10^{-7}$mbar. The second window W2 is built into the bottom plate of vacuum chamber (3). The liquid nitrogen shield (2) is embedded inside the vacuum chamber (3) and surrounds the liquid helium chamber (1). Liquid nitrogen can be filled in through three openings in the top plate of the cryostat. The nitrogen shield is connected to the helium chamber by a copper plate CP shortly below the top of the cryostat. This copper plate CP is the only thermal connection of the setup chamber to the liquid nitrogen, which allows a kind of pre-cooling the setup. For a description of the cooling procedure, see Appendix A.2. The nitrogen shield is elongated by a brass cylinder BC for thermal shielding. This brass cylinder BC reaches around the lower extended part of the helium chamber and has a hole at the position of the window.

There is a main disadvantage of this cryogenic assembly. If the liquid helium level falls below a certain height, the piezo elements of the setup are driven under low-vacuum conditions. Under these conditions, breakthroughs at the piezo elements can appear, which can damage or even depolarize the piezos. Even though great care has been taken, a regular exchange of the piezo elements has not been avoidable.

The temperature of the setup is measured by a thermometer (Lakeshore, silicon diode DT-670C-SD). At first, the diode has been mounted on one of the 16-pin
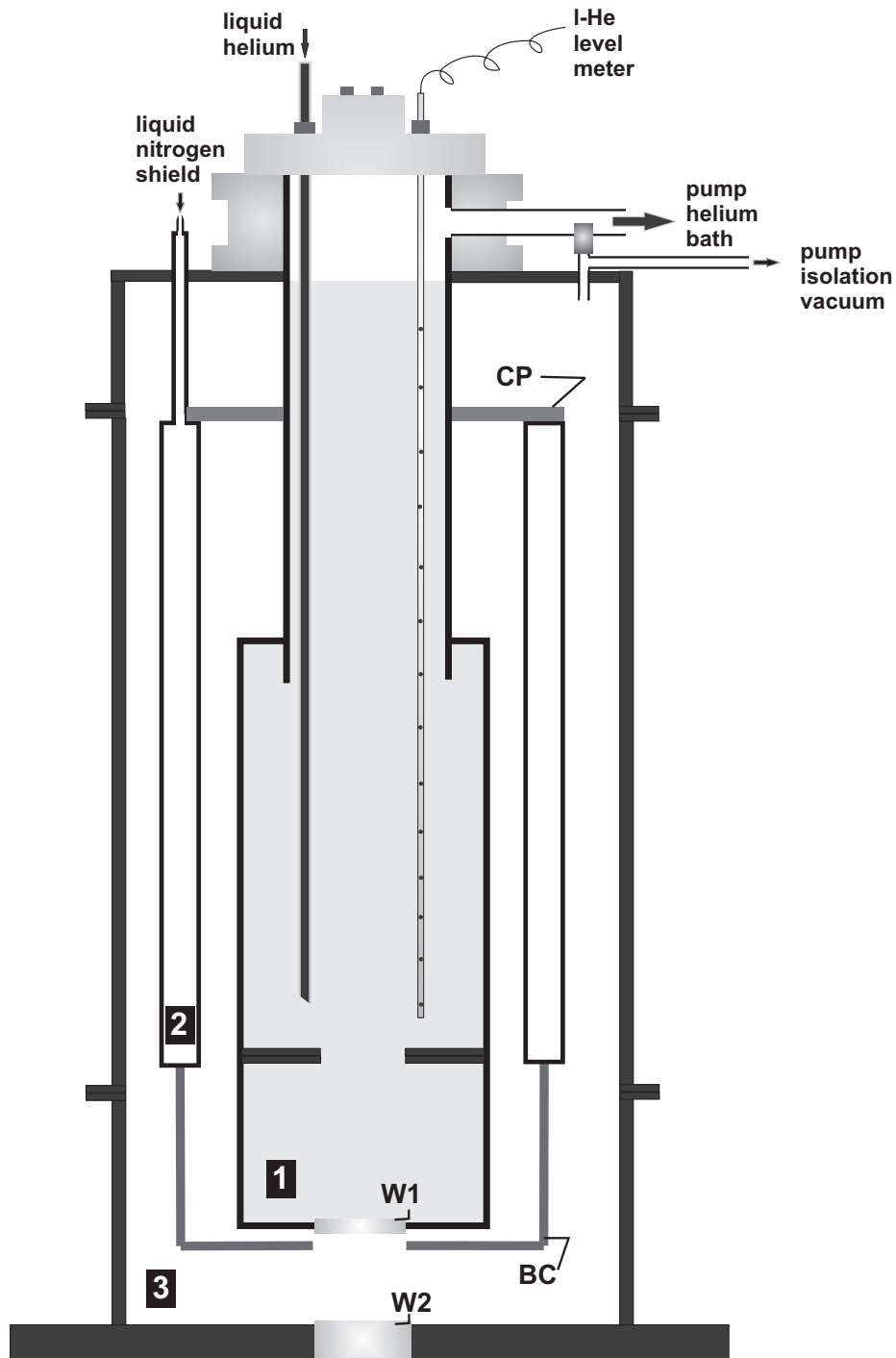
Figure 3.15: Liquid helium bath cryostat. (1) is the liquid helium and setup chamber. On the top plate, the openings for the liquid helium level meter and the liquid helium transfer line are shown; the connection to the liquid helium pump is sketched on the side of the top plate. In the bottom of the liquid helium chamber, one window W1 is mounted. (2) is the liquid nitrogen shield, whereas at the bottom, a brass extension BC has been mounted. The nitrogen shield is connected to the setup chamber by a copper plate CP for a kind of pre-cooling. (3) is the vacuum chamber for further thermal insulation. The connection to the turbo pump is on the top plate. Inside the bottom plate, there is the second window W2 mounted.

Figure 3.16: Confocal imaging. (a) Sketch of the experimental setup. Excitation frequency is set to a fixed value and the sample is scanned over the objective. (b) Spectral range: Laser excites all molecules inside the focal volume, whose resonances are spectrally close. (c) Typical confocal image of a sample at low temperature. Several molecules are excited within the scan range of the sample-scanner.
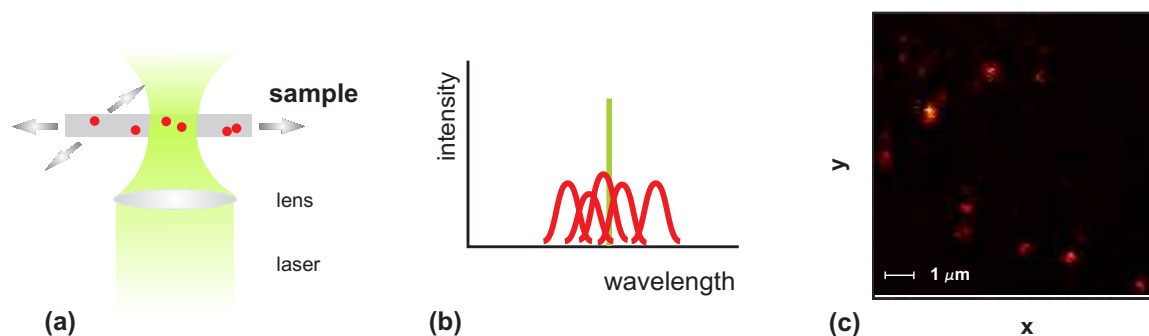
electrical connectors of the scanning tip-unit. Later on, the diode has been placed on a marcor-connector shortly below the sample holder. In this configuration, the diode should have been sensitive to the level of the liquid helium. Unfortunately, the diode has not been sensitive enough to measure the drop of the liquid helium accurately.

3.3   Performance of the setup

In the following, each possibility of acquiring data is discussed separately to provide an overview of the different abilities of the experimental setup. This section will be useful as a guideline during the discussion of the results. The presentation of the experiments is accompanied by figures which are divided in three parts. Part (a) shows a sketch of the experimental setup, part (b) illustrates the measurement within the spectral region, and part (c) shows a typical image obtained with such an experiment. In the sketches of the setup (a), the part of the setup which is moved or changed during the experiment is indicated by bold letters. The images, shown in the illustrations (c), are data taken at low temperature.

Confocal imaging

For confocal imaging, the sample is in focus and is scanned in x,y-direction over the objective, as shown in Fig. 3.16 (a). The narrow-band laser is set to a fixed frequency. A single molecule can be detected, if it is inside the focal volume and spectrally close to the excitation laser as sketched in Fig. 3.16 (b). Especially at low temperature, the narrow line width of the excitation laser combined with the narrow line width of the molecules makes it very difficult to find suitable molecules. A typical confocal image at low temperature is shown in Fig. 3.16 (c). The molecules are detected as bright and dim fluorescent spot. This method is diffraction-limited. Confocal microscopy with a narrow-band laser detects single molecules with similar resonance frequency,
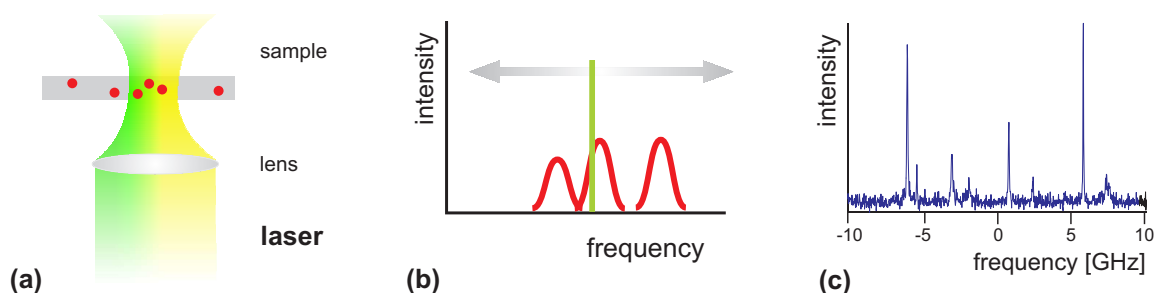
Figure 3.17: Excitation spectrum. (a) The sample is kept at a fixed position and the laser is scanned over a range of frequencies. (b) Several molecules, which are located inside the laser spot and have different resonance frequencies, are addressed one after the other. (c) Typical excitation spectrum at low temperature, where each peak corresponds to a single molecule.

but distributed over a spatial area.

Excitation spectrum

In contrast to the confocal imaging, excitation spectra detect single molecules, which differ in their resonance frequencies, but are located within the same diffraction limited laser spot, (see Fig. 3.17 (a)). The sample is fixed at one position and the laser is scanned over a certain frequency range as shown in Fig. 3.17 (b). The maximum frequency scan range of our laser is 30 GHz. The fluorescence of all molecules inside the focal volume and within the frequency scan range is detected and measured as a function of the excitation frequency of the laser. The output is an excitation spectrum as shown in Fig. 3.17 (c). The single molecules are addressed one after the other by the narrow-band laser. Each peak corresponds to a resonance of one molecule.

Excitation spectrum over time

Excitation spectra can be taken as a function of time. As before for measuring the excitation spectrum, the sample is fixed in one position, and the excitation laser is scanned, as shown in Fig. 3.18 (a) and (b). In contrast to a single excitation spectrum, data acquisition is done in a 2-dimensional image. On the x-axis the excitation frequency is recorded. The y-axis is the time-axis. In this way, the stability of the single molecule can be investigated, as shown in Fig. 3.18 (c). Each bright line corresponds to a single molecule. Only one of the detected molecules inside the focal volume is stable over the detection time and shows an uninterrupted line. Two molecules show strong blinking behavior and are not stable during the imaging time. They show a line-signal which is interrupted by dark periods. One of these two blinking molecules even photo-bleaches or jumps outside the excitation range. On the very right side of the image, two very weak molecules are visible. These two molecules sit probably at the edge of the confocal volume or are off-resonant and can hardly be excited at all.
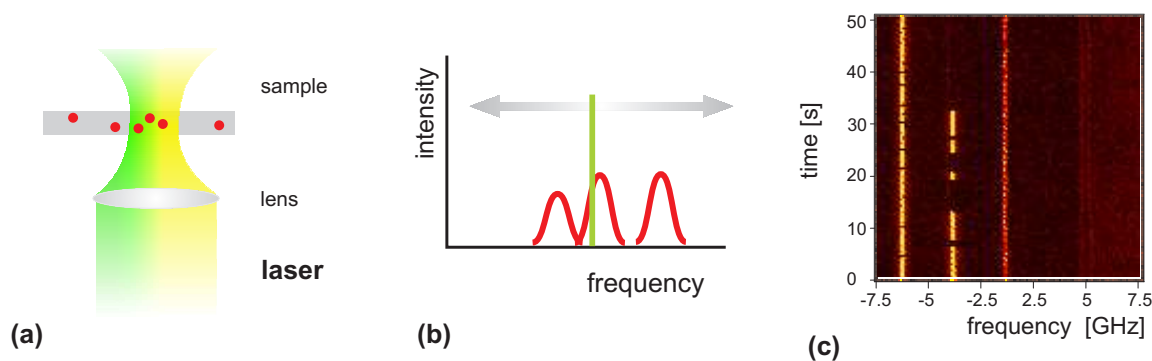
Figure 3.18: Excitation spectrum over time. (a) Sample is kept fixed at one position and the laser is scanned over a range of frequencies. (b) Several molecules, which are located inside the laser spot and have different resonance frequencies, are addressed one after the other. (c) Spectra are measured in a 2-D image, where the x-axis shows the excitation frequency of the laser and the y-axis is the time-axis.

Excitation spectrum depending on tip voltage, part1

In the following experiments, the Stark shift of molecules is investigated. The sample is fixed in one position with at least one molecule in the focus. The biased tip is approached towards the sample. Afterwards, the tip is fixed at one position, Fig. 3.19 (a). Scanning the laser frequency, a regular excitation spectrum is taken. Changing the voltage on the tip after each spectrum, the Stark shift of the molecules, located inside the focal volume, can be detected (see Fig. 3.19 (b)). The outcome of such an experiment is shown in Fig. 3.19 (c). The voltage is increased from top to bottom ($V_1 < V_2 < ... < V_n$). Three peaks, corresponding to three single molecules, are detected in the spectrum. The resonances of the molecules shift due to the induced Stark shift to lower frequencies. One of the molecules (high intensity) shows a smaller Stark shift as compared to the second molecule (lower intensity, broad peak), which runs from the right to the left side of the first molecule. With this kind of measurement, the linear and quadratic component of the Stark shift of a single molecule can be measured.

Excitation spectrum depending on tip voltage, part2

There is a faster way of imaging the Stark shift of single molecules at one spot of the sample. As before, the sample as well as the biased tip are fixed at one position (see Fig. 3.20 (a)). The excitation laser is scanned in frequency and the voltage of the tip is changed after each frequency scan, Fig. 3.20 (b). By recording the spectra as a 2-dimensional image over the stepwise changed, applied voltage, the Stark shift can be visualized as shown in image 3.20 (c). The image shows the resonance of a single molecule shifting to higher frequencies under the applied electric field. The molecule shows a dominant linear Stark effect.
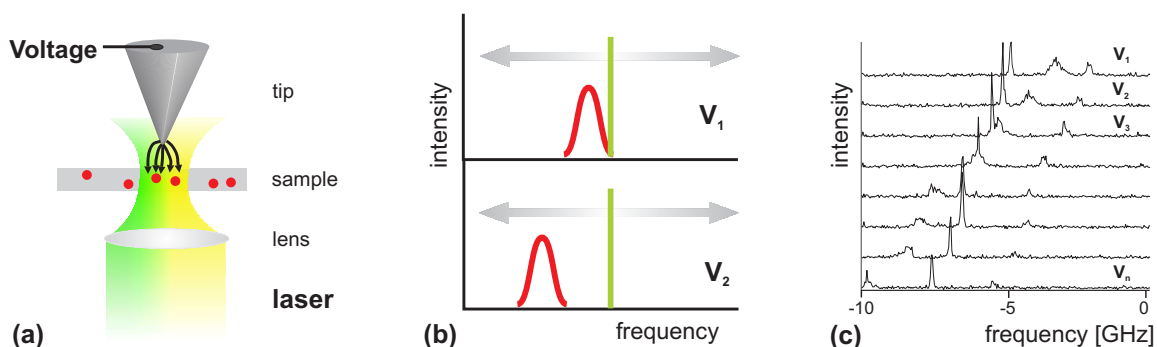
Figure 3.19: Excitation spectra as a function of applied voltage. (a) The sample and the biased tip are kept at a fixed position, the laser is scanned in frequency and the tip-voltage is changed after each frequency scan. (b) Recorded spectra depending on the tip-voltage. The resonance of the molecule is shifted by the electric field. (c) Several spectra are shown, where the voltage has been increased after each frequency scan (increasing voltage from top to bottom). The resonance frequencies of the three molecules are shifted towards lower excitation frequencies.
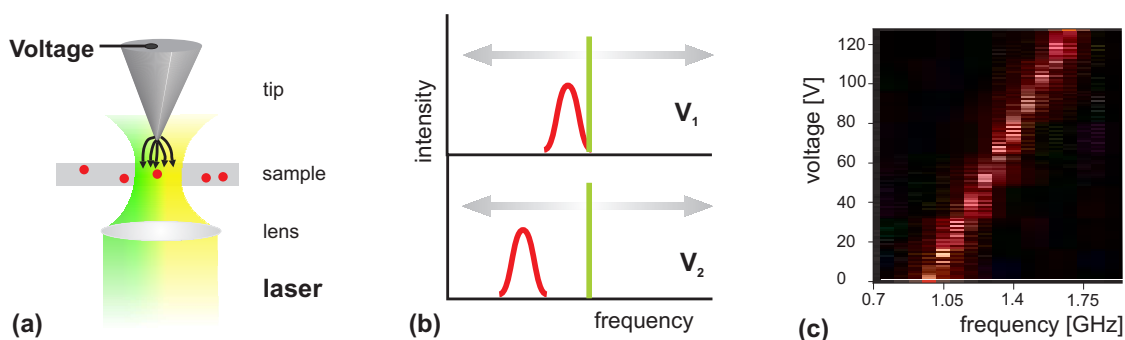
Figure 3.20: Excitation spectra as a function of applied voltage recorded as a 2-D image. (a) The sample is kept at a fixed position, the laser is scanned in frequency and the voltage applied to the tip is changed after each line. The tip is kept at a fixed position. (b) Changing spectra after the voltage on the tip has been changed. The resonance of the molecule is shifted by the electric field. (c) Recording of the excitation spectra as a function of applied voltage in a 2-D image. The x-axis is excitation frequency is plotted on the , and the y-axis is the tip voltage. The Stark shift of the detected single molecule has a dominated linear component.

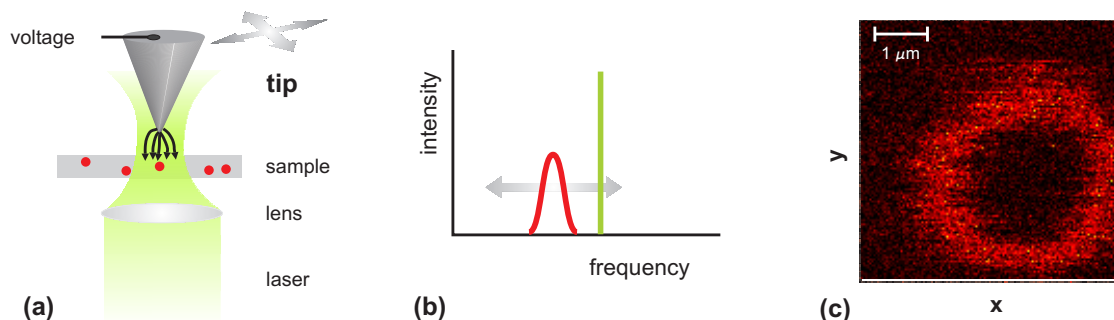Figure 3.21: Stark-shift imaging. (a) Position of the sample, excitation frequency and the tip-voltage are kept fixed. The biased tip is scanned over the confocal volume and pushes the molecule in and out of resonance with the laser. (b) The excitation frequency of the laser is kept fixed. By scanning the sample, variable Stark shifts are induced to the molecules. At certain tip positions, the Stark-shift of the molecule is large enough to shift the ZPL in resonance with the laser. (b) Typical Stark-shift image of a single molecule. The fluorescence pattern are discussed later on.

Stark-shift imaging

Finally, the Stark-shift imaging technique is discussed. The sample is fixed in one position. The excitation laser is fixed at one frequency, which is not in resonance with the molecule. The tip is close to the sample and the tip-voltage is also kept constant (see Fig. 3.21 (a)). The biased tip produces an inhomogeneous electric field at the apex, which has a high electric field gradient. By scanning the tip over the molecule, the field at the position of the molecule changes because of the field gradient. As the field changes, depending on the tip position, it induces different Stark shifts in the molecule. At certain tip positions, the electric field shifts the zero-phonon line of the molecule into resonance with the excitation laser frequency, Fig. 3.21 (b). At these tip positions, the molecule can be excited by the laser and a fluorescent signal can be detected. In this way, the fluorescence of the molecule can be recorded as a function of the tip position, as shown in Fig. 3.21 (c). One molecule is in focus and is pushed in and out of resonance with the laser by the electric field of the tip.

Chapter 4

Theoretical discussion and numerical simulation

A theoretical model has been developed to understand the experimental results and to underline the capability of Stark-shift microscopy. The task of the present chapter is to explain the expected Stark-shift pattern as a function of tip position and to motivate the applicability to measurements, such as the orientation determination of molecules and the investigation of coupling effects. The calculation of the Stark-shift patterns is divided in several steps. The first step is the calculation of the electric field of the tip. The the tip has been modelled once as a metal sphere and once as a truncated metal cone. With the calculated electric field distribution, the Stark-shift pattern depending on tip position is numerically simulated. Additional effects and their influence on the Stark-shift pattern will be discussed, for example, the coupling between two molecules or the coupling of a single emitter to a tunnelling two-level system of the matrix.

4.1   Electrical field of a sharp metal tip

The distribution of the static, electric field caused by the biased tip has a large influence on the Stark-shift pattern. The surface of the metallized glass-fiber tip might have a very complicated structure causing an asymmetric electric field distribution. Since experimental results show highly symmetric Stark-shift pattern, the tip has been approximated by a simplified shape such as a metal sphere or a truncated metal cone. In the case of the sphere, the calculation is simple. The electric field $\vec{E}$ can be easily calculated using the text-book example of the electric field of a metal sphere and a spherical capacitor [94]. In the case of the truncated metal cone, the calculation is more complicated and the calculation has be carried out numerically by a computer. Both calculations are shortly outlined in the following.

4.1.1   Metallized tip approximated by a metal sphere

The approximation of the tip by a metal sphere is a strong simplification. The apex of tips typically do not have such a nicely homogeneously shape as in the case of a
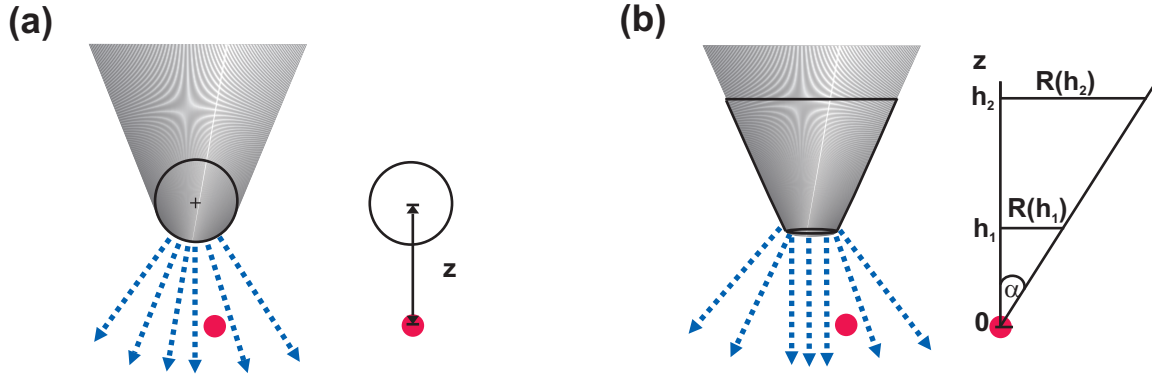
(a)

(b)

Figure 4.1: The metallized glass-fiber tip can be approximated by two different geometries: (a) as a metal sphere or (b) as a metal cone. The dashed lines indicate the electric field caused by the biased tip at the position of the molecule. The red spot is the position of the molecule. The right side of both pictures shows the simplified shape and the notation used for the theoretical simulation.

sphere. Nevertheless, this approximation still holds, if the gap-width is larger than the actual tip diameter. The electric field of a sphere-like tip is sketched in Fig. 4.1 (a). The electric field of a metal sphere is obtained by:

$$\vec{E}_{ext}(R) = \frac{Q}{4\pi\epsilon_0} \frac{\vec{e}_r}{R^2}, \tag{4.1}$$

where $R = \sqrt{x^2 + y^2 + z^2}$ is the distance between the center of the sphere and the emitter, whereby (x, y, z) marks the position of the tip and the emitter is located in the origin at $(0, 0, 0)$, Q is the charge on the tip, ϵ_0 is the dielectric constant in vacuum, and $\vec{e}_r$ is the unit vector in radial direction pointing towards the sphere. The unit vector is expressed in spherical coordinates as:

$$\vec{e}_r = \begin{pmatrix} \cos\phi\sin\theta \\ \sin\phi\sin\theta \\ \cos\theta \end{pmatrix}. \tag{4.2}$$

Transforming the unit vector $\vec{e}_r$ into Cartesian coordinates, using:

$$\begin{pmatrix} x \\ y \\ z \end{pmatrix} = \begin{pmatrix} R\cos\phi\sin\theta \\ R\sin\phi\sin\theta \\ R\cos\theta \end{pmatrix}, \tag{4.3}$$

it follows an expression for the unit vector:

$$\vec{e}_r = \frac{1}{R} \begin{pmatrix} x \\ y \\ z \end{pmatrix}. \tag{4.4}$$

The electric field can now be expressed as:

$$\vec{E}_{ext}(R) = \frac{Q}{4\pi\epsilon_0} \frac{1}{R^3} \begin{pmatrix} x \\ y \\ z \end{pmatrix}. \tag{4.5}$$

The charge of the sphere can be approximated with the help of the equation of a spherical capacitor [94]:

$$U = \frac{Q}{4\pi\epsilon_0} \frac{1}{d}, \tag{4.6}$$

where d is the distance between the electrodes, and U is the applied voltage. This leads to the expression:

$$\frac{Q}{4\pi\epsilon_0} = U\,d. \tag{4.7}$$

With the expression (4.7), the electrical field $\vec{E}$ could be expressed in known parameters such as U, d and R. However, the approximation oversimplifies the calculation of the electric field. The result yields a field strength which is far away from the observed value, while the shape of the field is well described. One reason is, that because of repulsive forces not all the charges are localized at the tip. Another reason is, that the wires possess a capacity, which can not be neglected. Both effects result in a reduction of the field strength. The expression for the electric field is described by:

$$\vec{E}_{ext}(R) = \frac{A}{R^3} \begin{pmatrix} x \\ y \\ z \end{pmatrix}. \tag{4.8}$$

The adjustable factor A takes into account the tip-voltage and the capacity of the wires. The factor A is chosen in such a way, that an adequate value for the electric field is obtained.

4.1.2 Metallized tip approximated by a truncated metal cone

The calculation of the electric field of a truncated- cone-shaped tip is carried out differently. In a first step, the potential ϕ is calculated and by taking the gradient, the electric field is obtained. In this calculation, the molecule is scanned in x, y and the tip is kept fixed at one position. The potential is defined as

$$\phi(\vec{r'}) = \frac{\delta}{4\pi\epsilon_0} \int \frac{1}{|\vec{r} - \vec{r'}|} \, dA. \tag{4.9}$$

δ is the surface charge density, ϵ_0 is the dielectric constant in vacuum, $\vec{r}$ the position of the tip, $\vec{r'}$ is the position of the molecule, A is the surface of the tip. Out of geometrical reason, the problem is handled in cylindrical coordinates: $x = r\cos\phi, y = r\sin\phi, z$. The radius R of the apex of the cone depending on the coordinate z can be expressed as $R(z) = z\tan\alpha$, with α the opening angle of the tip as shown in Fig. 4.1 (b). The

surface of the truncated cone is divided in two parts. One part is the flat bottom plate of the cone and the second part is the outer side-walls of the cone. With these assumptions the formula for the electrical potential ϕ can be expressed as:

$$\phi(\vec{r'}) = \frac{\delta}{4\pi\epsilon_0} \left(\int_{h_1}^{h_2} \int_0^{2\pi} \frac{R(z)}{|\vec{r_2} - \vec{r'}|} d\phi dz + \int_0^{R(h_1)} \int_0^{2\pi} \frac{r}{|\vec{r_1} - \vec{r'}|} d\phi d r \right). \tag{4.10}$$

The first part of the formula describes the side-surface of the cone (no r integration) and the second part describes the bottom plate (no z integration). The parameter h_1, h_2 and $R(h_1)$ are defined as shown in Fig. 4.1 (b). The distance between h_1 and h_2 defines the length of the cone, which is taken into account for the simulation. By choosing a value for h_1, the diameter of the apex of the cone $R(h_1) = h_1 \tan \alpha$ is also fixed. The distances can be written as:

$$|\vec{r_1} - \vec{r'}| = \sqrt{(R(z)\cos\phi - x')^2 + (R(z)\sin\phi - y')^2 + (z - z')^2} \tag{4.11}$$
$$|\vec{r_2} - \vec{r'}| = \sqrt{(r\cos\phi - x')^2 + (r\sin\phi - y')^2 + (h_1 - z')^2} \tag{4.12}$$

The electric field is calculated numerically by:

$$\vec{E}_{ext} = -\vec{\nabla}\phi \tag{4.13}$$

with the computer program Mathematica[1]. The field of a truncated-cone-shaped tip is sketched in Fig. 4.1 (b). The modelling of a truncated metal cone is necessary at gap-width smaller than the diameter of the tip. The electric field has to be assumed constant and homogeneous during a scan distance of the order of the tip diameter.

4.2   Stark shift depending on tip position

The numerical simulation approximates the Stark shift to the first (linear Stark shift) or the second (quadratic Stark shift) order. There are two effects caused by the surrounding matrix, which have to be taken into the account for the calculation of the electric field: (i) There is an additional internal field $\vec{E}_{int}$ due to stress and disorder in the matrix. (ii) The matrix has a different dielectric constant, which is taken into account by introducing the Lorentz factor f_L. Both effects result in an electric field $\vec{E}_{tot}$ at the position of the molecule as derived in Chapter 2. Both effects are neglected in the theoretical model, since they do not have any influence on the Stark-shift patterns. The Stark shift is therefore simplified as:

$$\Delta\nu(x, y, z) = \frac{1}{h}(-\Delta\vec{\mu})\vec{E}_{ext} - \frac{1}{2h}\vec{E}_{ext}\Delta\tilde{\alpha}\vec{E}_{ext}. \tag{4.14}$$

Hence, $\Delta\nu$ is the Stark shift, (x, y, z) is the position of the tip with a molecule at the origin, $\Delta\vec{\mu}$ is the difference of the permanent dipole moments of the ground state and

---

[1]Mathematica Version 5.0

the first excited state, $\vec{E}_{ext}$ is the external electric field as described in Eq. (4.8) or in Eq. (4.13), $\Delta\tilde{\alpha}$ is difference in the polarizability. In the following, $\Delta\vec{\mu}$ is called the linear Stark-shift coefficient and $\Delta\tilde{\alpha}$ is called the quadratic Stark-shift coefficient. For symmetry reason, free terrylene molecules do not possess a permanent dipole moment and would show only a quadratic Stark effect. Nevertheless, the molecule embedded in a crystalline matrix can exhibit a matrix-induced permanent dipole moment. In such a case, the molecule would show an additional linear Stark shift, which might even dominate over the weaker quadratic Stark shift. By calculating the Stark-shift pattern, we will see that the Stark shift has a strong influence on the pattern.

4.2.1 Stark shift with a metal sphere as a tip

The tip scans over the emitter and can be positioned in all three dimensions. The emitter itself sits at the origin $(0, 0, 0)$. The expression for the linear and the quadratic Stark shift are evaluated separately. If a molecule shows both, the linear and the quadratic Stark shift, the result is a linear combination of both formulas.

Linear Stark shift

Without loss of generality, the orientation of the permanent dipole moment difference can be expressed as:

$$\Delta\vec{\mu} = |\Delta\mu|\vec{e} = |\Delta\mu| \begin{pmatrix} \sin\phi \\ 0 \\ \cos\phi \end{pmatrix}, \tag{4.15}$$

where $|\Delta\mu|$ is the difference of the matrix-induced permanent dipole moment and $0 < \phi < \pi$ is the angle between the z-axis of the crystal and the difference of the permanent dipole moment. By setting $\phi = 0$ the dipole moment difference is parallel to the z-axis.

Since the orientation of the induced permanent dipole moment is not clear, the orientation is chosen in such a way, that it fits best the experimental results. The linear Stark shift can be expressed as a function of R and ϕ with the help of Eq. (4.8):

$$\Delta\nu(R) = -\frac{1}{h}\Delta\vec{\mu}\vec{E}_{ext} \tag{4.16}$$

$$= -\frac{A}{h}\frac{|\Delta\mu|}{R^3} \begin{pmatrix} \sin\phi \\ 0 \\ \cos\phi \end{pmatrix} \begin{pmatrix} x \\ y \\ z \end{pmatrix} \tag{4.17}$$

$$= -\frac{A}{h}\frac{|\Delta\mu|}{R^3}\frac{(x\sin\phi + z\cos\phi)}{R^3}. \tag{4.18}$$

Quadratic Stark shift

For the calculation of the quadratic Stark shift, the difference in polarizability is expressed as:

$$\Delta\tilde{\alpha} = \begin{pmatrix} \Delta\alpha_{aa} & \Delta\alpha_{ab} & \Delta\alpha_{ac} \\ \Delta\alpha_{ba} & \Delta\alpha_{bb} & \Delta\alpha_{bc} \\ \Delta\alpha_{ca} & \Delta\alpha_{cb} & \Delta\alpha_{cc} \end{pmatrix} \tag{4.19}$$

$$= \begin{pmatrix} \Delta\alpha_{aa} & 0 & 0 \\ 0 & \Delta\alpha_{bb} & 0 \\ 0 & 0 & \Delta\alpha_{cc} \end{pmatrix}, \tag{4.20}$$

where $\Delta\alpha_{mm}$ with $(m = a, b, c)$ is the difference in polarizability with respect to the main axes a,b,c of the crystal. The simplification of $\Delta\tilde{\alpha}$ is reasonable, since out of symmetry reason the largest polarizability is expected along the three main axis of the molecule. The longest axis of the molecule coincides with the c-axes of the crystal, as shown in Chap. 3. The exact values of the polarizability are not known for terrylene up to now, which makes the calculation difficult. Since the values for pentacene are known, they are used as guidelines. The difference in polarizability is normalized to the value of $\Delta\alpha_{cc} = \Delta\alpha$ which is supposed to give the largest contribution. The other values are expressed as fractions of $\Delta\alpha_{cc}$ as $\Delta\alpha_{aa} = a\Delta\alpha$ and $\Delta\alpha_{bb} = b\Delta\alpha$. The approximation of the difference in polarizability $\Delta\alpha$ might not result in an absolute value for the Stark shift, but it gives qualitatively the correct behavior. The quadratic Stark shift can be expressed with the help of Eq. (4.8) as:

$$\Delta\nu(R) = -\frac{1}{2h}\vec{E}_{ext}\Delta\tilde{\alpha}\vec{E}_{ext} \tag{4.21}$$

$$= -\frac{A^2}{2hR^6}\Delta\alpha(ax^2 + by^2 + z^2). \tag{4.22}$$

4.2.2   Stark shift with a truncated metal cone as tip

For simplicity of notation, only the equation for the linear Stark effect is derived. The permanent dipole moment difference $\Delta\vec{\mu}$ of the molecule is taken to be parallel to the z-axis:

$$\Delta\vec{\mu} = |\Delta\mu| \begin{pmatrix} 0 \\ 0 \\ 1 \end{pmatrix} \tag{4.23}$$

The electrical field is obtained from the previously calculated potential: $\vec{E} = -\vec{\nabla}\phi$, which results in:

$$\Delta\nu(x', y', z') = \frac{\delta|\Delta\mu|}{h4\pi\epsilon_0}\left(\int_{h_1}^{h_2}\int_0^{2\pi} \frac{(z-z')R(z)}{|\vec{r_1}-\vec{r'}|^3}d\phi dz + \int_0^{R(h_1)}\int_0^{2\pi} \frac{(h_1-z')r}{|\vec{r_2}-\vec{r'}|^3}d\phi dr \right) \tag{4.24}$$

with

$$|\vec{r_1} - \vec{r'}|^3 = \left((R(z)\cos\phi - x')^2 + (R(z)\sin\phi - y')^2 + (z - z')^2\right)^{\frac{3}{2}}$$
$$|\vec{r_2} - \vec{r'}|^3 = \left((r\cos\phi - x')^2 + (r\sin\phi - y')^2 + (h_1 - z')^2\right)^{\frac{3}{2}}$$

This formula can be evaluated numerically. In the experiment, the gap-width has been of the order of μm and is always larger than the tip diameter. Hence, in the following discussion of the Stark-shift pattern, the tip will be approximated as a metal sphere. However, the calculation can be easily adapted to an arbitrarily shaped tip.

4.3 Stark-shift patterns as a function of tip position

The following section discusses the Stark-shift pattern as a function of tip position. By carrying out a semi-classical calculation for a single molecule the Stark-shift patterns are numerically simulated.

4.3.1 Mathematical derivation of the model

A single molecule at low temperatures can be modelled as a two-level system. Only the ground state and the first excited state are taken into account. Any contributions of the vibrational energy levels are neglected. The Hamiltonian for a two-level system in an exciting laser field reads [95, 96]:

$$H = \frac{\hbar\nu_0}{2}(-\sigma_z) - \vec{d}_{eg}\vec{E}\cos(\nu_L t)\sigma_x \qquad (4.25)$$

with the Pauli matrices

$$\sigma_z = \begin{pmatrix} 1 & 0 \\ 0 & -1 \end{pmatrix} \text{ and } \sigma_x = \begin{pmatrix} 0 & 1 \\ 1 & 0 \end{pmatrix}, \qquad (4.26)$$

ν_0 is the resonance frequency of the molecule, $\vec{d}_{eg}$ is the transition dipole moment of the emitter, and $\vec{E}$ is the laser field, varying with frequency ν_L. Using the density matrix formalism, the time evolution of the density matrix, including the spontaneous emission in Lindblatt-form, can be expressed as follows [96]:

$$\dot{\rho} = -\frac{i}{\hbar}[H,\rho] - \frac{1}{2}\Gamma\left(Ł_+Ł_-\rho + \rho Ł_+Ł_- - 2Ł_-\rho Ł_+\right), \qquad (4.27)$$

with Γ the line width of the molecule, the density matrix ρ

$$\rho = \begin{pmatrix} \rho_{aa} & \rho_{ab} \\ \rho_{ba} & \rho_{bb} \end{pmatrix}, \qquad (4.28)$$

and the ladder operators Ł

$$\text{Ł}_- = \begin{pmatrix} 0 & 1 \\ 0 & 0 \end{pmatrix} \text{ and } \text{Ł}_+ = \begin{pmatrix} 0 & 0 \\ 1 & 0 \end{pmatrix}. \tag{4.29}$$

The rotating wave approximation is used for simplifying Eq. (4.27). As the probability of the process of emitting a photon and ,at the same time, getting into the excited state can be neglected (and vice versa), the cos-term in Eq. (4.27) can be approximated. Therefore, the interaction term of the Hamiltonian can be reduced to the first two terms of the following formula:

$$\vec{d}_{ed}\vec{E}\cos(\nu_L t) = \frac{1}{2}\hbar\nu_R(|\,b\rangle\langle a\,|\,e^{-\imath\nu_L t} + |\,a\rangle\langle b\,|\,e^{\imath\nu_L t} + |\,b\rangle\langle a\,|\,e^{\imath\nu_L t} + |\,a\rangle\langle b\,|\,e^{-\imath\nu_L t}) \tag{4.30}$$

where ν_R is the Rabi frequency, and $|\,b\rangle$ and $|\,a\rangle$ are the excited and the ground state, respectively. The Hamiltonian is reduced to:

$$H = \begin{pmatrix} -\frac{\hbar\nu_0}{2} & -\frac{\hbar\nu_R}{2}e^{\imath\nu_L t} \\ -\frac{\hbar\nu_R}{2}e^{-\imath\nu_L t} & \frac{\hbar\nu_0}{2} \end{pmatrix}, \tag{4.31}$$

with the abbreviation for the Rabi frequency

$$\nu_R = \frac{\vec{d}_{eg}\vec{E}}{\hbar}. \tag{4.32}$$

As part of the rotating wave approximation, a transformation into the rotating frame is made:

$$\tilde{\rho}_{ab} = \rho_{ab}e^{\imath\nu_L t} \tag{4.33}$$

$$\tilde{\rho}_{ba} = \rho_{ba}e^{-\imath\nu_L t} \tag{4.34}$$

$$\tilde{\rho}_{aa} = \rho_{aa} \tag{4.35}$$

$$\tilde{\rho}_{bb} = \rho_{bb} \tag{4.36}$$

As a next step the time evolution for the density matrix elements can be calculated:

$$\dot{\tilde{\rho}}_{aa} = -\frac{\imath\nu_R}{2}(\tilde{\rho}_{ab} - \tilde{\rho}_{ba}) + \Gamma\tilde{\rho}_{bb} \tag{4.37}$$

$$\dot{\tilde{\rho}}_{bb} = \frac{\imath\nu_R}{2}(\tilde{\rho}_{ab} - \tilde{\rho}_{ba}) - \Gamma\tilde{\rho}_{bb} \tag{4.38}$$

$$\dot{\tilde{\rho}}_{ab} = -\imath(\nu_L - \nu_0)\tilde{\rho}_{ab} - \frac{\imath\nu_R}{2}(\tilde{\rho}_{aa} - \tilde{\rho}_{bb}) - \frac{1}{2}\Gamma\tilde{\rho}_{ab} \tag{4.39}$$

$$\dot{\tilde{\rho}}_{ba} = \imath(\nu_L - \nu_0)\tilde{\rho}_{ba} + \frac{\imath\nu_R}{2}(\tilde{\rho}_{aa} - \tilde{\rho}_{bb}) - \frac{1}{2}\Gamma\tilde{\rho}_{ba} \tag{4.40}$$

In the following, only the steady-state is considered, since the time evolution is not resolved in the experiment. Therefore, the left hand side of Eq. (4.37) to (4.40) of the time-evolution of the density matrix components are set to zero. The four equations

can be reduced to two equations, depending only on the two components $\tilde{\rho}_{aa}$ and $\tilde{\rho}_{bb}$:

$$0 = \dot{\tilde{\rho}}_{aa} = -\frac{\nu_R^2 \Gamma}{4(\nu_L - \nu_0)^2 + \Gamma^2} \tilde{\rho}_{aa} + \left(\frac{\nu_R^2}{4(\nu_L - \nu_0)^2 + \Gamma^2} + 1 \right) \Gamma \tilde{\rho}_{bb} \quad (4.41)$$

$$0 = \dot{\tilde{\rho}}_{bb} = \frac{\nu_R^2 \Gamma}{4(\nu_L - \nu_0)^2 + \Gamma^2} \tilde{\rho}_{aa} - \left(\frac{\nu_R^2}{4(\nu_L - \nu_0)^2 + \Gamma^2} + 1 \right) \Gamma \tilde{\rho}_{bb} \quad (4.42)$$

The pre-factors for the occupation probabilities $\tilde{\rho}_{aa}$ and $\tilde{\rho}_{bb}$ on the right side of the Eq. (4.41) and (4.42) are the transition rates for going from the ground state to the excited state $\gamma_{a \to b}$ and for going from the excited to the ground state $\gamma_{b \to a}$, respectively:

$$\gamma_{a \to b} = -\frac{\nu_R^2 \Gamma}{4(\nu_L - \nu_0)^2 + \Gamma^2} \quad (4.43)$$

$$\gamma_{b \to a} = \left(\frac{\nu_R^2}{4(\nu_L - \nu_0)^2 + \Gamma^2} + 1 \right) \Gamma \quad (4.44)$$

Again, the steady-state is considered and the time-evolution in Eq. (4.41) and (4.42) is set to zero. Additionally, the addition of both probabilities has to equal unity, $\tilde{\rho}_{aa} + \tilde{\rho}_{bb} = 1$. From that, an expression for the occupation probability of the excited state is obtained:

$$\tilde{\rho}_{bb} = \frac{\nu_R^2}{2\nu_R^2 + 4(\nu_L - \nu_0)^2 + \Gamma^2}. \quad (4.45)$$

The fluorescence of a single molecule can be calculated by multiplying the radiative transition rate $\gamma_{b \to a}$ with the occupation probability of the excited state $\tilde{\rho}_{bb}$. This leads to the following result for the fluorescence I_{fluo}, assuming quantum yield $\phi = 1$:

$$I_{fluo} = \left(\frac{\nu_R^2 \Gamma}{4(\nu_L - \nu_0)^2 + \Gamma^2} + \Gamma \right) \frac{\nu_R^2}{2\nu_R^2 + 4(\nu_L - \nu_0)^2 + \Gamma^2}. \quad (4.46)$$

This expression includes all contributions to the fluorescence, such as the stimulated and the spontaneous emission. Since the stimulated emission is cut off with a filter, only the spontaneous emission has to be taken into account, which results in the fluorescence I of a single emitter:

$$I = \frac{\Gamma \nu_R^2}{(2\nu_R^2 + 4(\nu_L - \nu_0)^2 + \Gamma^2)}. \quad (4.47)$$

The resonance frequency ν_0 of the single molecule is now modulated by the Stark effect due to the electric field of the tip. Taking into account the Stark shift $\Delta\nu$, the Stark-shift pattern as a function of tip position can be expressed as follows:

$$I_{fluo}(x, y, z) = \frac{\Gamma \nu_R^2}{(2\nu_R^2 + 4(\Delta\tilde{\nu} - \Delta\nu)^2 + \Gamma^2)}, \quad (4.48)$$

$\Delta\tilde{\nu} = \nu_L - \nu_0$ is the detuning between the laser frequency ν_L and the zero-field resonance ν_0, and $\Delta\nu(x, y, z)$ is the Stark shift as calculated in section 4.2.
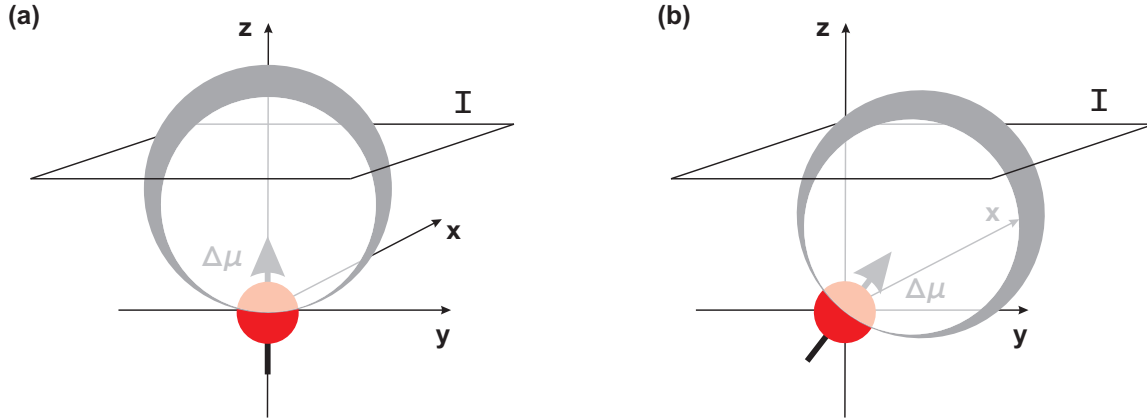
Figure 4.2: 3-dimensional sketch of the Stark-shift balloon for a single molecule with a dominant linear Stark-shift, I is the image plane. (a) The permanent dipole moment difference is oriented along the c-axis. (b) The permanent dipole moment difference is tilted.

4.3.2 Numerical simulation of the Stark-shift patterns

The section presents numerical simulation of the Stark-shift pattern as a function of tip position. The calculations are carried out by the computer program Mathematica[2]. The fluorescence $I(x, y, z)$ in Eq. (4.48) resembles a 3-dimensional Stark-shift balloon, as sketched in Fig. 4.2. The size of Stark-shift balloon depends on the parameter settings, such as tip voltage and detuning, as we will see later. By scanning the tip at a constant height, a section of the Stark-shift balloon is measured as indicated by the image plane I in Fig. 4.2. The balloon has a certain wall thickness, which changes depending on the gap-width z as shown in Fig. 4.2. If $\Delta\vec{\mu}$ is oriented along the z-axis (Fig. 4.2 (a)), the imaged Stark-shift pattern is a circular feature, what we call the Stark-shift ring. If $\Delta\vec{\mu}$ is tilted (Fig. 4.2 (b)), the Stark-shift pattern becomes an ellipse with varying ring width. Since it is kind of difficult to illustrate the properties of this 3-dimensional Stark-shift balloon, only vertical sections at fixed gap-width z or horizontal sections at $y = 0$ will be discussed in the following. The Stark-shift pattern can be described by two parameter: the ring width W of the Stark-shift balloon and the pattern width (or size) W.

Vertical sections of the Stark-shift pattern of a single molecule

The vertical sections of the Stark-shift balloon correspond to the experimental images taken by one spatial tip scan. In Fig. 4.3 (x,y)-sections of the fluorescence of a single molecule as a function of tip position at different gap-width z are shown. The white spot at the origin of the image symbolizes the position of the molecule. The detuning $\Delta\tilde{\nu}$ is kept fixed at 600 MHz. The imaged molecule has a line width of $\Gamma = 50$ MHz and the Rabi frequency ν_R is set to a reasonable value of 1MHz. From left to right, the gap-width is reduced from 1.6 μm to 100 nm, as indicated by the sketches in
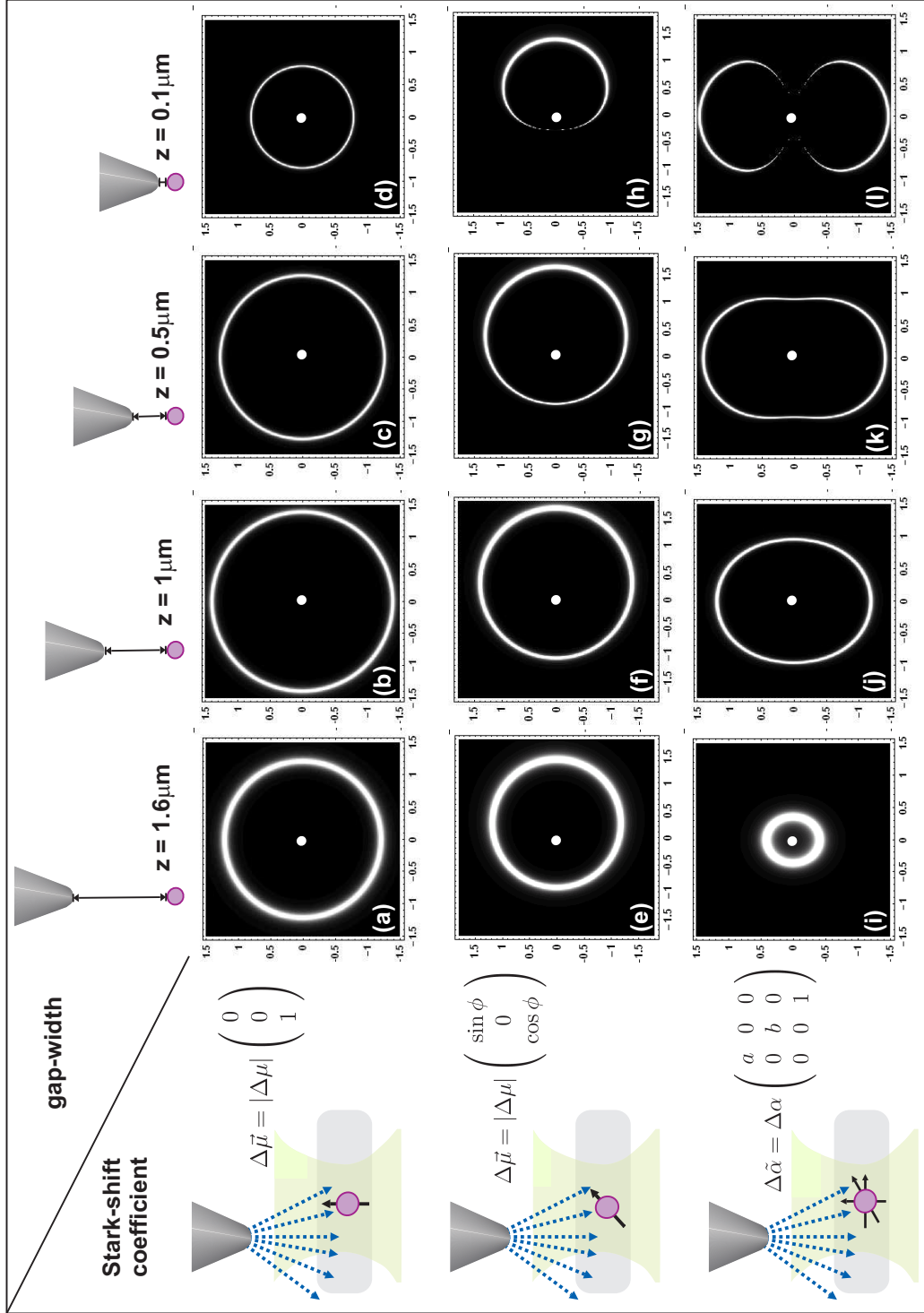
---

[2]Mathematica Version 5.0

Figure 4.3: (x,y)-sections of the Stark-shift pattern as a function of tip position and gap-width. The white spot in the center symbolizes the molecule's position. The scan range of the tip is $3 \times 3 \ \mu m^2$. The gap-width is reduced from left to right as indicated in the first line. The detuning is kept fixed a 600 MHz. The Stark-shift coefficients differ from row to row. (a)-(d) Case A: Stark-shift pattern for a molecule with a pure permanent dipole moment $\Delta\vec{\mu}$, which is orientated along the z-axis. (e)-(h) Case B: Stark-shift pattern for a molecule with a permanent dipole moment $\Delta\vec{\mu}$, which has an angle of $\phi = \pi/10$ to the z-axis. (i)-(l) Case C: Stark-shift pattern for a molecule a quadratic Stark-shift component of: $\Delta\alpha_{aa} = -0.1 \times \Delta\alpha$ and $\Delta\alpha_{bb} = 0.6 \times \Delta\alpha$.

the first row in Fig. 4.3. The Stark-shift coefficients differ from row to row, going from a linear Stark shift with different permanent dipole difference orientations to a quadratic Stark shift.

Case A: Linear Stark shift with $\Delta\vec{\mu} \parallel z$ In the first row, Fig. 4.3 (a)-(d), the molecule is assumed to possess a purely linear Stark shift. The molecule has a permanent dipole difference $\Delta\vec{\mu}$ orientated in the direction of the z-axis ($\phi = 0$ in Eq. (4.18)). The Stark-shift pattern for such a molecule is a symmetric ring with the molecule at its center. This Stark-shift pattern is called Stark-shift ring in the following. By approaching the tip towards the molecule (following the first row from left to right), two effects stand out. The diameter of the Stark-shift ring first increases. At a certain gap-width (here $z < 1\mu$m), the diameter starts to decrease again. The critical gap-width, at which the diameter starts to decrease, depends on the settings of the detuning $\Delta\tilde{\nu}$ and the tip-voltage. Concomitantly to the diameter change, the ring width decreases while the tip is approached. As we will see in the following, these effects are common for all Stark-shift pattern and will be explained in section 4.3.2.

Case B: Linear Stark shift with tilted $\Delta\vec{\mu}$ The second row, Fig. 4.3 (e)-(h), shows the Stark-shift pattern of a molecule, which exhibits a linear Stark-shift effect. But in this case, the permanent dipole moment difference $\Delta\vec{\mu}$ has an angle to the z-axis of $\phi = \pi/10$. The Stark-shift pattern differs considerably from the one in case A with $\Delta\vec{\mu} \parallel z$. If the tip is far away from the molecule, Fig. 4.3 (e), the Stark-shift pattern appears similar to the ring-like Stark-shift pattern of case A, but with a slight variation in line width and an offset between the center of the Stark-shift pattern and the molecule position. By reducing the gap-width (going from (e) to (h)), the circular structure becomes more and more elliptic. The asymmetry in the pattern width depends on the orientation of the dipole moment difference $\Delta\vec{\mu}$ and becomes more and more apparent at small gap-widths. On one side of the molecule, the orientation of $\Delta\vec{\mu}$ is more favorable to interact with the electric field, than on the other side of the molecule. The orientation dependence influences the Stark shift of the molecule. It becomes apparent, that with Stark-shift microscopy, the orientation of $\Delta\vec{\mu}$ can be determined. As in case A with $\Delta\vec{\mu} \parallel z$, the Stark-shift pattern depends strongly on the gap-width z, and shows the same effects: the Stark-shift pattern shows a increase and decrease in the dimension and a concomitantly decrease of the width. The explanation follows in section 4.3.2.

Case C: Quadratic Stark shift   In the last row, Fig. 4.3 (i)-(l), the Stark-shift patterns of a molecule with a dominant quadratic Stark-shift coefficient are shown. The polarizability has been set to $\Delta\alpha_{aa} = -0.1 \times \Delta\alpha$ and $\Delta\alpha_{bb} = 0.6 \times \Delta\alpha$. Already at large gap-widths (Fig. 4.3 (i)), these Stark-shift patterns have an elliptical shape. Compared to the tilted $\Delta\vec{\mu}$, there is no asymmetry in the width of the ring and the pattern is symmetric to the origin. The effect of a decrease in width and also the enlargement of the circular feature seems to depend stronger on the gap-width than
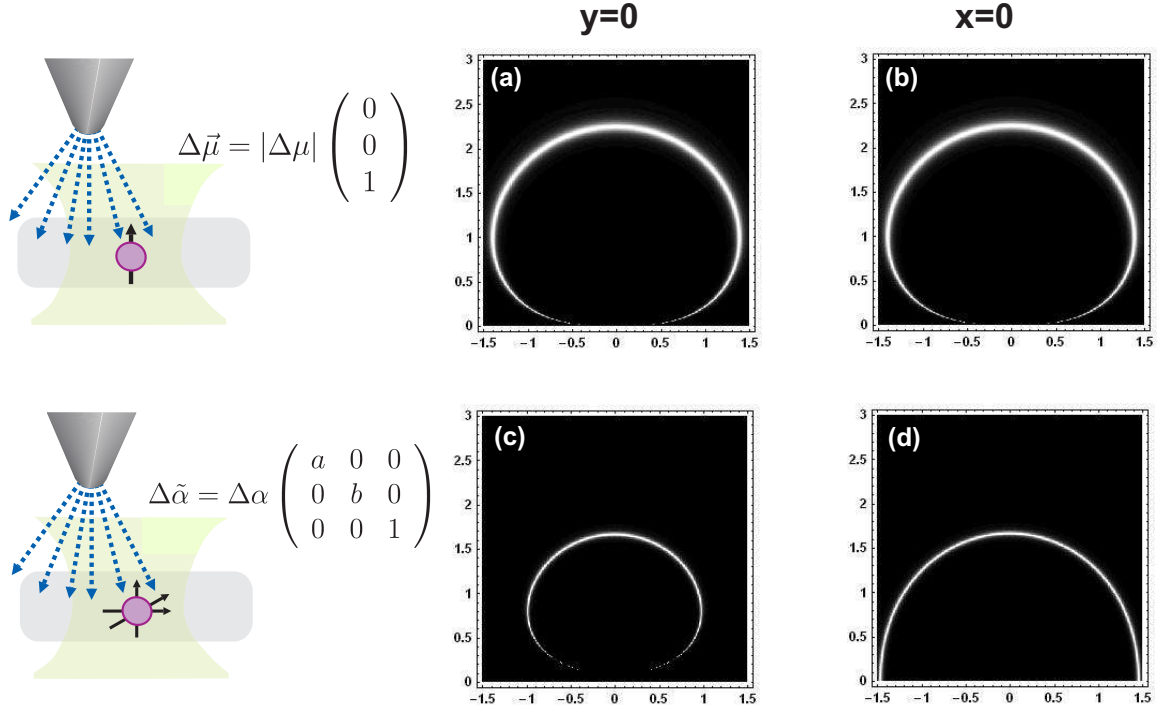
Figure 4.4: Sections along the z-axis of Stark-shift patterns from numerical simulations. (a) and (b) show a (x,z)- and a (y,z)-section of Stark-shift patterns of a molecule with only a linear Stark-shift component. The permanent dipole moment difference $\Delta\vec{\mu}$ is orientated along the z-axis. (c) and (d) show a (x,z)- and a (y,z)-section of Stark-shift patterns of a molecule with only a quadratic Stark-shift component: $\Delta\alpha_{aa} = -0.1 \times \Delta\alpha$ and $\Delta\alpha_{bb} = 0.6 \times \Delta\alpha$.

in case A or B. The Stark-shift patterns show a really interesting behavior, if the gap-width is further reduced. The asymmetry due to the difference of the polarizability becomes apparent. Since the $\Delta\alpha_{aa}$-component of the polarizability is negative, the Stark-shift goes to a different direction than the Stark-shift of the $\Delta\alpha_{bb}$-component. At a 100 nm gap-width (Fig. 4.3 (l)), the fluorescent feature is divided into an upper and a lower lobe, symmetric around the position of the molecule.

Horizontal sections of the Stark-shift pattern of a single molecule

In contrast to the vertical sections, which correspond directly to an experimental measurement, the horizontal sections cannot be measured in a single tip scan. On the other hand, theses horizontal sections give a better idea of the geometry of the 3-dimensional Stark-shift balloon. In Fig. 4.4, (x,z)-sections at $y = 0$ and (y,z)-sections at $x = 0$ are shown, respectively. In this figure, the different behavior for the linear and the quadratic Stark shift is nicely visible. The figures reveal the gap-width dependence of the Stark-shift patterns: an increase of the diameter, followed by a diameter decrease at a certain gap-width. The parameter for the detuning, the line width of the molecule and the Rabi-frequency are kept fixed: $\Delta\tilde{\nu} = 600\text{MHz}$,
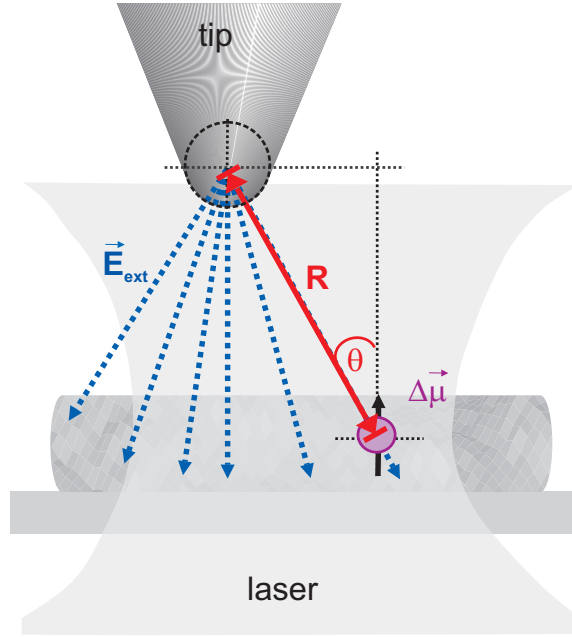
Figure 4.5: Geometry of the experimental settings: angle θ and distance r between $\Delta\vec{\mu}$ and $\vec{E}$ define the behavior of the diameter and the width of the Stark-shift pattern. For details, see text.

$\Gamma = 50$MHz, and $\nu_R = 1$MHz. The upper row, Fig. 4.4 (a) and (b), visualizes the tip-approach dependence of the Stark-shift ring for an emitter possessing a purely linear Stark shift with $\Delta\vec{\mu} \parallel z$ as in Case A. The Stark-shift balloon is symmetric for $\Delta\vec{\mu} \parallel z$, therefore Fig. 4.4 (a) and (b) show the same dependency on the gap-width z. The lower row, Fig. 4.4 (c) and (d), show the tip-approach dependence of the Stark-shift pattern for an emitter exhibiting a quadratic Stark shift. The values for $\Delta\alpha$ are chosen as: $\Delta\alpha_{aa} = -0.1 \times \Delta\alpha$ and $\Delta\alpha_{bb} = 0.6 \times \Delta\alpha$. The (x,z)-section resembles the behavior of the linear Stark-shift. The (y,z)-section shows only an increase in diameter, which is not followed by a decrease as in the linear Stark-shift case. This behavior results into the two-lobe pattern as shown in Fig. 4.3 (l).

Behavior of the Stark-shift pattern depending on the electric field

As a general behavior, independent of the Stark-shift coefficient, the Stark-shift pattern width decreases and its size concomitantly increases (followed by a decrease), as the tip approaches the molecule.

The change of the pattern dimension can be explained by two processes. It is obvious that the coupling of the electric field to the dipole depends on the distance R and on the angle θ between the permanent dipole moment difference $\Delta\vec{\mu}$ and the field lines $\vec{E}_{ext}$, as sketched in Fig. 4.5. By reducing the gap-width z, the field strength at the position of the molecule increases which results in an enlargement of the Stark-shift ring. At a certain critical gap-width the angle θ between $\vec{E}$ and $\Delta\vec{\mu}$ becomes
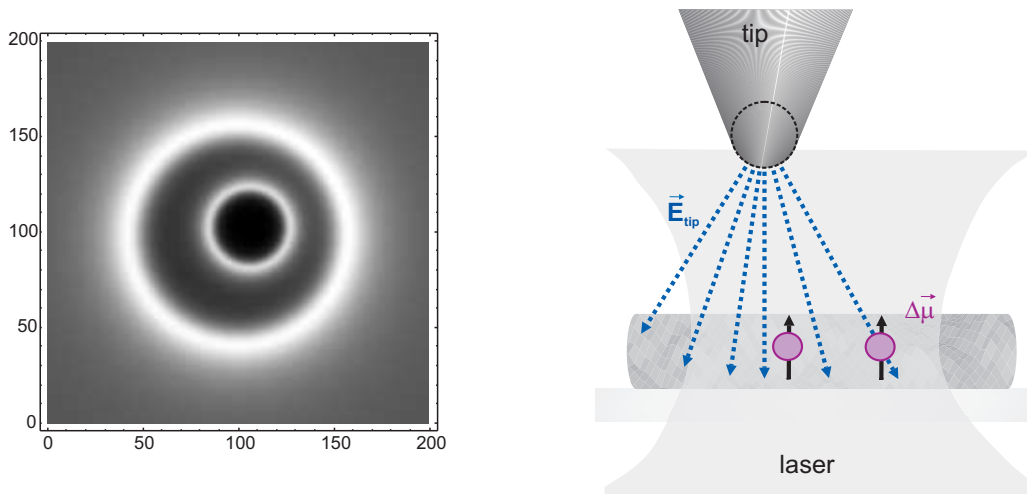
Figure 4.6: Left side shows a numerically simulated Stark-shift pattern of two single molecules, which are separated spectrally by $\Delta\nu_s = 10$ GHz and spatially $r = 0.36\,\mu$m. Right side shows the experimental settings. Both permanent dipole moment difference are parallel to the z-axis. Even though, both molecules differ spectrally, they can be resolved in a single spatial tip scan.

unfavorable. Only the stronger field in closer proximity to the tip apex induces a sufficiently strong Stark shift to push the molecule into resonance. This results in a decrease of the Stark-shift ring diameter.

The measured and simulated decrease in the width of the Stark-shift ring can be explained by the increase of the field gradient during the tip approach. If the gap-width z is large, the gradient of the field is very small. The tip has to be scanned by a large distance to change the electric field at the position of the molecule. The induced Stark shift depending on tip position is varying very slowly, which results in Stark-shift ring with a very broad thickness. By reducing the gap-width, the gradient of the electric field increases. This increase results in a faster tuning of the Stark shift and therefore in a thinner Stark-shift ring.

Stark-shift imaging of several molecules

We consider now the case, where several molecules with varying resonance frequencies are located in the focal volume of the excitation laser. Single molecules with differing resonances could be only resolved in a sequence of sample scans with adjusted excitation frequency. However, using Stark-shift microscopy, the position of these molecules can be determined in one spatial tip scan, as shown in Fig. 4.6. On the left side of Fig. 4.6, the simulated Stark-shift pattern depending on the tip position is shown. The experimental settings are sketched on the right side. Two molecules are located in the focal area. The two molecules have a permanent dipole difference along the z-axis. For simplicity, they both exhibit a linear Stark shift, but differently strong. Their resonances are separated spectrally by 10 GHz. The molecules are

spatially separated by $r = \sqrt{(x_0 - x_1)^2 + (y_0 - y_1)^2} = 0.36\,\mu$m. Both molecules are still inside the focussed laser spot, which has an diameter of 400 nm. The positions of the two molecules can be clearly assigned to the origins of the Stark shift rings. In this way, the distance r between the molecules in the (x,y)-plane is easily obtained. Therefore, both molecules are resolved in one tip scan by using the spatial and spectral information. As it will be shown experimentally, it is not necessary for such a measurement to move the tip into the near-field. The only condition is that the field gradient of the tip is large enough to push the molecules into resonance with the laser at different tip positions. Already far-field tip scans with a gap-width in the μm-range result in a resolution of the inter-molecule distance in the nm-range.

4.4 Coupling effects

Coupling between several emitters or between emitters and a TLS of the matrix have an interesting influence on the above discussed features. Such interactions between single quantum systems are under investigation for a long time [15, 60], since they are difficult to detect. The Stark-shift imaging technique offers the possibility to investigate such interaction effects. In the following sections, the emphasize lies on the dipole-dipole coupling between two single emitters and the coupling of a single emitter and a two-level system (TLS) of the matrix.

4.4.1 Coupling between two single emitters

In the first section, the coupling between two molecules will be discussed. The two emitters are treated in the same way as in the case of a single emitter in the section 4.3. The theoretical model is expanded by introducing a dipole-dipole coupling between the two dipoles. Based on this model, the Stark-shift pattern are numerically simulated.

Mathematical derivation of the model

Following the same procedure as in Chapter 4.3, we extend the model to a system of two coupled emitters. The notation of the states for the coupled system is:

$$\left.\begin{array}{lll} \text{molecule 1} & |\,a_1\rangle & |\,b_1\rangle \\ \text{molecule 2} & |\,a_2\rangle & |\,b_2\rangle \end{array}\right\} \quad \text{coupled system: } |\,a\,a\rangle \quad |\,b\,b\rangle \quad |\,a\,b\rangle \quad |\,b\,a\rangle$$

The first letter describes the state of molecule 1 and the second letter molecule 2, whereas letter 'a' indicates the ground state and letter 'b' the first excited state as presented in Chapter 2.3. The density-matrix formalism is used to describe the system and has been derived in Eq. (2.27). The time evolution of the density matrix, including the spontaneous emission due to the interaction with the environment, for

both molecules in Lindblatt-form can be expressed as [96]:

$$\dot{\rho} = -\frac{1}{\hbar}[H,\rho] - \frac{1}{2}\Gamma_1 \left(Ł_+^1 Ł_-^1 \rho + \rho Ł_+^1 Ł_-^1 - 2Ł_-^1 \rho Ł_+^1 \right) - \frac{1}{2}\Gamma_2 \left(Ł_+^2 Ł_-^2 \rho + \rho Ł_+^2 Ł_-^2 - 2Ł_-^2 \rho Ł_+^2 \right) \tag{4.49}$$

The density matrix ρ and the matrices for $Ł_+$ and $Ł_-$ in the bases of the coupled system:

$$\rho = \begin{pmatrix} \rho_{aaaa} & \rho_{aaba} & \rho_{aaab} & \rho_{aabb} \\ \rho_{baaa} & \rho_{baba} & \rho_{baab} & \rho_{babb} \\ \rho_{abaa} & \rho_{abba} & \rho_{abab} & \rho_{abbb} \\ \rho_{bbaa} & \rho_{bbba} & \rho_{bbab} & \rho_{bbbb} \end{pmatrix}, \quad Ł_+^1 = \begin{pmatrix} 0 & 0 & 0 & 0 \\ 1 & 0 & 0 & 0 \\ 0 & 0 & 0 & 0 \\ 0 & 0 & 1 & 0 \end{pmatrix},$$

$$Ł_-^1 = \begin{pmatrix} 0 & 1 & 0 & 0 \\ 0 & 0 & 0 & 0 \\ 0 & 0 & 0 & 1 \\ 0 & 0 & 0 & 0 \end{pmatrix}, \quad Ł_+^2 = \begin{pmatrix} 0 & 0 & 0 & 0 \\ 1 & 0 & 0 & 0 \\ 0 & 0 & 0 & 0 \\ 0 & 0 & 1 & 0 \end{pmatrix}, \quad Ł_-^2 = \begin{pmatrix} 0 & 1 & 0 & 0 \\ 0 & 0 & 0 & 0 \\ 0 & 0 & 0 & 1 \\ 0 & 0 & 0 & 0 \end{pmatrix}.$$

The coupling J between the molecules, which is at first assumed to be constant, is introduced by:

$$J = j \left(| \, ab \rangle \langle ba \, | + | \, ba \rangle \langle ab \, | \right) \tag{4.50}$$

$$\tag{4.51}$$

$$= \begin{pmatrix} 0 & 0 & 0 & 0 \\ 0 & 0 & j & 0 \\ 0 & j & 0 & 0 \\ 0 & 0 & 0 & 0 \end{pmatrix} \tag{4.52}$$

Applying the rotating wave approximation and introducing the coupling to the Hamiltonian, it follows for the whole system:

$$H = \begin{pmatrix} -\frac{\hbar(\nu_1+\nu_2)}{2} & \nu_{R1}\hbar e^{i\nu_L t} & \nu_{R2}\hbar e^{i\nu_L t} & 0 \\ \nu_{R2}\hbar e^{-i\nu_L t} & \frac{\hbar(\nu_2-\nu_1)}{2} & j & \nu_{R1}\hbar e^{i\nu_L t} \\ \nu_{R1}\hbar e^{-i\nu_L t} & j & \frac{\hbar(\nu_1-\nu_2)}{2} & \nu_{R2}\hbar e^{i\nu_L t} \\ 0 & \nu_{R1}\hbar e^{-i\nu_L t} & \nu_{R2}\hbar e^{-i\nu_L t} & \frac{\hbar(\nu_2+\nu_1)}{2} \end{pmatrix} \tag{4.53}$$

where ν_1, ν_2 are the resonance frequencies of the two molecules, ν_L is the laser frequency, ν_{R1}, ν_{R2} are the Rabi frequencies and j is the dipole-dipole coupling constant. Starting from that, the same procedure is done as for the single emitter. Using Mathematica[3] the values for the density matrix ρ are numerically computed. In order to get the fluorescence of the TLS, the integration over all frequencies must be done, since the detector counts all incoming photons. The other important point is, that everything is analyzed in steady state, therefore $t \to \infty$.

---

[3]Mathematica Version 5.0

The power spectrum is calculated as follows [96]:

$$S(\vec{r},\nu') = \frac{1}{2\pi} \int_{-\infty}^{\infty} d\tau \, \Re\{\langle E^-(\vec{r},t)E^+(\vec{r},t+\tau)\rangle e^{i\nu'\tau}\},\tag{4.54}$$

where $E^-(\vec{r},t)$ and $E^+(\vec{r},t)$ are the electric field operators for the negative frequency part and the positive frequency part, respectively. Integrating over all photon frequencies yields the final result for the fluorescence intensity I:

$$
I = \int_{-\infty}^{\infty} d\nu_0\, S(\vec{r},\nu') \;=\; \frac{1}{4\pi}\int_{-\infty}^{\infty} d\tau\, \left(\langle E^-(\vec{r},t)E^+(\vec{r},t+\tau)\rangle \underbrace{\int_{-\infty}^{\infty} e^{i\nu\tau} d\nu'}_{\delta(\tau)2\pi} \right.
\tag{4.55}
$$

$$
\left. + \langle E^-(\vec{r},t)E^+(\vec{r},t+\tau)\rangle^* \underbrace{\int_{-\infty}^{\infty} e^{-i\nu\tau} d\nu'}_{\delta(\tau)2\pi} \right)
\tag{4.56}
$$

$$
= \frac{1}{2}\int_{-\infty}^{\infty} d\tau\, \left(\langle E^-(\vec{r},t)E^+(\vec{r},t+\tau)\rangle \delta(\tau) \right.
\tag{4.57}
$$

$$
\left. + \langle E^-(\vec{r},t)E^+(\vec{r},t+\tau)\rangle^* \delta(\tau) \right)
\tag{4.58}
$$

$$\tag{4.59}$$

$$
= \Re\{\langle E^-(\vec{r},t)E^+(\vec{r},t)\rangle\}
\tag{4.60}
$$

$$\tag{4.61}$$

$$
= \Re\{I_0(\vec{r})\langle L_+(t)L_-(t)\rangle\}
\tag{4.62}
$$

$$\tag{4.63}$$

$$
= \Re\{I_0(\vec{r})\mathrm{tr}[L_+L_-\rho]\}
\tag{4.64}
$$

By taking the numerically calculated values for the density matrix ρ, the fluorescence for a molecule system can be calculated. Integration over the frequency range and by plotting this result over the incoming laser frequency, an image of the Stark-shift pattern is generated.

Dipole-dipole coupling constant j

Until now, it has been assumed that the coupling constant j is not influenced by the Stark shift. This aspect has to be proven. On the other side, it would be really interesting to introduce a tool, usable to control the coupling between quantum systems. Using the Stark-shift microscope as a tool, to interact with single emitters and tune their coupling strength would open a door for fascinating possibilities. The coupling between two single molecules is accomplished by dipole-dipole coupling [49]. In the following, an estimation is presented, where the influence of the tip-induced Stark

effect is shown.

The formula for the static dipole-dipole coupling j accounts to [49]:

$$j = \frac{3\sqrt{\Gamma_1\Gamma_2}}{4(k_0 r_{12})^3} \left[(\hat{\mu}_1\hat{\mu}_2) - 3(\hat{\mu}_1\hat{r}_{12})(\hat{\mu}_2\hat{r}_{12})\right]. \quad (4.65)$$

Here, Γ_1, Γ_2 are the line width of molecule 1 and molecule 2, $k_0 = \frac{\nu_1-\nu_2}{2c}$ is the average wave number, $\hat{r}_{12}$ is the distance between the molecules, $\hat{\mu}_{1/2}$ are the dipole moments. Assuming, that the dipole moments are parallel to each other and perpendicular to the connecting vector r_{12}:

$$\hat{\mu}_1\hat{r}_{12} = \hat{\mu}_2\hat{r}_{12} = 1 \quad (4.66)$$

and

$$\hat{\mu}_1\hat{\mu}_2 = 0. \quad (4.67)$$

The resonance of a single molecule can be expressed by:

$$\Gamma_i = \frac{k_i^3 \mu_i^2}{6\pi\epsilon_0\hbar}, \quad (4.68)$$

where $i = 1, 2$ and $k_i = \frac{\nu_i}{c}$ with c as the speed of light. The dipole-dipole coupling can now be expressed as:

$$j = \frac{3\sqrt{\Gamma_1\Gamma_2}}{4(k_0 r_{12})^3} \quad (4.69)$$

$$= \frac{(\nu_1\nu_2)^{3/2}\mu_1\mu_2}{((\nu_1 + \nu_2)r_{12})^3\pi\epsilon_0\hbar} \quad (4.70)$$

The tip-position depending Stark shift is introduced into the formula by adding to the resonance frequencies ν_i the Stark shift $\Delta\nu$ calculated section 4.2. Introducing the Stark shift yields:

$$j = \frac{((\nu_1 + \Delta\nu_1)(\nu_2 + \Delta\nu_2))^{3/2}}{((\nu_1 + \nu_2 + \Delta\nu_1 + \Delta\nu_2)r_{12})^3\pi\epsilon_0\hbar} \quad (4.71)$$

Without further calculation, it is already obvious that the influence of the tip-induced component of the dipole-dipole coupling is negligible. The tip-induced Stark-shift $\Delta\nu_i$ lies in the frequency range of MHz or GHz. Compared to the value of the resonance frequency ν_i of a single molecule, which lies in the THz-range, the Stark-shift can be neglected. Therefore, during the tip scan, the dipole-dipole coupling constant can be assumed to be constant.

Numerical simulated Stark-shift pattern of coupled molecules

In Fig. 4.7 (a), two fluorescent, uncoupled ($j = 0$) molecules are resolved in one tip scan with a scan range of 200×200 nm. The two molecules are separated by
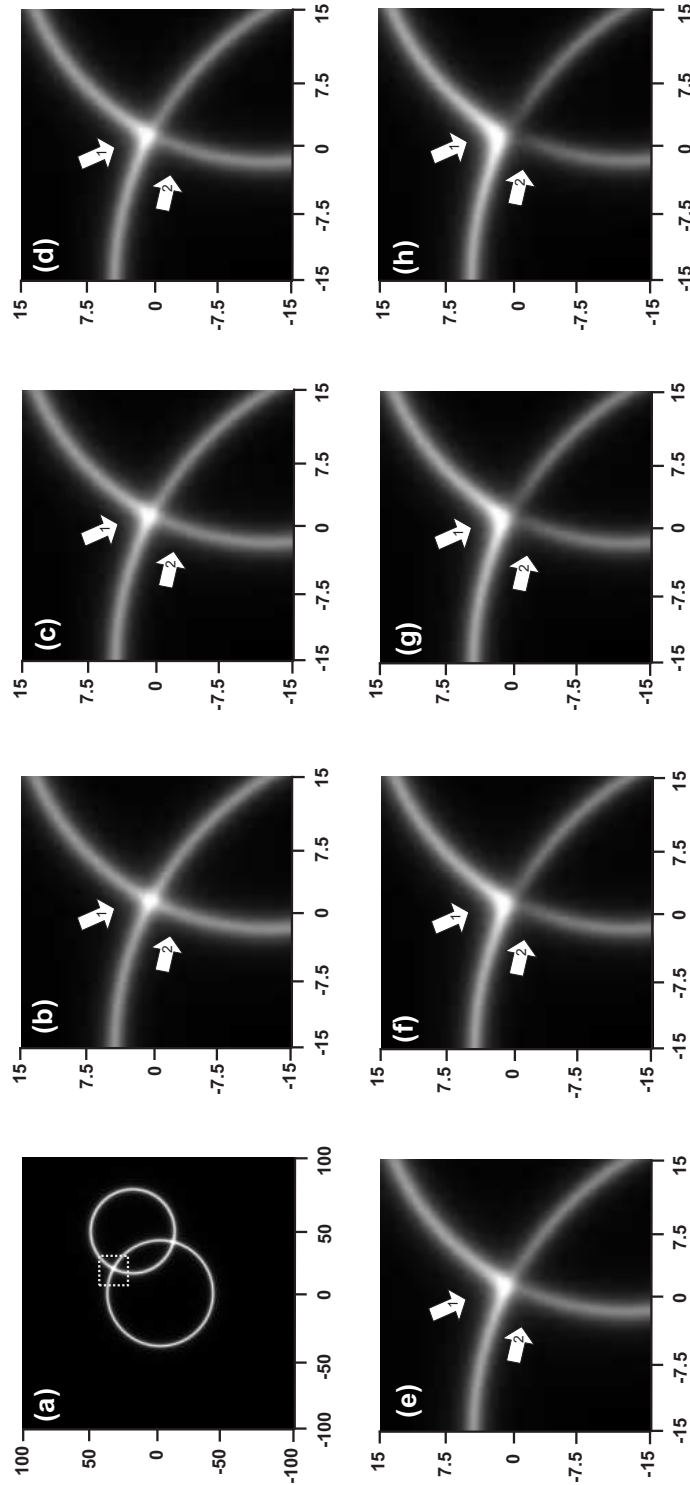
Figure 4.7: Numerically simulated Stark-shift pattern for two molecules separated by 49 m and resolved in a single tip scan. The parameter are chosen in such a way, that the Stark-shift rings are crossing each other. Scan-range of the tip is 200×200 nm. (a) Two uncoupled molecules ($j = 0$) with crossing Stark-shift rings. (b) Zoom-in on of the crossing point of the Stark-shift rings. The molecules are still uncoupled, $j = 0$. The new scan range of the tip is 33×33 nm. (c)-(h) the interaction j increases in units of the Rabi frequency $\nu_R = 1$ MHz, which defines the laser-molecule interaction. (c) $j = 2\nu_R$. (d) $j = 6\nu_R$. (e) $j = 10\nu_R$. (f) $j = 12\nu_R$. (g) $j = 16\nu_R$. (h) $j = 20\nu_R$.

49 nm. The parameter of the detuning and of the applied voltage are chosen in such a way, that the Stark-shift rings cross each other. The gap-width z is 70 nm. The Rabi-frequency ν_R is 1 MHz and the line width Γ of the molecule is chosen 40 MHz. The following sequence of simulated images show a zoom-in of the crossing point of the two Stark-shift rings, indicated as a dashed square in Fig. 4.7 (a). The new scan range of the tip is 33×33 nm. The coupling constant is increased from Fig. 4.7 (c)-(h). In Fig. 4.7 (b), the uncoupled case ($j = 0$) is shown. It is visible, indicated by the arrows (1) and (2), that the resonances of the two molecules cross each other without any effect. By increasing the coupling constant j, the crossing point of the two Stark-shift rings begins to change. Arrow (1) points towards an area, which becomes more smeared out in the intensity. Arrow (2) points towards an area, where an avoided crossing becomes visible. The higher the coupling constant, the better the avoided crossing becomes apparent, as it is shown in Fig. 4.7 (h).

By careful analysis of such an Stark-shift pattern, coupled molecules can be detected in a single spatial tip scan. The parameters , such as the tip voltage and the detuning $\Delta\tilde{\nu}$, have to be chosen very carefully to obtain a Stark-shift pattern of crossing rings. Detecting such a pattern might be already quite challenging. Furthermore, one has to keep in mind, that the simulation assumes an infinite sharp tip. The diameter of the simulated sphere is only taken into account by setting a minimal gap-width. The tip scan range for the simulation around the crossing point is just 33×33 nm. A full-metal tip will have to be used to obtain a tip apex, that produces a field gradient, which is sufficiently large in such a scan range.

4.4.2 Coupling of a single emitter to a TLS

The nearby environment of a single molecule has an influence on its characteristics. The optical properties of a fluorescent molecule can be changed by choosing a different host matrix, for example. Furthermore, any kind of structural change occurring inside the matrix has an influence on the nearby molecules. Therefore, single molecules have been used as 'local probes' to investigate these kind of changes [10]. One kind of the structural changes of the matrix has been modelled as a two-level system (TLS) as introduced in Chapter 2.4. In the present section, a theoretical model is introduced presenting the influence of a nearby flipping TLS on the fluorescent pattern of a single molecule [61, 62, 60].

Mathematical derivation of the model

The Stark-shift pattern as a function of tip position has already been introduced in the previous section 4.3. Additionally, the effects of a nearby flipping TLS are included into this model. Hereby influences the electric field of the tip also the potential of the TLS. This influence results in a shift of the energy levels of the TLS. The energy levels E_i' of a TLS, which experiences an field-induced, additional Stark shift $\Delta\vec{\mu}'\vec{E}$,

can be expressed as:

$$E'_{1,2} = \pm\frac{E'}{2} = \pm 1/2\left((\eta - \Delta\vec{\mu'}\vec{E})^2 + \Delta_0^2\right)^{1/2},\tag{4.72}$$

where η is the asymmetry of the potential, $\Delta\vec{\mu'}$ the dipole moment difference of the TLS, $\vec{E}$ is the external, electric field and Δ_0 is the tunneling matrix element. The expression for the additional Stark shift of the TLS can be taken from the previous Stark-shift calculation for a single molecule. A permanent dipole moment is assigned to the TLS and shows therefore only a linear Stark shift. The permanent dipole moment is oriented in z-direction. From these assumptions follows:

$$\Delta\vec{\mu'}\vec{E} = G\frac{\Delta\mu' z}{R'^3},\tag{4.73}$$

where G is a factor depending on the applied voltage and taking the geometry of the tip into account, $\Delta\mu'$ is the dipole moment difference for the TLS, $R' = \sqrt{(x-x') + (y-y')^2 + z^2}$ the distance between TLS and the tip, whereas (x', y') is the position of the TLS. A transition from the ground to the excited state of a single TLS induces a frequency shift of the resonance of the molecule [61]:

$$\nu(t) = \nu_0 + \zeta(t)\nu',\tag{4.74}$$

where ν is the transition frequency of the molecule, ν_0 is molecule's transition frequency if the TLS is in the ground state, $\zeta(t) = 0$ or 1 corresponds to the TLS being in the ground or excited state and ν' is the induced shift to the chromophore. The induced shift ν' caused by a single TLS can be expressed by:

$$\nu' = 2\pi\alpha\frac{\cos\theta\eta}{E'r^3},\tag{4.75}$$

where α is the TLS-molecule coupling constant, θ is the orientation parameter between the TLS and molecule and r is the distance between molecule and TLS. This TLS-induced frequency shift is changed by the external, electric field of the tip from Eq. (4.73) to:

$$\nu' = 2\pi\alpha\frac{\cos\theta(\eta - \Delta\vec{\mu'}\vec{E})}{E'r^3}.\tag{4.76}$$

For further calculation, it is assumed, that the TLS flips faster than the scan velocity. Therefore, the time-averaged occupation probabilities are introduced:

$$n_1 = \frac{1}{1 + \exp(-\beta E')}\tag{4.77}$$

$$n_2 = \frac{1}{1 + \exp(\beta E')}\tag{4.78}$$

where n_1 and n_2 is the occupation probability for the ground and the excited state of the TLS, respectively and $\beta = 1/k_B T$. Now, the fluorescence $\tilde{I}$ of a single molecule

coupled to a nearby TLS is calculated. As long as the TLS is in the ground state, the fluorescence I_1 is equal to the occupation probability of the ground state of the TLS times the fluorescence expression for the field-shifted molecule resonance I from Eq. (4.48). If the TLS jumps to the excited state, the fluorescence I_2 is equal to the occupation probability of the excited state of the TLS times the field-shifted and TLS-shifted molecule resonance I':

$$
\begin{aligned}
\tilde{I} &= I_1 + I_2 & (4.79) \\
&= n_1 I(x,y,z) + n_2 I'(x,y,z) & (4.80) \\
&= \frac{1}{[1 + \exp(\beta E')]} \frac{\Gamma \nu_R^2}{[2\nu_R^2 + 4(\Delta\tilde{\nu} - \Delta\nu)^2 + \Gamma^2]} \\
&\quad + \frac{1}{[1 + \exp(-\beta E')]} \frac{\Gamma \nu_R^2}{[2\nu_R^2 + 4(\Delta\tilde{\nu} - \Delta\nu + \nu')^2 + \Gamma^2]} & (4.81)
\end{aligned}
$$

Numerical simulation of the Stark-shift pattern

The numerical simulation by Mathematica[4] yields the results presented in Fig. 4.8. The (x,y)-sections at different gap-widths show Stark-shift patterns of a molecule, which is coupled to a nearby tunnelling TLS. The single molecule is located at the center of the tip scan and possesses a linear Stark shift (aligned $\Delta\vec{\mu}$). At the position $(x_0', y_0') = (0.03, 0)\mu$m a TLS is placed. The TLS exhibits a permanent dipole moment, which has an angle of $\phi = -\frac{\pi}{10}$. It has been further assumed, that the TLS is locked in its ground state, which is a reasonable assumption for low temperatures. Further parameter have been estimated to $T = 0.9$ K, $\Delta_0 = 0.31 k_B T$, $\eta = 0.096 k_B T$, $\Delta\tilde{\nu} = 150$ MHz and $\alpha = 120$ MHz . Only at a certain position of the tip a flipping of the TLS is induced and the TLS jumps to the excited state. This jump of the TLS induces then an additional frequency shift of the molecules's resonance. The additional frequency shift results in a splitting of the Stark-shift ring of the molecule. The phenomenon is visible in Fig. 4.8 (a)-(h). The parameter for the TLS are chosen in the way, that a tip scan induces a large enough Stark-shift to allow the jump from the ground state to the excited state. At large gap-width (Fig. 4.8 (a)), here $z \geq 1.7\mu$m, a regular Stark-shift ring of a single molecule is visible. By approaching the tip to the sample (Fig. 4.8 (b) to(h)), the ring diameter of the Stark-shift pattern increases, followed by a decrease, and the ring width is decreasing. At a certain distance z, a splitting on he right side of the Stark-shift ring appears (Fig. 4.8 (c) to (e)). If the ring width is very broad, a splitting might not be visible. At small gap-width, $z \leq 0.4\mu$m, the splitting appears also on the right side of the Stark-shift ring (Fig. 4.8 (f) to (g)). Decreasing the gap-width even further, results in an double-ring pattern, where the dimmer ring is deformed (Fig. 4.8 (h))
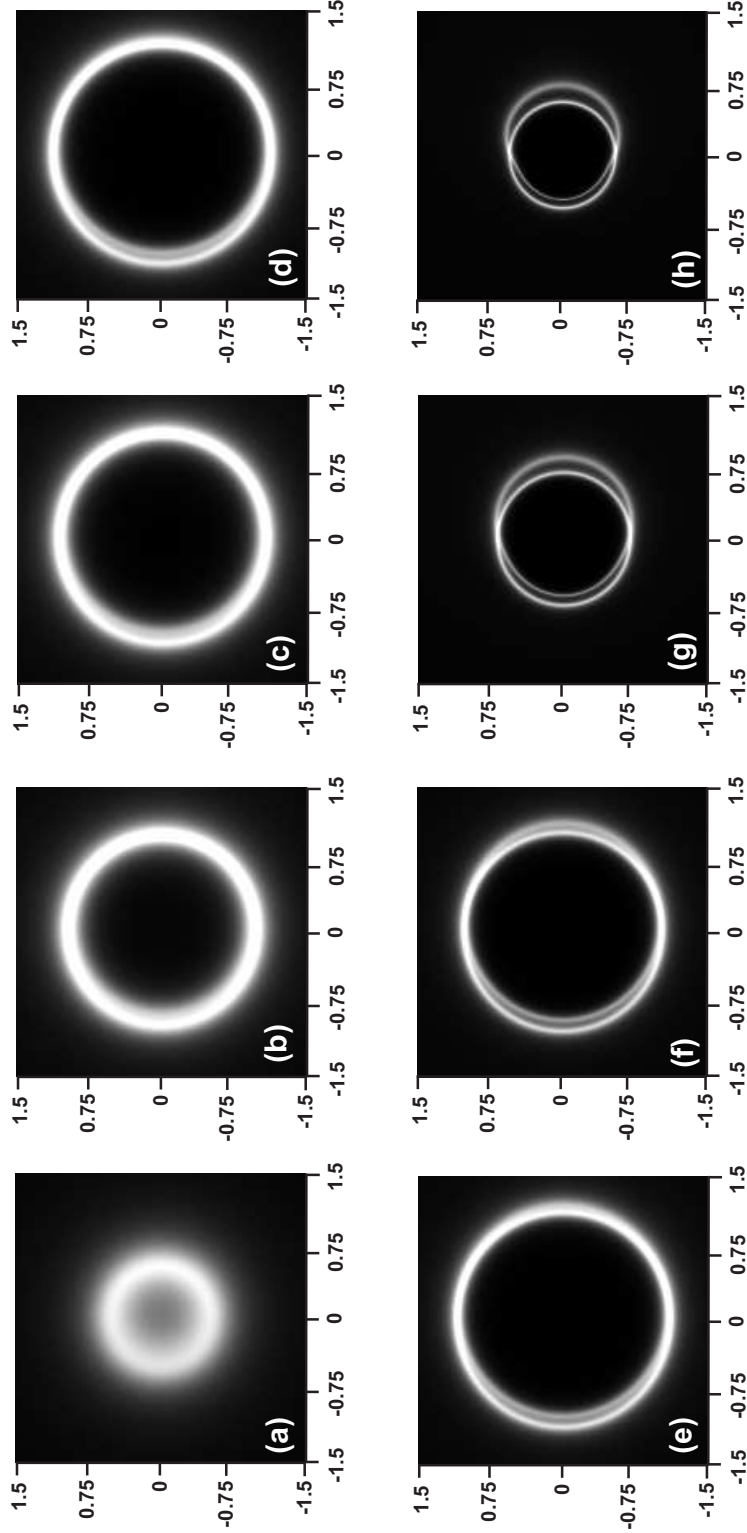
---

[4]Mathematica Version 5.0

Figure 4.8: Stark-shift patterns of a single molecule $(x_0, y_0) = (0, 0)$, coupled to a nearby TLS $(x'_0, y'_0) = (0.03, 0)\mu$m with a tilted dipole moment $\phi = -\frac{\pi}{10}$ at different gap-width. Further parameters have to be estimated: temperature $T = 0.9$ K, tunnelling matrix element $\Delta_0 = 0.31 k_B T$, asymmetry $\eta = 0.096 k_B T$, detuning $\Delta\tilde{\nu} = 150$ MHz, coupling $\alpha = 120$ MHz. (a) $z = 1.7\mu$m, (b) $z = 1.3\mu$m, (a) $z = 1.1\mu$m, (a) $z = 0.8\mu$m, (a) $z = 0.6\mu$m, (a) $z = 0.4\mu$m, (a) $z = 0.1\mu$m, (a) $z = 0.05\mu$m

Chapter 5

Performance of the experimental measurements

The experimental setup offers a large variety of parameter settings, with which the field-molecule interaction can be optimized. There is the tip voltage, the gap-width between tip and molecule, and the excitation frequency of the laser. But as long as it is not clear, what kind of effect the settings of the parameters have on the Stark-shift pattern, it is very difficult to control the experiment. The following chapter gives a flavor of the experimental parameter settings. The first sections presents a theoretical examination by using a simplified model of the theoretical model of Chap. 4. The second sections presents a measurement protocol which is called the five-points measurement. The last sections presents an overview of the experimental measurement.

5.1 Theoretical discussion of experimental parameter settings

In the following section, the dependencies of the experimental settings on the Stark-shift pattern are demonstrated. A simplified model is used, but nevertheless, the model is very helpful for the control of the experiment and the understanding of the data.

For simplicity, the assumption is made, that the tip has a sphere-like shape and the molecule shows a dominant linear Stark-shift behavior. With these assumption, the dependencies of the fluorescent pattern on the detuning, the applied voltage to the tip and the gap-width can be simulated. The field-induced Stark shift of a sphere-like tip has been calculated before and is taken from E. (4.18):

$$\Delta\nu(R,\theta,U) = \frac{A \mid \Delta\mu \mid}{R^3\,h}\,z,$$

with $R = \sqrt{x^2 + y^2 + z^2}$ being the tip-molecule distance with the molecule located at (0,0,0) with a permanent dipole moment difference oriented along the z-axis.
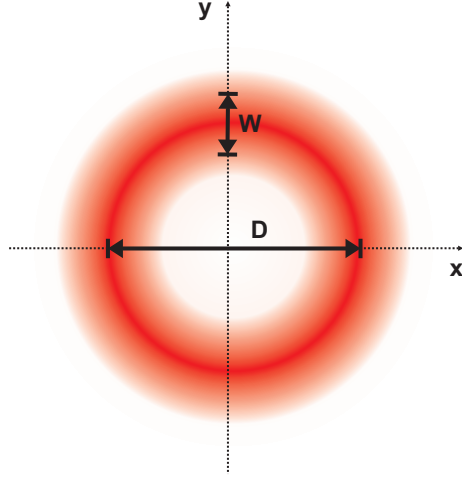
Figure 5.1: Stark-shift pattern of a single emitter which is located at the origin of the ring. The diameter D of the ring is defined as the distance from maximum to maximum. The ring width W is defined as twice the distance of maximum-FWHM of the ring.

As mentioned before, the resonance of a single molecule at cryogenic temperatures has a Lorentzian shape:

$$f(\nu_0) = \frac{B\Gamma_{HW}^2}{\nu_0^2 + \Gamma_{HW}^2},$$

where B is the amplitude of the ZPL, ν_0 is the resonance frequency and $2 \times \Gamma_{HW}$ is the line width of the molecule. Now, the linear Stark shift is introduced, which yields:

$$f(x, y, z) \;\; = \;\; \frac{B\Gamma_{HW}^2}{(\Delta\tilde{\nu} - \Delta\nu)^2 + \Gamma_{HW}^2}, \tag{5.1}$$

where $\Delta\tilde{\nu} = \nu_L - \nu_0$ is the detuning and $\Delta\nu$ is the field-induced Stark shift. This formula results in the same Stark-shift pattern as a function of the tip position as shown before in Section 4.3. Eq. (5.1) is a simplified version of the previous deduced formula for $I(x, y, z)$ in Eq. (4.48). Several characteristics of the ring, such as diameter D and ring width W, can be calculated in dependence on the experimental settings. Fig. 5.1 shows how the quantities D and W are defined. First, the maxima of the Stark-shift pattern function are calculated and from the that the diameter and the ring width is deduced. Finally, a five-point measurement method for the experiment is presented.

Maxima of the Stark-shift ring

When the field of the tip is of the correct orientation and the correct strength, the molecule is driven into resonance with the laser. By scanning the tip, circular Stark-

shift pattern are expected in the case of a linear Stark shift. Therefore, two maxima of the fluorescence-function $f(x, y, z)$ are expected in one line-scan. The positions of the maxima $x_{1,2}$ are calculated in 1D:

$$x_{1,2} = \pm\sqrt{\left(\frac{A \mid \Delta\mu \mid z}{h\Delta\tilde{\nu}}\right)^{\frac{2}{3}} - z^2}. \tag{5.2}$$

There are two maxima expected, as long as:

$$\frac{A \mid \Delta\mu \mid}{h\Delta\tilde{\nu}} - z^{\frac{4}{3}} > 0 \tag{5.3}$$

$$z < \left(\frac{A \mid \Delta\mu \mid}{h\Delta\tilde{\nu}}\right)^{\frac{3}{4}}. \tag{5.4}$$

If this requirement is not fulfilled, there is no Stark-shift ring. It is already apparent, that a suitable setting of the parameter, such as voltage and detuning, is necessary. Since the Stark-shift pattern is a ring and symmetric in 2D, the same results apply for the y-direction, by replacing $x_{1,2}$ with $y_{1,2}$. With this result, the diameter and the ring width can be calculated.

Diameter D of the Stark-shift ring

The diameter of the Stark-shift ring D can easily be calculated as the distance between the two maxima $x_{1,2}$:

$$D = \mid x_1 - x_2 \mid \tag{5.5}$$

$$= 2\sqrt{\left(\frac{A \mid \Delta\mu \mid z}{h\Delta\tilde{\nu}}\right)^{\frac{2}{3}} - z^2} \tag{5.6}$$

Of course, there are the same requirement for z as in the case for the maxima-calculation, otherwise no Stark-shift ring is detected. Since only the linear Stark shift is taken into account, the Stark-shift pattern is symmetric and the formula can be applied in 2D.

Ring width W of the Stark-shift ring

The ring width W is calculated by finding the positions $\tilde{x}$ in one dimension, where the fluorescence function $f(x, y, z)$ drops to the value of half of the maximum amplitude

B :

$$
\begin{aligned}
f(\check{x}) &= B/2 \\
\frac{\Gamma_{HW}^2}{(\Delta\tilde{\nu} - \Delta\nu)^2 + \Gamma_{HW}^2} &= 1/2 \\
\check{x}_{1,2} &= \pm\sqrt{\left(\frac{A \mid \Delta\mu \mid z}{h(\Delta\tilde{\nu} - \Gamma_{HW})}\right)^{\frac{2}{3}} - z^2} \\
\check{x}_{3,4} &= \pm\sqrt{\left(\frac{A \mid \Delta\mu \mid z}{h(\Delta\tilde{\nu} + \Gamma_{HW})}\right)^{\frac{2}{3}} - z^2}
\end{aligned}
$$

The ring-width W is now determined by twice the difference between the maxima $x_{1,2}$ and the half-amplitude position $\check{x}_{1,2}$:

$$
\begin{aligned}
W &= 2 \mid x_1 - \check{x}_1 \mid \\
&= 2\left(\sqrt{\left(\frac{A \mid \Delta\mu \mid z}{h\Delta\tilde{\nu}}\right)^{\frac{2}{3}} - z^2} - \sqrt{\left(\frac{A \mid \Delta\mu \mid z}{h\Delta\tilde{\nu} - \Gamma_{HW}}\right)^{\frac{2}{3}} - z^2}\right)
\end{aligned}
$$

The dependencies of the ring width on the voltage and the detuning are visualized later on.

Amplitude B of the Stark-shift ring

Up to now, it has been assumed that the amplitude of field-shifted fluorescence of the molecule B is the same as the amplitude of the unperturbed resonance. A simple calculation can confirm this assumption The amplitude of the fluorescence-function f at the position of the maxima $x_{1,2}$, which would correspond to the new amplitude B', is calculated:

$$
\begin{aligned}
f(x_1) = f(x_2) &= \frac{B\Gamma_{HW}^2}{\left(\Delta\tilde{\nu} - \dfrac{A|\Delta\mu|z}{h\left(\left(\left(\frac{A|\Delta\mu|z}{h\Delta\tilde{\nu}}\right)^{\frac{2}{3}} - y^2 - z^2\right) + y^2 + z^2\right)^{\frac{3}{2}}}\right)^2 + \Gamma_{HW}^2} \\
&= B' \\
&= B
\end{aligned}
$$

The amplitude of the ring structure is the same as the amplitude of the fluorescence peak.

Numerical simulation of the dependencies

The section gives an overview of the calculated dependencies of the voltage and the detuning on the width W and the diameter D. The settings of the experimental setup are important, especially if delicate measurement such as the coupling effects wants

to be done. For these kinds of measurements, the ring-diameter and ring-width has to be under control. According Eq. (5.7), it is obvious that the line width $2 \times \Gamma_{HW}$ of the molecule also has an influence on the width W. The smaller the line width, the sharper the width of the Stark-shift pattern. Since the line width of the molecule cannot be controlled experimentally (besides measuring at low temperatures), this dependency is not discussed any further. Fig. 5.2 and Fig. 5.3 visualize in different graphs the dependency of the Stark-shift pattern on the experimental settings. Fig. 5.2 concentrates on the influence on the detuning and Fig. 5.3 shows the influence of a change of the tip voltage. The voltage goes linearly into the pre-factor A of the formula for the Stark shift.

Dependency on the detuning $\Delta\tilde{\nu}$ The detuning $\Delta\tilde{\nu} = \nu_L - \nu_0$ is a very important setting. The Fig. 5.2 (a) shows a section of the Stark-shift ring along the x-axis at $y = 0$ at different detuning values between 100 MHz and 600 MHz. The amplitude B is constant. The values for the voltage-depending parameter A and the gap-width $z = 1\,\mu$m are kept fixed. Increasing the detuning $\Delta\tilde{\nu}$, the diameter as well as the width of the Stark-shift ring are decreased. By having a look at the Eq. (5.7) and (5.5) again, all parameters such as diameter D and width W are proportional $\propto 1/(\Delta\tilde{\nu} - \Delta\nu)$. This means that D and W depend on the difference between the detuning $\Delta\tilde{\nu}$ and the Stark shift $\Delta\nu$. Therefore, to increase the ring width W, the difference $\Delta\tilde{\nu} - \Delta\nu$ has to be decreased. The detuning has to be of the order of the Stark shift, and vice versa. This dependency is shown in Fig. 5.2 (b) and (c). Fig. 5.2 (b) shows the ring width W plotted over the gap-width z with different detuning $\Delta\tilde{\nu}$. The larger the detuning, the smaller the ring width, which can be seen by drawing a vertical line at a fixed value for z. It has to be pointed out, that at a certain gap-width z, the dependency for the width W on the detuning changes as can be seen in Fig. 5.2 (b). The function for the width becomes singular, the graph shows a strong upturn. By hitting this limit with the parameter setting, no Stark-shift ring is obtained anymore. There is another parameter setting, with which the dependency of the width W on the detuning is reversed. The width of the Stark-shift ring becomes larger by increasing the detuning. The dependency of W on the gap-width z is also visible. By increasing the gap-width, the ring width decreases. This behavior depends on the change of the field strength by approaching the tip to the molecule, as discussed before.

The same dependency of the width on the detuning is valid for the ring diameter D, which can be increased by decreasing the difference between $\Delta\tilde{\nu}$ and $\Delta\nu$, as can be seen in Eq. 5.5. In Fig. 5.2 (c), the diameter D is plotted over the gap-width z. The diameter is decreased by increasing the detuning. In contrast to the ring width, the dependency on the detuning never changes for the diameter. There does not exist a region, where the behavior is reversed, as discussed for the ring width. The diameter depends also on the gap-width. By approaching the tip to the sample, diameter D increases and then decreases . This effect depends on the angle between the dipole
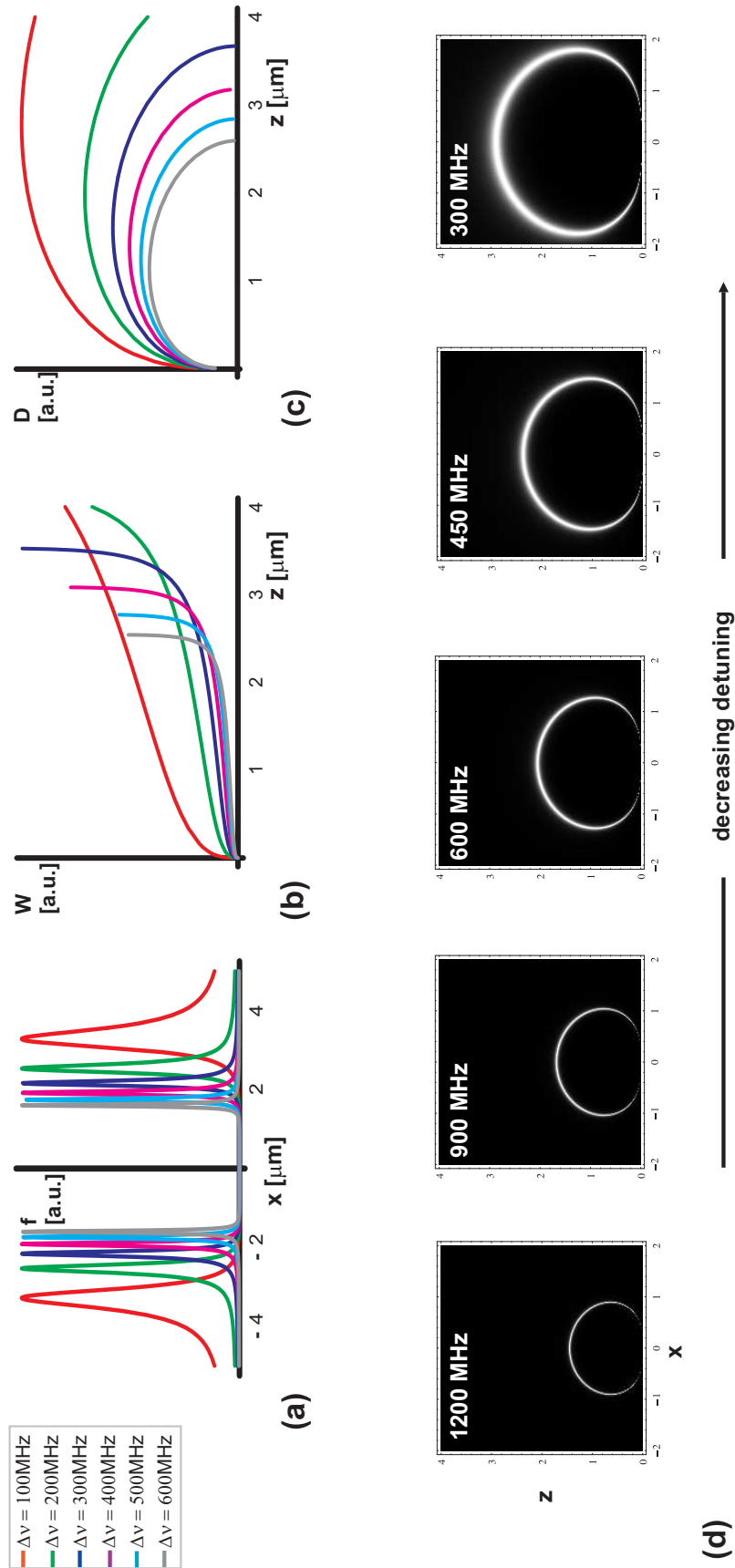
Figure 5.2: Dependence of the Stark-shift pattern on the experimental settings on the detuning. Influence of the detuning, ranging from 100 to 600 MHz, on the Stark-shift pattern (a), the width W (b) and on the diameter D (c). Section along (x,z)-plane, with a decreasing detuning $\Delta\tilde{\nu}$ from left to right (d).

moment difference $\Delta\vec{\mu}$ and the electric field E as discussed before in Section 4.3. For visualization, the second row in Fig. 5.2 (d) shows a series of sections along the (x,z)-plane at $y = 0$. From left to right, the detuning is decreasing. It is seen, that the diameter and the ring width at a fixed gap-width z (horizontal line), are increasing, with decreasing detuning value. That is one possibility to tune the Stark-shift balloon of a single molecule.

Dependency on the tip voltage In Fig. 5.3, the influence of the voltage is discussed. In the section of the Stark-shift pattern in Fig. 5.3 (a), it becomes apparent, that the diameter of the Stark-shift ring becomes larger with increasing voltage. The voltage effect on the width W is not as large as by changing the detuning as shown in Fig. 5.3 (b). The detuning for all graphs is fixed to $\Delta\tilde{\nu} = 600$MHz. Again, there is a region for the ring width W, where the dependency on the voltage is reversed, and the width becomes smaller by increasing the voltage. In Fig. 5.3 (d) a series of section along the (x,z)-plane at $y = 0$ are shown. The voltage is increased from left to right. It is very nicely visible, how the Stark-shift balloon grows lager with increasing voltage.

At the end, it should be pointed out again, that all the theoretical calculation has been carried out with the assumption of a perfectly shaped tip. The tip has been modelled as a sphere. Therefore, the minimum gap-width has been the sphere radius, which has been set to 50 nm. Tips in the experiment have a larger diameter. It might also be, that the approximation of a sphere-like tip is too rough. Therefore, the influence of the parameter settings might not be as strong as in the simulation in the previous section 4.3. For example, the decrease of the Stark-shift ring diameter has been hardly detectable by assuming a cone-shaped tip.

5.2   Five-points measurement

The previous section presented the dependencies of the Stark-shift ring on the experimental parameter settings. It became clear, that only with a suitable choice of set points for the voltage U, the detuning $\Delta\tilde{\nu}$ and the gap-width z, the detection of a Stark-shift ring is possible. Because of the large variety of parameter settings, it can be quite tedious to find the suitable set points. Additionally, the relative position between the molecule and the tip is not known. By overlaying the image of the tip with the reflected spot of the focal plane, the molecule might end up to be located at the edge of the tip's scan range. Tip-scan images can be taken in a trial-and-error process to adjust the molecule-tip position and the parameter settings. Since this trial-and-error procedure is time-consuming, an experimental protocol has been elaborated which consists of excitation spectra taken at five different positions of the biased tip (U=const.). This procedure is called the five-points spectrum. By means of these five spectra, a quick overview of the choice of parameter and position is
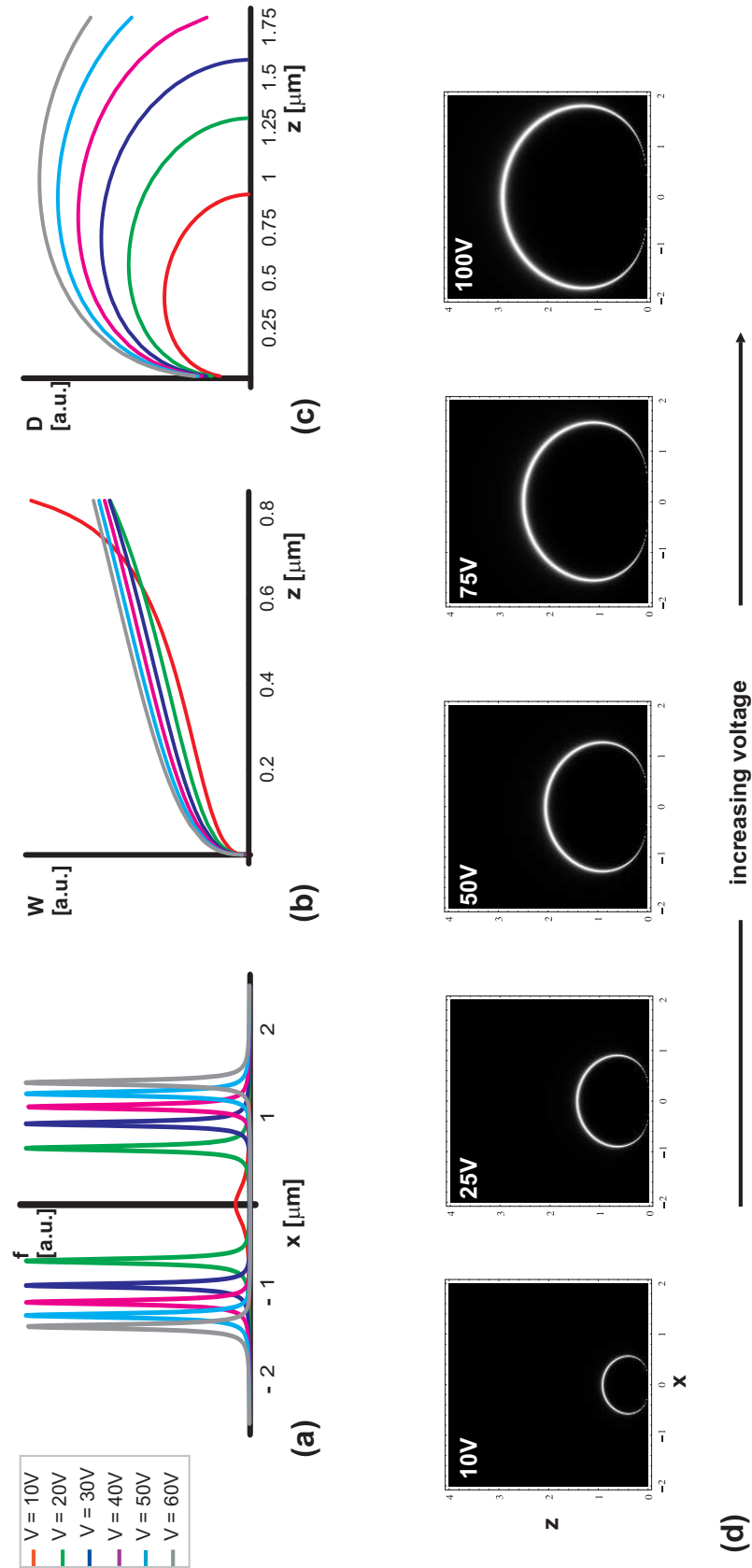
Figure 5.3: Dependence of the Stark-shift pattern on the voltage. Influence of the tip voltage, ranging from 10 to 60 V, on the Stark-shift pattern (a), the width W (b) and on the diameter D (c). Section along (x,z)-plane, with an increasing voltage U from left to right (d).
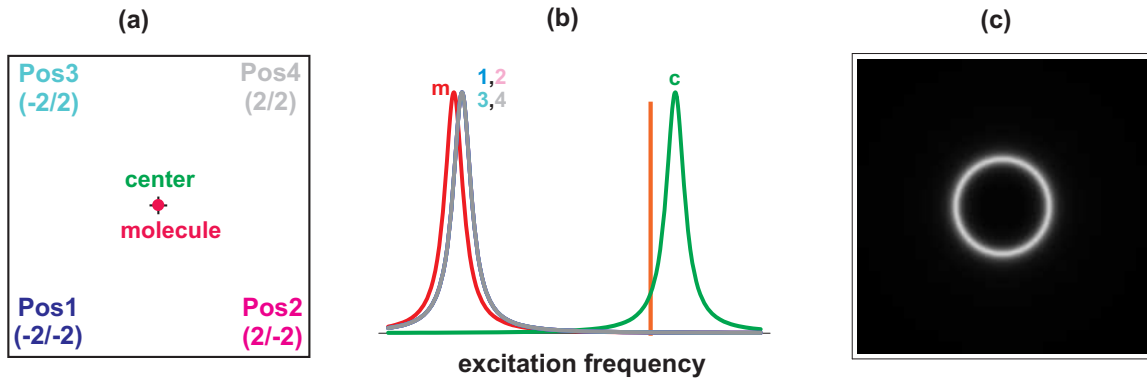
Figure 5.4: Case 1 (a) The molecule is located right in the center of the scan range of the tip. (b) Five-points spectrum, measured at different tip positions: edges '1,2,3,4'; center 'c'; undisturbed resonance 'm'. (c) Calculated stark-shift pattern by choosing the laser frequency as indicated by the straight line in (b).

obtained. The five positions of the tip are the center position and the four edges of the scan range. In the case of $\Delta \vec{\mu} \parallel z$, the closer the tip to the molecule, the larger the induced Stark-shift. The tip position, causing the largest Stark shift of the resonance, is therefore closest to the molecule's position. Furthermore, it has been discussed before, that the detuning $\Delta \tilde{\nu}$ should be of the same order as the Stark shift $\Delta \nu$ for reaching a small width W of the Stark-shift ring. The excitation frequency should therefore be fixed close to the maximum Stark shift of the molecule. By the outcome of the five-point spectrum, it is possible to judge, if the molecule is centered in the scan range of the tip and at which value the excitation frequency should be fixed.

In the following, four examples of a five-point spectrum are discussed, whereas the position of the molecule in the tip's scan range varies from case to case. The four examples are presented in Fig. 5.4 to Fig. 5.7. The figures are divided in three parts. The first part, (a), shows the scan range of the tip, including the molecule position and the five points of the tip, at which the spectra are taken. The positions are the center position and the four edges of the scan range, respectively. The numbers at the four edges indicate the value for the simulation, which is a 4×4 μm scan ranges. The second part, (b), of the picture shows the resonance of the molecule at different tip positions together in one spectrum. The zero-field molecule resonance, which is independent of the tip position, is shown as a reference and is marked with the letter 'm'. The Stark shift at the center position is marked by the letter 'c', and the Stark shifts at the four edges are numbered '1' to '4'. The maximum Stark shift is induced, when the tip is above the molecule. Since the spectrum is taken at only five positions of the tip, which do not necessarily coincide with the molecule position, the maximum Stark shift might not be measured. Only the position, which is closest to the molecule, shows a larger Stark shift compared to the other four tip positions.
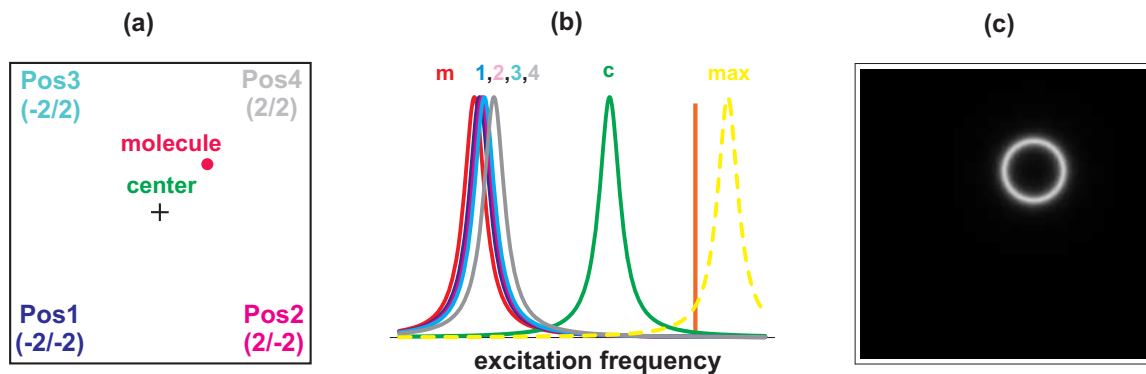
Figure 5.5: Case 2 (a) The molecule is located a bit off-center of the scan range of the tip. (b)five-point spectrum at the five different tip positions: edges '1,2,3,4'; center 'c'; undisturbed resonance 'm'; maximum Stark shift 'max' at the position of the molecule, which is not directly measured. (c)Calculated Stark-shift pattern by choosing the laser frequency as indicated by the straight line in (b).

The maximum Stark shift, if not directly measured with the five-point spectrum, is indicated as a dashed line in the spectrum and marked by the initials 'max'. Finally, the last part (c) of the figures shows a simulated Stark-shift pattern, whereas the fixed excitation frequency is marked in the spectrum (b) by a straight line.

Case 1   The most favorable case is, when the molecule is located in the center of the tip scan, as shown Fig. 5.4 (a). This means, that the largest Stark shift in the five-point spectrum is induced, when the tip is in the center position of the scan range. Fig. 5.4 (b) shows the spectrum. The resonance of the molecule is shifted to higher frequencies. The Stark shift at the corner positions are all equal, since the tip-molecule distance is for all positions the same. These four shifted resonance peaks overlap each other. Therefore, only one peak is visible for the edges '1,2,3,4'. The center position induces the maximum Stark shift. This is the indicator, that the molecule is located close to the center position. By choosing the excitation frequency as marked in Fig. 5.4 (b), a Stark-shift pattern is obtained as shown in Fig. 5.4 (c). In the case of the centered molecule, it is obvious how to set the laser frequency. The resonance frequency is shifted to higher frequencies and the maximum induced Stark shift is at center position. This is the maximum frequency range, which is accessible by moving the tip. Therefore, the frequency is set at the right of the zero-field resonance, but to the left of the shift at center position.

Case 2   The molecule is located a bit off-center, closer to the position 4 as marked in Fig. 5.5 (b). The influence of the off-center position becomes immediately apparent in the five-points spectrum in Fig. 5.5 (b). The Stark-shift at the four edges differ, since now the corner positions have different distances to the molecule. Since the
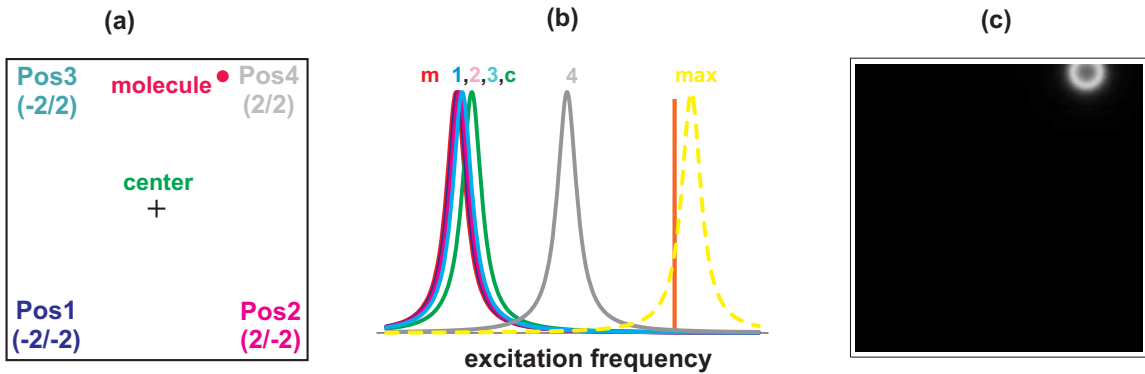
Figure 5.6: Case 3 (a) The molecule is located close to position 4 of the scan range of the tip. (b) five-point spectrum at the five different tip positions: edges '1,2,3,4'; center 'c'; undisturbed resonance 'm'; maximum Stark shift 'max' at the position of the molecule, which is not directly measured. (c) Calculated Stark-shift pattern by choosing the laser frequency as indicated by the straight line in (b).

molecule is still closest to the center, the center position of the tip 'c' induces still the largest Stark-shift, followed by the Stark shift induced at position 4. Now, the five-point spectrum does not cover the whole field-induced Stark-shift range. At the position of the molecule, the maximum Stark-shift would be measured, as indicated by the dashed line 'max'. To take a full Stark-shift ring image as shown in Fig. 5.5 (c), the excitation frequency has to be chosen right of the maximum measured Stark-shift peak 'c', in contrast to Case 1.

Case 3 The molecule is located just at the rim of the scan range of the tip, close to position 4, as shown in Fig. 5.6 (a). In the five-points spectrum Fig. 5.6 (b), tip position '4' induces now the largest Stark-shift, since it has the smallest distance to the molecule. The other tip positions induce a Stark shift in the order of 'c'-'3'-'2'-'1', depending on their distance to the molecule. If the largest Stark shift is induced in one of the corner position, a whole Stark-shift ring might not be measured with any kind of settings. It depends on how close the molecule is to the rim of the scan range. The laser frequency has to be set also on the right side of the peak '4', since the maximum Stark shift 'max' lies by even higher frequencies. It is visible in Fig. 5.6 (c), that one part of the Stark-shift ring is cut off, even by choosing the laser frequency closely to the maximum measured Stark shift.

Case 4 The molecule is located outside the maximum scan range of the tip, as shown in Fig. 5.7 (a). In this case, the largest induced Stark shift appears in one of the corner position '4', followed by a another corner position '3', Fig. 5.7 (b). If the center position induces such a small Stark shift, a measurement of a complete Stark-shift ring is impossible. By choosing the laser frequency close the maximum
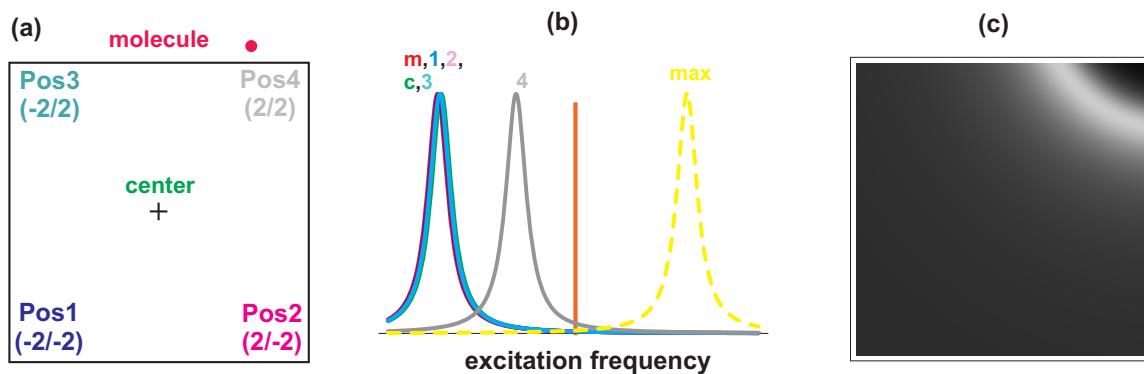
Figure 5.7: Case 4 (a) The molecule is located outside the scan range of the tip. (b) Five-point spectrum at the five different tip positions: edges '1,2,3,4'; center 'c'; undisturbed resonance 'm'; maximum Stark shift 'max' at the position of the molecule, which is not directly imaged. (c) Calculated Stark-shift pattern by choosing the laser frequency as indicated by the straight line in (b).

Stark-shift at position '4', a part of the Stark-shift ring becomes visible. Choosing such a big difference between the detuning and the actual maximum Stark shift at 'max' results in a huge Stark-shift ring, which is detectable in the upper corner of the tip scan, Fig. 5.7(c). In such a case, it is inevitable to move the tip.

The five-point spectrum gives a quick overview, if the tip is well positioned above the molecule. By adjusting the position of the tip and the laser excitation frequency, a tip scan can be started. The drawback of the five-point spectrum is, that it is only applicable for one or at the most two molecules. The spectra get too complicated with more peaks, and the shift of the resonances cannot be assigned to the different molecules anymore.

5.3   Experimental protocol

We have developed an experimental protocol for imaging of single molecules by Stark-shift microscopy at low temperature. The experimental procedure starts with a confocal scan at a high excitation intensity of about 500nW. After the sample scan, a desired area of the sample where a fluorescence signal has been detected, is moved into the focus. The excitation intensity is decreased to avoid power broadening and light-induced spectral jumps. Some spectra are taken to investigate the number of molecules in that area and their spectral stability. The position of the sample area is adjusted in vertical and horizontal position in order to achieve the highest intensity of the zero-phonon lines. If the settings for the excitation are optimized, the tip is brought into position above the objective. The optically observed approach of the tip is started, until the tip is positioned satisfactorily over the objective. Excitation spectra are then taken at different tip positions:

- tip in center position, but without any voltage applied: zero-field resonance ν_0.

- tip in center position with different voltages applied to investigate the nature of the Stark shift of the molecules: linear or quadratic Stark shift.

- tip at different position with a fixed tip voltage fixed (five-points measurement): Stark shift depending on tip position.

When finished, the scan control is switched from sample scan, to tip scan. The settings for the tip voltage and the detuning for the tip scan are made according to the results of the five-points measurements. It is important, that the Stark-shift is large enough to hit the laser frequency at a certain tip position. After all these settings are performed, a tip scan can be started.

Chapter 6

Experimental results and discussion

The present chapter starts with a section about the data analysis. In the second section, parameter settings, such as the excitation frequency, and some general remarks about the experimental discussion are pointed out. The section about the experimental results starts with the demonstration of the general behavior of the Stark-shift pattern depending on the setting of the parameters such as the tip voltage and the detuning. The results are discussed and compared with theoretical predictions of Chapter 5.1. Even though many approximations have to be done for the sake of computation, the developed theoretical model reproduces the experimental results in good agreement. In the following, experimental results on Stark-shift patterns of single molecules are presented. The focus is on the influence of the gap-width on the Stark-shift pattern of the molecule. Another issue is the orientation determination of a dipole moment difference $\Delta\vec{\mu}$ and the coupling of a single molecule to a neighboring TLS. These effects have been already presented in the theoretical discussion in Chapter 4.4.2. Finally, experimental results on distinguishing several molecules in a single tip-scan are presented.

6.1 Data analysis

The section about the data analysis is divided in two parts. The first part is concerned with the analysis of the spectra. The next section discusses the analysis of Stark-shift patterns. The data analysis is based on the theoretical models derived in Chap. 4.

6.1.1 Spectra

At low temperatures, the zero-phonon lines of a single molecule can be described by a Lorentzian function, as discussed section 2.1.1. By fitting a Lorentzian to the resonance of a single molecule, the line width of the molecule and its spectral position can be determined. Determination of the resonance frequency of the ZPL is important

for calculating the Stark shift. The Lorentzian has been parameterized as follows:

$$F = of + \frac{A\Gamma_{HW}^2}{(\nu - \nu_0)^2 + \Gamma_{HW}^2}$$

with of an offset, A the amplitude, $2 \times \Gamma_{HW}$ the line width of the ZPL, ν the excitation frequency and ν_0 the resonance frequency of the single molecule.

6.1.2   Stark-shift pattern

Recording the fluorescence of a single molecule as a function of tip position results in certain patterns depending on certain characteristics of the molecule as discussed in Chap. 4. The analysis of the Stark-shift patterns can be very complex, since the shape and appearance of the patterns depends strongly on many parameters.

Linear Stark shift

The Stark-shift pattern of a single molecule with a dominant linear Stark shift ($\Delta\vec{\mu} \parallel z$) is a ring-like pattern and can be fitted by:

$$f(x, y, z) = of + \frac{A\Gamma_{HW}^2}{\left(n - \frac{bz}{[(x-x_0)^2 + (y-y_0)^2 + z^2]^{(3/2)}}\right)^2 + \Gamma_{HW}^2}, \qquad (6.1)$$

with of an offset, A the amplitude of the fluorescence, $2 \times \Gamma_{HW}$ the line width of the resonance, $\Delta\tilde{\nu}$ the detuning between laser frequency and the zero-field resonance frequency of the single molecule, b a geometrical factor proportional to the applied voltage to the tip, z the gap-width, (x,y) the position of the tip and (x_0, y_0) the position of the molecule. This equation is derived from Eq. 5.1, including the linear Stark shift from Eq. 4.18. The only unknown parameter in this fit formula is the gap-width z. Therefore, fitting the Stark-shift pattern of a single molecule yields the tip-molecule distance by approximated b.

If more than one molecule is in the focus and the field pushes more than one molecule into resonance with the laser, several rings can appear. Fitting of the data results in an accurate analysis of the position of the molecules and their relative distance to each other. Since Eq. 6.1 requires the knowledge of many parameters for each molecules, the position determination can be very complicated. For simplicity, another formula can be derived, which takes only the geometry of the Stark-shift pattern into account. In the case of the linear Stark-shift with $\Delta\vec{\mu} \parallel z$, the equation for a ring is used:

$$\left(\frac{D}{2}\right)^2 = (x - x_0)^2 + (y - y_0)^2, \qquad (6.2)$$

with D the diameter of the ring, and (x_0, y_0) as the center coordinates. Therefore, for position determination of the molecules, ring-like Stark-shift patterns can be fitting

by a Lorentzian depending only on the spatial position:

$$f(x, y, z) = of + \frac{C \left(\frac{W}{2}\right)^2}{\left(\frac{D}{2} - \sqrt{(x - x_0)^2 + (y - y_0)^2}\right)^2 + \left(\frac{W}{2}\right)^2}. \tag{6.3}$$

Here, of is the offset, C is the amplitude of the Stark-shift ring, W is of the width of the Stark-shift ring, (x, y) is the tip position and (x_0, y_0) is the molecule position. This fit-equation does not require any knowledge about the spectral parameter, such as the detuning or the Stark shift.

Quadratic Stark shift

The Stark-shift pattern of a single molecule with a dominant quadratic Stark shift has an elliptical pattern and can be fitted by:

$$f(x, y, z) = of + \frac{A\Gamma_{HW}^2}{\left(n - \frac{d}{R^6}(a(x - x_0)^2 + b(y - y_0)^2 + z^2)\right)^2 + \Gamma_{HW}^2}, \tag{6.4}$$

with d the pre-factor taking into account the voltage and the polarizability, $R = \sqrt{(x - x_0)^2 + (y - y_0)^2 + z^2}$ the distance between tip and molecule, and (a, b) the ratios of the polarizability $\Delta\alpha_{cc}$. This equation is derived from the equation Eq. 5.1, including the quadratic Stark shift from Eq. 4.22.

The quadratic Stark shift pattern can also be fitted by an equation taking only the geometry of the pattern into account. In the case of the pure quadratic Stark-shift, the equation for an ellipse is used:

$$\tilde{a}^2\tilde{b}^2 = \tilde{b}^2(x - x_0)^2 + \tilde{a}^2(y - y_0)^2, \tag{6.5}$$

with $\tilde{a}, \tilde{b}$ the minor and the major axis, respectively and (x_0, y_0) as the center coordinates. The Stark-shift pattern can be fitted by a Lorentzian depending only on the spatial position of the molecule:

$$f(x, y, z) = of + \frac{C \left(\frac{W}{2}\right)^2}{\left(\underbrace{\tilde{a}\tilde{b} - \sqrt{\tilde{b}^2(x - x_0)^2 - \tilde{a}^2(y - y_0)^2}}_{n}\right)^2 + \left(\frac{W}{2}\right)^2}. \tag{6.6}$$

The parameter $\tilde{a}, \tilde{b}$ are directly connected to the ratios a, b of the polarizability $\Delta\alpha_{cc}$. If the ellipse is not only moved from the $(0, 0)$-position of the tip scan, but also turned by a certain angle ϕ, the term n of equation (6.6) can be written as:

$$n = \tilde{a}\tilde{b} - \sqrt{\tilde{b}^2 \left((x - x_0)\cos(\phi) - (y - y_0)\sin(\phi)\right)^2 - \tilde{a}^2 \left((y - y_0)\cos(\phi) + (x - x_0)\sin(\phi)\right)^2}. \tag{6.7}$$

6.2 Preliminary Considerations

As discussed in section 3.1.1, there are different possible excitation frequencies for the p-terphenyl/terrylene system. Molecules at the X_1-site or at the X_3-site (see Table 3.1) are not photostable, so they are not suitable for the shift-sensitive Stark-shift measurements. Molecules at X_2-site and at the X_4-site are photostable. The frequency, used in our experiments, is set to the X_2-site around $k = 17286 \text{cm}^{-1}$. The excitation intensity has been reduced by the filter wheel (see Fig. 3.7) to about 30 to 1 nW during the tip scans. During the confocal scans, it has been increased to about 300 to 500 nW. The higher intensity makes it easier to excite the molecules with the narrow band laser, since the ZPL is power-broadened and more molecules will be in resonance with the laser. The laser excitation power has been measured with a power-meter after the wedge (W) (see Fig. 3.7). Therefore, the actual excitation power at the location of the sample might be a bit lower, since the laser beam passes the two cryostat windows.

Another important setting is the integration time per pixel for the images and spectra. In the original software (DSP 6.0), the integration time for the confocal images is 3 ms per pixel and the integration time for the spectra is 16.9 ms per point. In the new software (labview 6.1), the integration time for the confocal images is still 3 ms per pixel and for the spectra 20 ms per point.

It has to be pointed out, that the laser frequency ν_L and also the resonance ν_0 of the molecule are expressed in MHz or GHz, which is the detuning of the center frequency of the laser. The maximum frequency scan range of the dye laser is ± 15 GHz. For example, stating a frequency $\nu_L = -3.5$ GHz means that the excitation frequency is detuned by 3.5 GHz from the center frequency of the laser towards smaller frequencies. The detuning $\Delta\tilde{\nu} = \nu_L - \nu_0$ is the frequency difference between the zero-field resonance of the molecule ν_0 and the excitation frequency ν_L. The parameter $\Delta\nu$ is the Stark shift of the molecule, defined as $\Delta\nu = \nu_e - \nu_0$. Finally, the frequency $\Delta\nu'$ is defined as the difference in the Stark shift between the corner position of the tip within it scan range and the center position: $\Delta\nu' = \Delta\nu_{center} - \Delta\nu_{corner}$.

The experimental results are obtained from sublimated and from spin-coated samples. Even though it will be mentioned which kind of sample has been used, the data sets are not specially divided into data obtained with sublimated crystals and spin-coated micro-crystals. The fluorescent molecules and the matrix are the same. It has been noticed, however, that the line width of the ZPL are often smaller for molecules in spin-coated micro-crystals as in sublimated crystals. This might be connected to an observed expansion of the lifetime of single molecules in thin samples [97].

6.3   The Stark shift depending on the tip-position

The electric field produced by the biased tip has to have a large field gradient to be successfully applied to Stark-shift microscopy. It is essential, that moving the tip by small distances (nm-range) results in a suitable Stark-shift difference at the different tip positions. Or, to put it another way, $\Delta\nu' = \Delta\nu_{center} - \Delta\nu_{corner}$ has to be at least of the order of the line width of the molecule. We may ask ourselves, how large the actual Stark shift is, which can be induced by the usage of a tip with a diameter of $d \sim 100$ nm and a gap-width of maybe $z \sim 2 - 3$ μm. The data set of a five-points measurement (discussed in Chap. 5.2) will give an example of a Stark-shift range, which is possible by moving the tip within its maximal scan range of 5×5 μm.

Fig. 6.1 shows a sequence of spectral measurements of a single molecule at low temperatures. The spectra are measured with the tip at different positions within its scan range. The data are taken with a sublimated crystal. The gap-width is not known, since shear force gap-width control has not been operating. Since further approach steps have been taken later on during the measurements, the gap-width for these spectra is assumed to be in the range of a few micrometers. The excitation power of the laser is set to $P = 30$ nW. Fig. 6.1 (a) shows the resonance of the single molecule without any voltage applied to the tip. The resonance of the molecule has a line width $\Gamma = 54$ MHz and an amplitude A of 138 ± 5 counts. The spectral position is at $\nu_0 = 128$ MHz. Then, the tip is put into the center position of its scan range and a voltage of $U = 30$ V is applied to the tip. Fig. 6.1 (b) shows the resonance after switching on the voltage. The field-induced Stark shift $\Delta\nu$ amounts to 176 MHz to higher frequencies. Switching on the voltage results also in a slight broadening of the peak with $\Gamma = 64$ MHz and an decrease of the amplitude A to 113 ± 1.5 counts. The broadening and the decreased amplitude remains as long as the voltage is switched on. These effects might be connected to the activation of a TLS system in the matrix. Fig. 6.1 (c)-(f) shows the Stark shift of the ZPL by positioning the tip in the four corners of its scan range. Since the scan range of the tip is $5 \times 5\mu$ m, the in-plane distance d between the center position and one of the corner-positions is $d \sim 3.5$ μm. The molecule is obviously not in the center of the scan range of the tip, since the Stark-shift difference $\Delta\nu'$ of the four corners differ. The shift-difference between the center position and the corner-positions is between $\Delta\nu' = 1$ MHz (corner4) and $\Delta\nu' = 117$ MHz (corner2) towards higher frequencies. The fit-results of the spectra are summarized in table 6.1.

To summarize, moving a tip with an apex of about 100 nm in x,y-direction by 3.5 μm at a gap-width of a few μm results in Stark shifts of the ZPL in the range of 100 MHz with a voltage of just 30V. Applying larger voltages to the tip results in larger Stark shifts compared to the field-free resonance ν_0. But the Stark-shift $\Delta\nu'$ induced within the scan range of the tip, depends only on the field gradient of the tip. To induce a larger Stark shift $\Delta\nu' > 117$ MHz within the scan rang of the
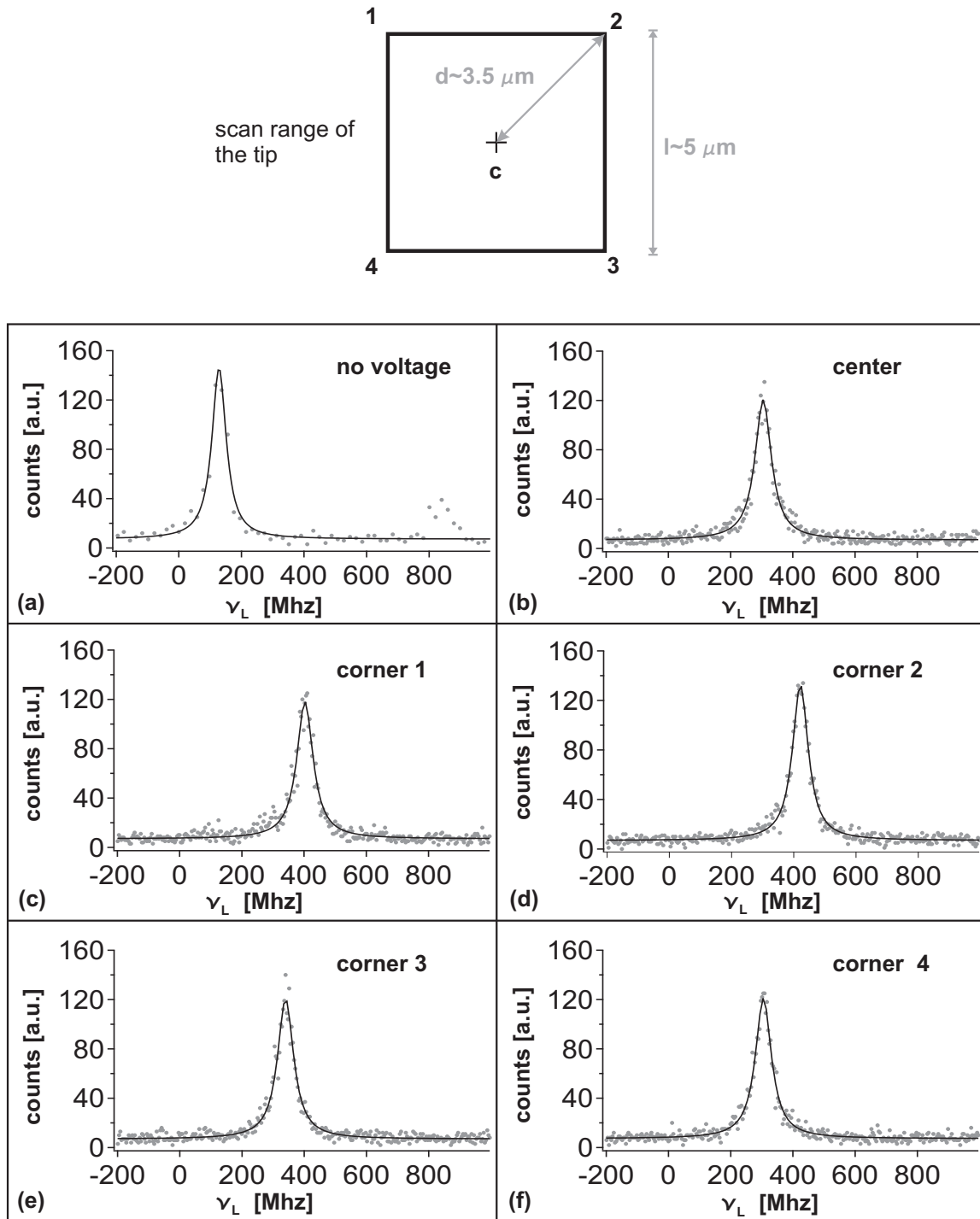
Figure 6.1: Stark shift depending on tip position, measured in a five-points measurements, see section 5.2. Stark shift depending on tip position, imaged with a excitation power of 30 nW. (a) Field-free resonance of the molecule. (b) Tip in center position of the scan range with an voltage of $U = 30$V applied to the tip. (c)-(f) Tip positioned in one of the four corners of the scan range with a voltage of $U = 30$V applied to the tip.

tip	field free	center	corner1	corner2	corner3	corner4
voltage	$U = 0$	$U = 30$ V	$U = 30$ V	$U = 30$ V	$U = 30$ V	$U = 30$ V
Γ [MHz]	54 ± 3.4	63.8 ± 1.2	63.4 ± 1.4	61 ± 1	62 ± 1.2	62 ± 1.1
A [counts]	138 ± 5	113 ± 1.4	111 ± 1.7	125 ± 1.4	113 ± 1.5	113 ± 1.4
ν_i [MHz]	128 ± 1	304 ± 0.4	402 ± 0.5	421 ± 0.4	340 ± 0.4	305 ± 0.4

Table 6.1: Overview of the fit-results for the spectra depending on tip position, shown in Fig. 6.1. ν_i are the frequencies at zero-voltage ($i = 0$) and at the different biased-tip positions ($i = c, 1, 2, 3, 4$).
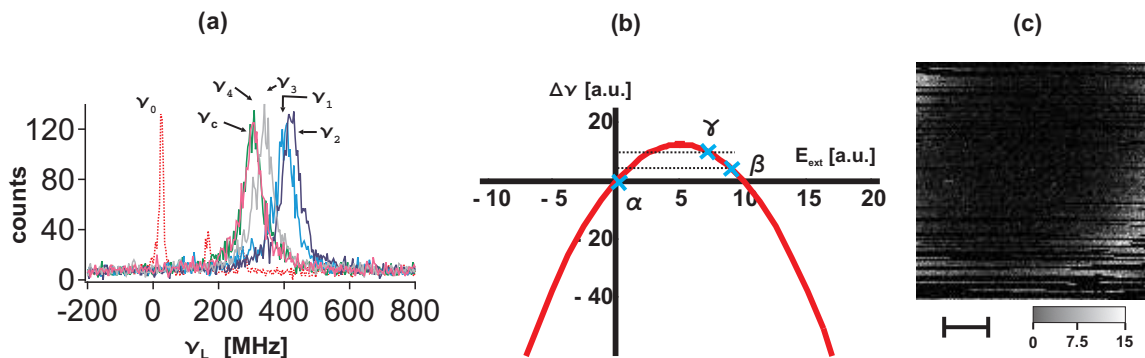

Figure 6.2: (a) Experimental example of the five-points measurement, introduced in Chapter 5.2. All 6 spectra of Fig. 6.1 are plotted into one graph. (b) Explanation of the Stark-shift behavior depending on tip position. The molecule exhibit a linear and a quadratic component of the Stark shift, respectively. For explanation, see text. (c) Stark-shift pattern of the molecule with an excitation frequency of $\nu_L = 140$ MHz and an applied voltage of $U = 30$ V. Scalebar is 1 μm and the grey-scale is in counts.

tip, a smaller gap-width z or a sharper tip is necessary. Nevertheless, for Stark-shift microscopy, it is sufficient to induce shifts of the ZPL in the range of the line width Γ. These numbers for the Stark shift give only an idea of possible Stark shifts depending on tip position. The electric field strength of the tip depends very strongly on the electric contact to the tip. If the resistance of the metallized tip is high, a higher voltage is necessary to produce the same electric field strength. Consequently, every tip behaves a bit differently, since the contact resistance is difficult to control.

The presented spectral measurements are an example for the application of the five-points measurement, presented in Chapter 5.2. In Fig. 6.2 (a), the 6 spectra are plotted together in one graph. The center position of the tip shows the smallest Stark shift of $\Delta\nu = \nu_0 - \nu_c = 176$ MHz. The four corner-position ν_{1-4} show larger Stark-shifts between $\Delta\nu = 177$ MHz and $\Delta\nu = 293$ MHz. The Stark shift increases by moving the tip away from the center position, even though the value measured at the corner position at ν_4 overlaps almost with ν_c. The conclusion is therefore, that the molecule is positioned slightly off-center within the scan range.

The Stark-shift depending on tip-position, shown in Fig. 6.2 (a), seems to show an anomalous behavior at the first look. Switching on the voltage and positioning the tip in center position results in a shift towards larger frequencies. Moving the tip from the center position into one of the corners, which is the same as decreasing the voltage at a fixed tip position, results also in a shift of the ZPL towards larger frequencies. One would expect, that moving the tip towards one of the corners, away from the molecule, the Stark shift gets smaller. Fig. 6.2 (b), where a calculated Stark-shift as a function of the electric field is shown, clarifies this effect. This particular Stark-shift behavior can only be explained by a combination of a linear and quadratic component of the Stark shift of the molecule. Even though the external electric field is switched off, the molecule exhibits a non-zero Stark shift, at position α in Fig. 6.2 (b). As seen in section 2.2, the molecule can have a Stark shift due to an internal field $\vec{E}_{int}$ (see Eq. (2.20)). Switching on the external electric field E_{ext}, results in an additional electric field component and the Stark shift changes towards higher frequencies to position β in Fig. 6.2 (b). Now, moving the tip away from the center position and reducing therefore the electric field at the position of the molecule results in an even larger shift of the ZPL. This would correspond to moving from position β to position γ in Fig. 6.2 (b), which results indeed in a larger Stark shift.

The assumption of a combination of a linear and quadratic component of the Stark shift is confirmed by a biased tip scan, shown in Fig. 6.2 (c). This figure shows the fluorescence intensity depending on tip position. Even though the molecule shows some blinking, a Stark-shift pattern can be observed. The circular pattern is not centered around the center of the tip scan. It is moved a bit to the upper right corner which is corner2. Furthermore, the pattern seems to have a more elliptical shape, which confirms a dominant quadratic component of the Stark shift as discussed in Chap. 4.3. The Stark-shift pattern is cut off at the corner, because of an unfortunate setting of the detuning $\Delta\tilde{\nu}$. The excitation frequency for this tip scan has been set to $\nu_L = 140$ MHz, which results in an detuning of $\Delta\tilde{\nu} = 12$ MHz. The maximum Stark shift is $\Delta\nu = 293$ MHz. From the theoretical discussion we known, that for imaging a complete Stark-shift pattern, the detuning $\Delta\tilde{\nu}$ and the Stark shift $\Delta\nu$ should have more or less the same value (see Eq. (5.1)). The molecule bleached before the laser frequency could be adjusted to a higher value to observe a complete Stark-shift pattern.

6.4   Stark-shift pattern depending on tip voltage

The theoretical model in Chapter 4 predicts that with an increasing tip-voltage, the diameter and the width of the Stark-shift patterns should increase (see Fig. 5.3). In Fig. 6.3 a series of circular Stark-shift patterns of a single molecule is shown for different values of tip voltages. From Fig. 6.3 (a) to (e) the voltage is increased in
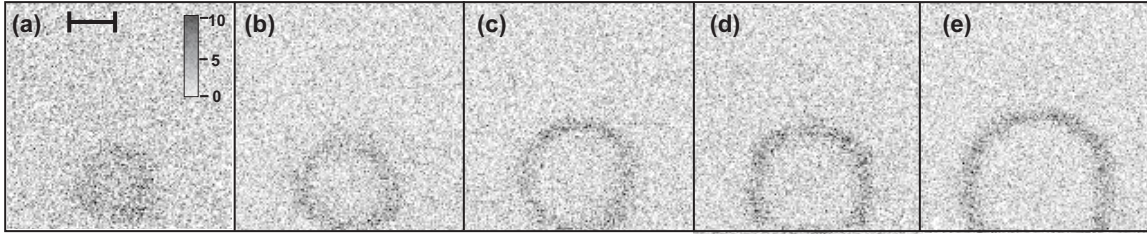
Figure 6.3: Voltage dependence of the Stark-shift ring taken with a laser power of $= 13$ nW. The gap-width is in the μm-range. The scalebar is 1μm and the grey-scale is in counts. (a) $U = -80$ V (b) $U = -90$ V (c) $U = -100$ V (d) $U = -110$ V (e) $U = -120$ V

	(a)	(b)	(c)	(d)	(e)
	$U = -80$ V	$U = -90$ V	$U = -100$ V	$U = -110$ V	$U = -120$ V
W [μm]	0.59±0.04	0.30±0.02	0.29±0.01	0.29±0.01	0.27±0.01
D [μm]	1.18±0.03	1.94±0.02	2.25±0.01	2.45±0.01	3.06±0.01

Table 6.2: Overview of the fit-results for the ring width W and the diameter D from the Stark-shift pattern depending on the applied voltage, shown in Fig. 6.3.

10V-steps from $U = -80$ V to $U = -120$ V. The sample consists of spin-coated micro-crystals. The excitation power of the laser is about ~ 13 nW. The gap-width is again estimated to be in the μm-range. Since the Stark-shift patterns are circular, it is assumed that the molecule exhibits a dominant linear Stark-shift component. Unfortunately, this assumption cannot be enforced by the experiment, since a five-points measurement has not been saved. The results of fitting the Stark-shift pattern with Eq. 6.3 are summarized in Table 6.2. The experimental results for the diameter follow the predicted behavior quite nicely. The dependence of the parameter W and D is plotted as a function of the tip voltage in Fig. 6.4. Increasing the voltage
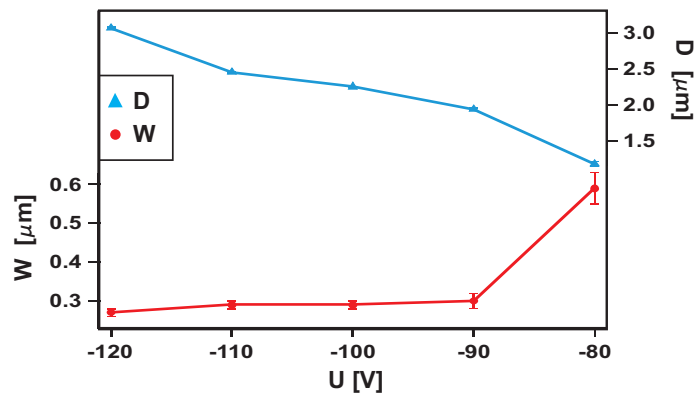

Figure 6.4: Dependence of the diameter D and the width W on the voltage as shown in Tab. 6.2.
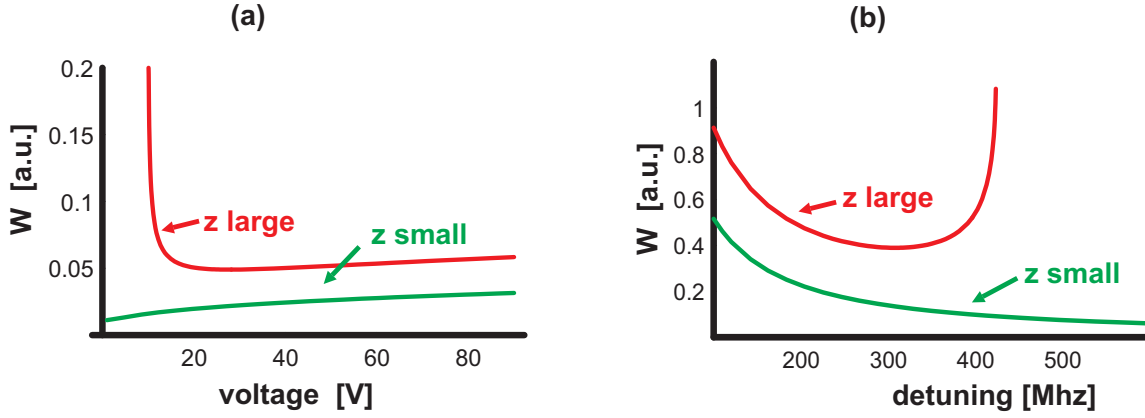
Figure 6.5: Explanation for the detected behavior of the width of the Stark-shift rings.(a) Influence of the applied voltage on the width at two different gap-width z. (b) Influence of the detuning $\Delta\tilde{\nu}$ on the width at two different gap-width z.

results in an increase of the diameter of the Stark-shift ring, while the width of the diameter decreases from $W = 0.59$ μm to $W = 0.27$ μm. The decrease of W seems to contradict the theoretical model, since an increase of the width is expected with increasing voltage. Taking a closer look at Fig. 5.3 (b) reveals, that two different types of behavior of the ring width depending on the gap-width z are expected. In Fig.Fig. 6.5 (a), the ring width W is plotted as a function of the applied voltage. The upper graph is for large gap-width ($z > 2$ μm) and the lower one is for small gap-width ($z < 2$ μm). At large gap-width z, it is possible that the width W of the Stark-shift rings first decreases and then increases by continuously increasing the voltage. Reaching a certain critical gap-width z, the behavior of the width W switches to an continuous increase with increasing voltage. The actual value for the gap-width z, at which the behavior of the ring width W switches, depends on the detuning $\Delta\tilde{\nu}$. At large gap-width z, increasing the voltage results in a sharp decrease of the ring width and afterwards in a slight decrease. At small gap-width, the increase in voltage results in a continuously increase of the width of the Stark-shift rings.

The experimentally observed behavior of the diameter D and the width W depending on the tip voltage follow the predictions of the theoretical model very well. The influence of the tip voltage is therefore understood and can be used to control the Stark-shift pattern of single molecules. By changing the voltage a rough estimation of the tip-molecule distance is obtained, depending on the behavior of the ring width W as shown in Fig. 6.5 (a).

tip	center	corner1	corner2	corner3	corner4
Γ [MHz]	119±5.2	68.2±2	84.2±2.1	65±2.4	56.6±2.9
A [counts]	86.5±2.9	145.9±2.7	113.8±1.9	155.1±7.2	162±10.5
ν_i [GHz]	0.8±0.001	1.28±0.001	1.39±0.0007	1.17±0.0007	1.33±0.0004

Table 6.3: Overview of the fit parameter of the spectra depending on the tip-position in Fig. 6.6 (a). The frequency ν_i is the spectral position of the ZPL at the different tip position ($i = c, 1, 2, 3, 4$).

6.5 Stark-shift pattern depending on the excitation frequency

The theoretical model predicts, that with an increasing detuning, the width of the Stark-shift ring and also the diameter decreases, see Fig. 5.2. Stark-shift data depending on the detuning $\Delta\tilde{\nu}$ are shown in Fig. 6.6. They are recorded with a sublimated crystal. The laser power is set to $P \sim 20$ nW and the tip voltage is set to $U = 28$V. The Stark-shift depending on tip position is shown in the first row, Fig 6.6 (a). The tip is moved from the center position (first spectrum), to the four corners (following four spectra). The fit parameter of the spectra are summarized in Table 6.3. By comparing the line width Γ at the different tip positions in table 6.3, we notice that the line width Γ is broadened and the amplitude A is decreased, when the tip is in the center position, which is the closest position to the molecule. The Stark-shift depending on the tip position in its scan range varies between $\nu' = 370$ MHz at corner3 and $\nu' = 590$ MHz at corner2. Unfortunately, the zero-field resonance ν_0 has not been measured. Therefore, an absolute number for the Stark shift $\Delta\nu$ depending on tip position cannot be extracted. By analysis of the Stark-shift ring depending on excitation frequency, we will see that the zero-field resonance ν_0 is spectrally located on the right side of the Stark-shifted resonances.

The shape of the Stark-shift patterns, Fig. 6.6 (b)-(m), is obviously elliptic, which points towards a dominant quadratic component of the Stark shift. In the middle row, Fig. 6.6 (b)-(g), the laser frequency ν_L is changed from 1 GHz to 500 MHz. Since the Stark-shift patterns decrease in size with the laser frequency going to lower frequencies, it can be deduced that the detuning $\Delta\tilde{\nu}$ must have increased. Therefore, the zero-field resonance ν_0 lies at higher frequencies than any of the resonance at the corner positions: $\nu_0 > 1.39$ GHz. In Fig. 6.6 (e), a full Stark-shift ring is visible. The detuning $\Delta\tilde{\nu}$ must be close to the best setting, where $\Delta\tilde{\nu} \simeq \Delta\nu$. From this, it can be even deduced, that $\nu_0 \sim 1.45$ GHz. The Stark-shift pattern is decreasing in size with an increasing detuning, until the shape is reduced to a spot (Fig. 6.6 (f)). At this point, the detuning is chosen in such a way, that no elliptical Stark-shift pattern is observed anymore (see Eq. (5.4)).
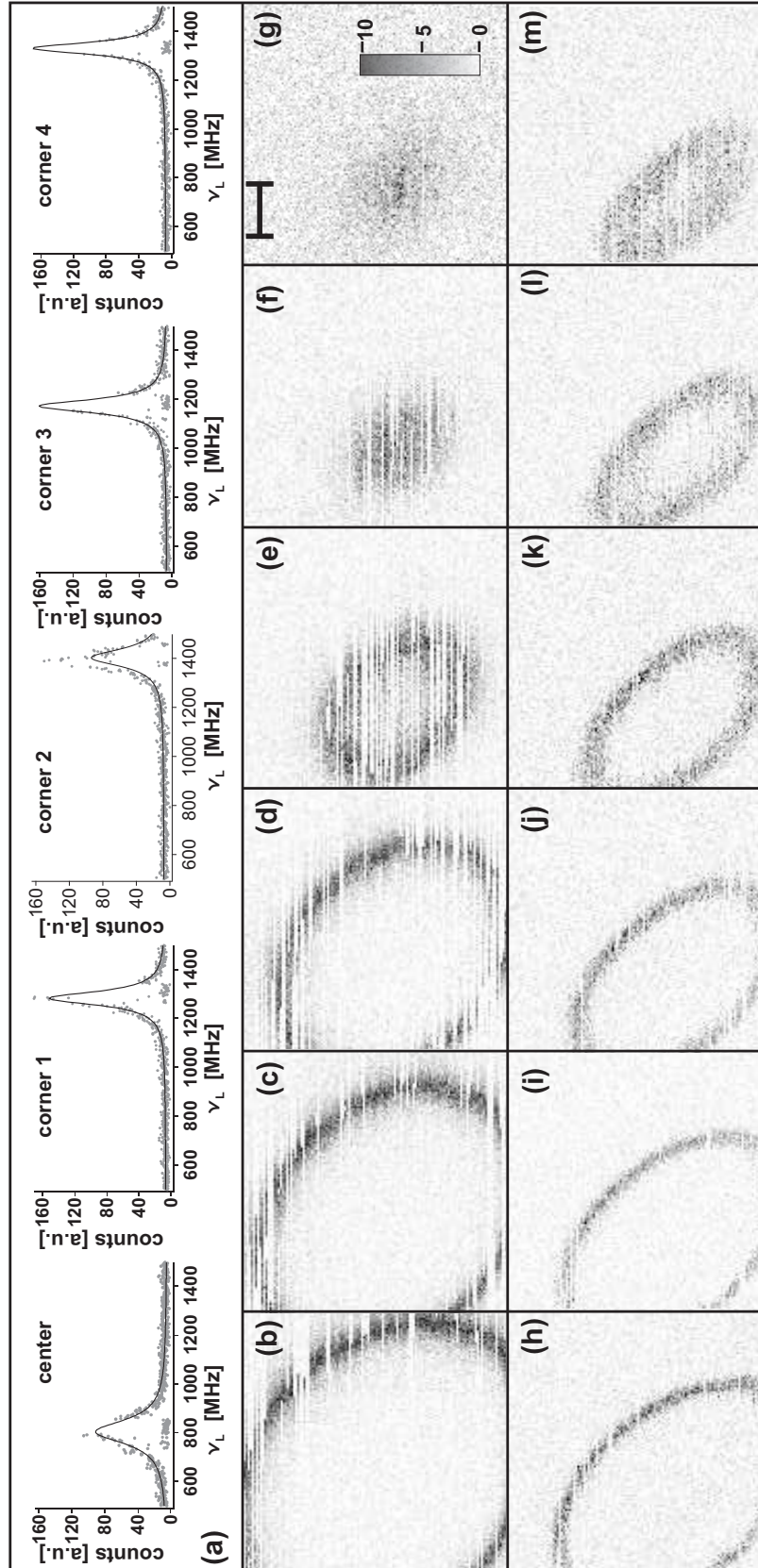
Figure 6.6: (a) Stark shift depending on tip position, at the center position and the four corners. Laser power $P \sim 20$ nW, tip voltage $U = 28$ V. (b)-(g) Stark-shift patterns depending on the excitation frequency: $\nu_L = 1.1$ GHz (b), $\nu_L = 1$ GHz (c), $\nu_L = 0.9$ GHz (d), $\nu_L = 0.7$ GHz (e), $\nu_L = 0.6$ GHz (f), $\nu_L = 0.5$ GHz (g). (h)-(m) Stark-shift patterns depending on the excitation frequency after tip approach: $\nu_L = 0.7$ GHz (h), $\nu_L = 0.55$ GHz (i), $\nu_L = 0.25$ GHz (j), $\nu_L = 0$ GHz (k), $\nu_L = -0.2$ GHz (l), $\nu_L = -0.4$ GHz (m).

ν_L [GHz]	$\tilde{a}$ [μm]	$\tilde{b}$ [μm]	y_0 [μm]	x_0 [μm]
1.1	3.35±0.006	2.26±0.003	2.21±0.004	1.72±0.005
1	2.86±0.004	2.14±0.003	2.19±0.003	1.7±0.005
0.9	2.45±0.005	1.83±0.004	2.13±0.004	1.66±0.004
0.7	1.33±0.009	0.96±0.006	2.15±0.006	1.64±0.006
0.7	2.67±0.004	1.63±0.001	1.76±0.003	1.37±0.003
0.55	2.46±0.004	1.50±0.002	1.76±0.002	1.36±0.003
0.25	2.24±0.004	1.27±0.002	1.74±0.003	1.35±0.004
0	1.94±0.005	1.02±0.002	1.74±0.003	1.34±0.003
-0.2	1.68±0.008	0.82±0.004	1.74±0.005	1.35±0.005
-0.4	1.17±0.012	0.59±0.006	1.75±0.007	1.36±0.007

Table 6.4: Results of the elliptical fits of the Stark-shift pattern in Fig. 6.6 (b)-(m) with the Eq. (6.7) and (6.7). The double line indicates the point of the tip approach.

The gap-width z is reduced by a few steps of the slip-stick drive. A new series of Stark-shift patterns is taken, Fig. 6.6 (h)-(m) by further decreasing the laser frequency ν_L from 0.7 GHz to -0.4 GHz. The same behavior of the size of the Stark-shift pattern is observed as in the images (b)-(g). By increasing the detuning, the size becomes smaller. The table 6.4 summarizes the fit-results according Eq. (6.6) and (6.7). It is clearly visible, that the minor and major axis becomes smaller, when the detuning increases. The angle ϕ is about 0.812 ± 0.006, which is about $\pi/4 = 45°$. The position of the molecule (x_0, y_0) is a bit shifted after the tip approach. During the image series Fig. 6.6 (b)-(g), the position of the molecule is $(\bar{x}_0, \bar{y}_0) = (1.68 \pm 0.005, 2.17 \pm 0.004)$ μm. After the tip approach, Fig. 6.6 (h)-(m), the position of the molecule is $(\bar{x}_0, \bar{y}_0) = (1.35 \pm 0.004, 1.75 \pm 0.004)$ μm. The approach by slip-stick motion is not perfectly vertical.

The striking feature in both data series is the contradicting behavior of the ring width. The expectation is, that with increasing detuning $\Delta\tilde{\nu}$, the diameter D and the ring width W, respectively, decrease. Contradicting, the width W increases obviously with increasing detuning. The origin of such a behavior can be explained by the help of Fig. 6.5 (b). The width of the Stark-shift ring shows different behavior due to changes of the detuning. At large gap-width z (upper graph), an increase in the detuning is followed by a decrease and then by an increase in the diameter W. Only at smaller gap-width, the increase of the detuning is followed by a continuously decreasing width of the Stark-shift ring. From this discussion on the behavior of the ring width W we may deduce, that (i) the gap-width z in that measurement is comparable large ($z > 1$ μm, depending on the voltage), and (ii) the detuning $\Delta\tilde{\nu}$ is also large ($\Delta\tilde{\nu} > 400$ MHz), depending on the gap-width z and the voltage). Generally,

the ring width W depends much stronger on the detuning $\Delta\tilde{\nu}$ than on the voltage, as shown in Fig. 6.5.

Comparing the images from Fig. 6.6 (b)-(g) with the images from Fig. 6.6 (h)-(m), we observe that the ring width W and the size of the Stark-shift pattern depend also very strongly on the gap-width z. By reducing the gap-width, the ring width becomes much smaller, Fig. 6.6 (h). As mentioned in the introduction, the ring width depends strongly on the electric field gradient at the tip. Approaching the tip results in an increase of the field gradient. The size of the Stark-shift pattern is increased, as long as the gap-width is more than approximately 1 μm (also depending on voltage and detuning). The effect has been explained in section 4.3 and will be also discussed in the following experimental section.

The experimental results depending on the detuning $\Delta\tilde{\nu}$ can be explained with the help of the theoretical model, and the influence of the detuning on the Stark-shift pattern is by now understood. By changing the detuning a rough estimation of the tip-molecule distance is obtained, depending on the behavior of the ring width W as shown in Fig. 6.5 (b).

6.6   Stark-shift pattern depending on the gap-width

In Fig. 6.7 a series of Stark-shift pattern of a single molecule are presented. The data are recorded with a sublimated crystal. The laser power is 30 nW. Fig. 6.7 (a) shows the resonance of the singe molecule, with the voltage already switched on. The line width is $\Gamma = 44$ MHz and the resonance is $\nu = -5.31$ GHz.   Fig. 6.7 (b)-(f) shows a series of Stark-shift pattern, where the excitation frequency has been changed. The excitation frequency has been increased from $\nu_L = -5.3$ GHz (Fig. 6.7 (b)) to $\nu_L = -5.55$ GHz (Fig. 6.7 (f)). The effect on the change of the excitation frequency is a decrease in diameter and in the width of the observed Stark-shift patterns. This tendency again is supported by the theoretical prediction. In Fig. 6.7 (c), the Stark-shift pattern appears to have an asymmetric shape. We suspect that due to a slow spectral 'creeping' of the ZPL, the Stark-shift pattern does not show a perfect circular structure. The feature in Fig. 6.7 (c) may be reproduced by four segments from four different rings. The first ring starts at the bottom up to the dashed line 1, where the first spectral jump of the molecule occurs. The diameter of the Stark-shift ring changes slightly. Then a second spectral jump of the molecule occurs and the diameter and the width of the Stark-shift ring are slightly decreased (marked by the dashed line 2). The third ring goes from the dashed line 2 to the dashed line 3, where the third spectral jump occurs. Due to the spectral jumps of the resonance, the detuning $\Delta\tilde{\nu}$ is not constant during the tip scan. A change in the detuning explains the difference in diameter and the width of the Stark-shift ring during the tip scan. In Fig. 6.7 (d)-(f) three images are shown , where the resonance of the molecule is stable
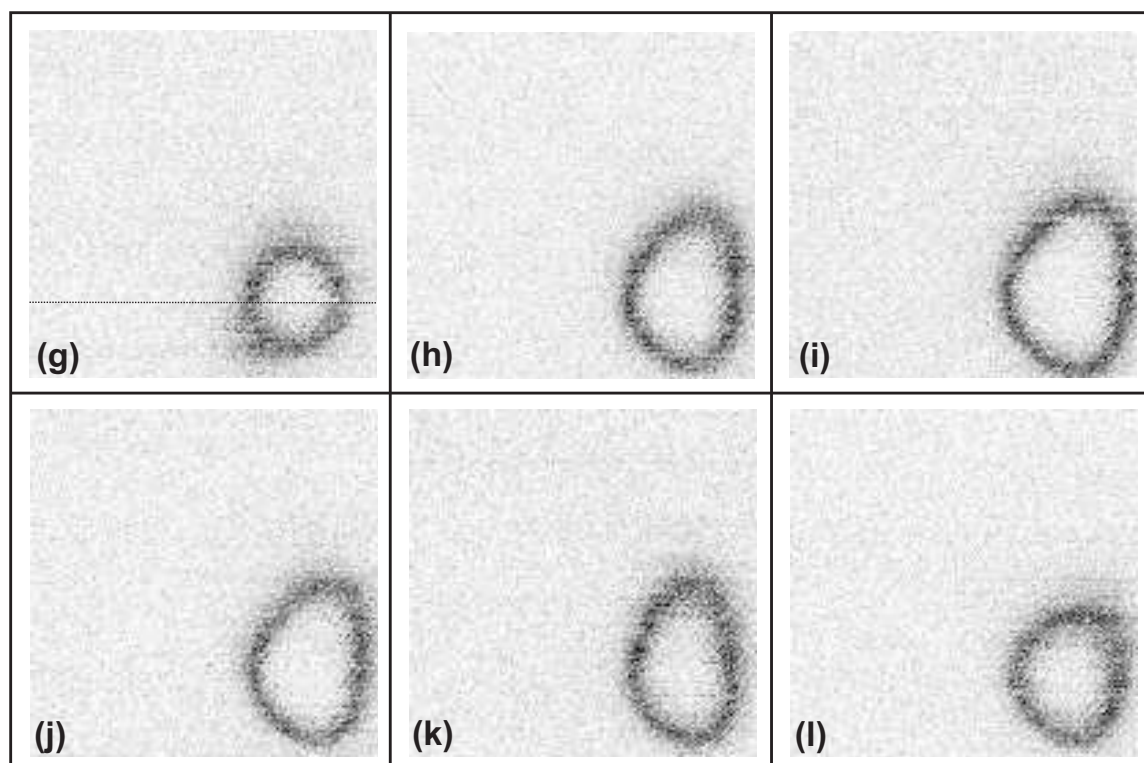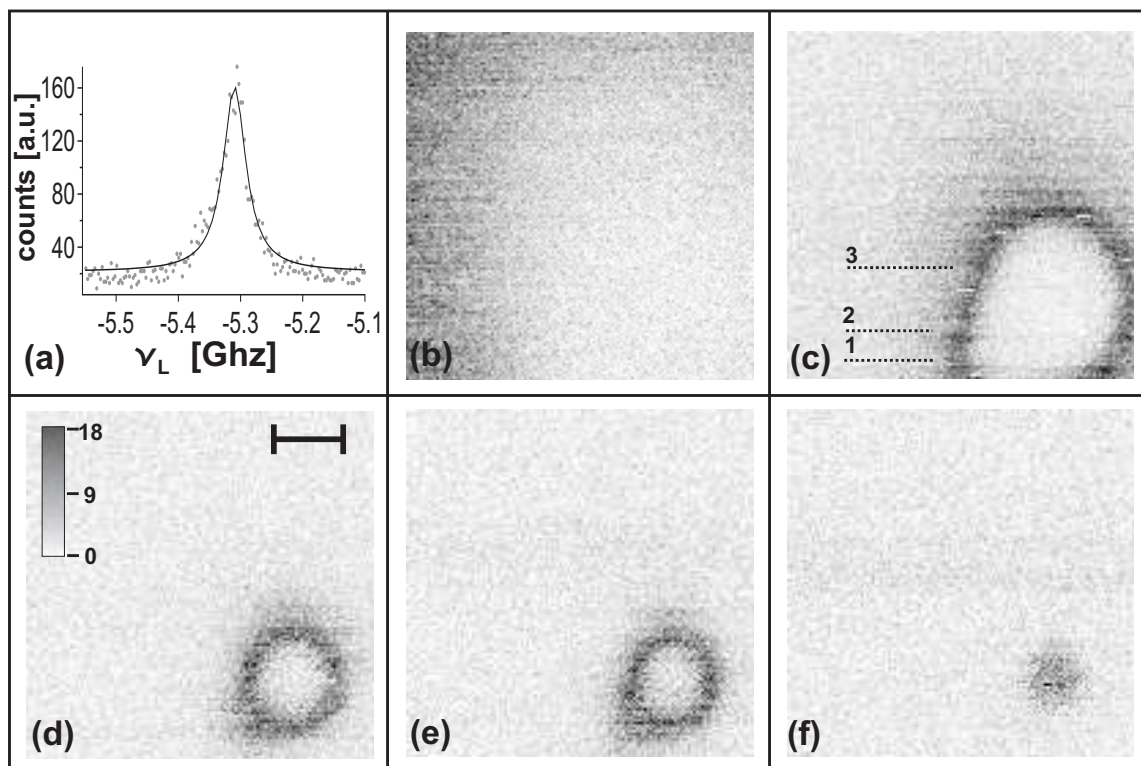
Figure 6.7: (a) Spectrum of a single molecule with a line width of $\Gamma = 44$ MHz, taken with an laser power of 30 nW. (b)-(f) Stark-shift patterns depending on the excitation frequency. Tip voltage is $U = 140$V, scalebar is 1μm and the grey-scale is in counts. (b) $\nu_L = -5.3$ GHz, (c) $\nu_L = -5.34$ GHz, (d) $\nu_L = -5.4$ GHz, (e) $\nu_L = -5.48$ GHz, (f) $\nu_L = -5.56$ GHz. (g)-(l) Series of Stark-shift patterns depending on the gap-width. Excitation frequency is $\nu_L = -5.4$ GHz and the tip voltage is $U = 140$ V. The tip has been approached to the sample, the gap-width decreases from (g) to (l).
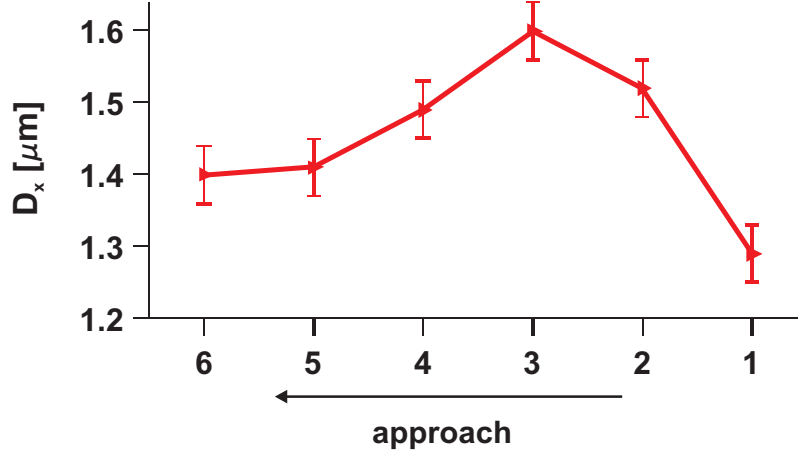
Figure 6.8: Dependence of the diameter D_x on the gap-width z.

again, and the Stark-shift patterns are circular. The round Stark-shift pattern leads to the conclusion, that the single molecule exhibits a dominant linear Stark shift and the dipole moment difference $\Delta\mu$ is oriented perpendicular to the surface.

Fig. 6.7 (g)-(l) shows a series of Stark-shift patterns of the same molecule depending on the gap-width z. The tip voltage is kept fixed at $U = 140$ V and the excitation frequency is set to $\nu_L = -5.4$ GHz. Starting in Fig. 6.7 (g) the gap-width is decreased. Since shear-force control has not been operating, the absolute value for the gap-width is not known. During the approach, the molecule shows further spectral instabilities. The Stark-shift patterns are not perfectly round. Therefore, it is difficult to quantitatively analyze the Stark-shift patterns. The center of the first Stark-shift ring (Fig. 6.7 (g)) is determined. In the further images (Fig. 6.7 (h)-(l)) the lower and the upper part of the circular pattern are deformed due to spectral instabilities. The diameter in x-direction of these Stark-shifts rings is taken at the center position of the first ring. The position is $y_0 = 1.09$ μm as indicated by the dashed line in Fig. 6.7 (g). The diameter D_x changes in the following way: $1.29 \pm 0.039 \mu$m $\rightarrow$ $1.52 \pm 0.039 \mu$m $\rightarrow$ $1.6 \pm 0.039 \mu$m $\rightarrow$ $1.49 \pm 0.039 \mu$m $\rightarrow$ $1.41 \pm 0.039 \mu$m $\rightarrow$ $1.4 \pm 0.039 \mu$m
The change of the diameter D_x depending on the gap-width z is very clearly visible in Fig. 6.8. The diameter D_x at the position $y_0 = 1.09$ μm increases up to 1.6 μm and then it decreases to 1.4μm. This trend confirms the theoretically predicted behavior of the Stark-shift ring upon decreasing of the gap-width z. Unfortunately, there are not enough data points in one line-section at $y_0 = 1.09 \mu$m to determine the width W of the Stark-shift rings accurately enough. The width does not seem to change very much during the approach. However, the data set confirms the predicted approach behavior shown in Fig. 4.3.

Another data set of a single molecule in a sample of spin-coated micro-crystals is shown in Fig. 6.9 and in Fig. 6.10. The laser power is $P = 7$ nW. The line
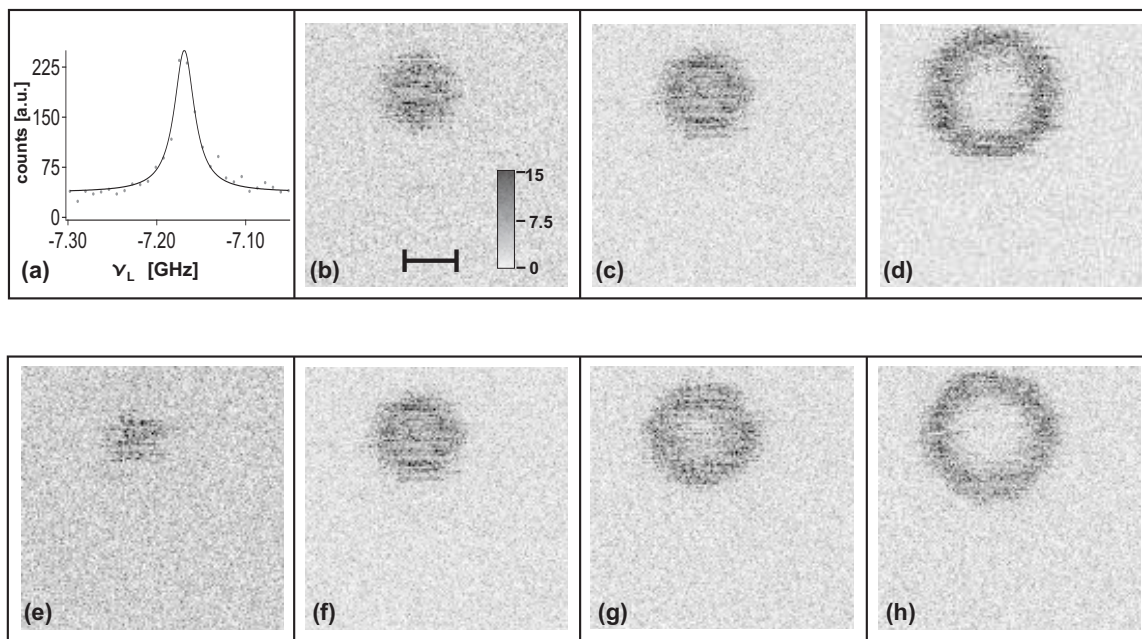
Figure 6.9: (a) Spectrum of a single molecule with a line width of $\Gamma = 26$ MHz, taken with an laser power of 7 nW. (b)-(d) Stark-shift patterns depending on the excitation frequency. (b) $\nu_L = -7.5$ GHz, (c) $\nu_L = -7.425$ GHz, (d) $\nu_L = -7.35$ GHz. (e)-(h)Stark-shift patterns depending on the tip voltage, which is increased from left to right. (e) $U = -60$V ,(f) $U = -70$V ,(g) $U = -80$V,(h) $U = -90$V. Scale bar is 1 μm, the greyscale is in counts.
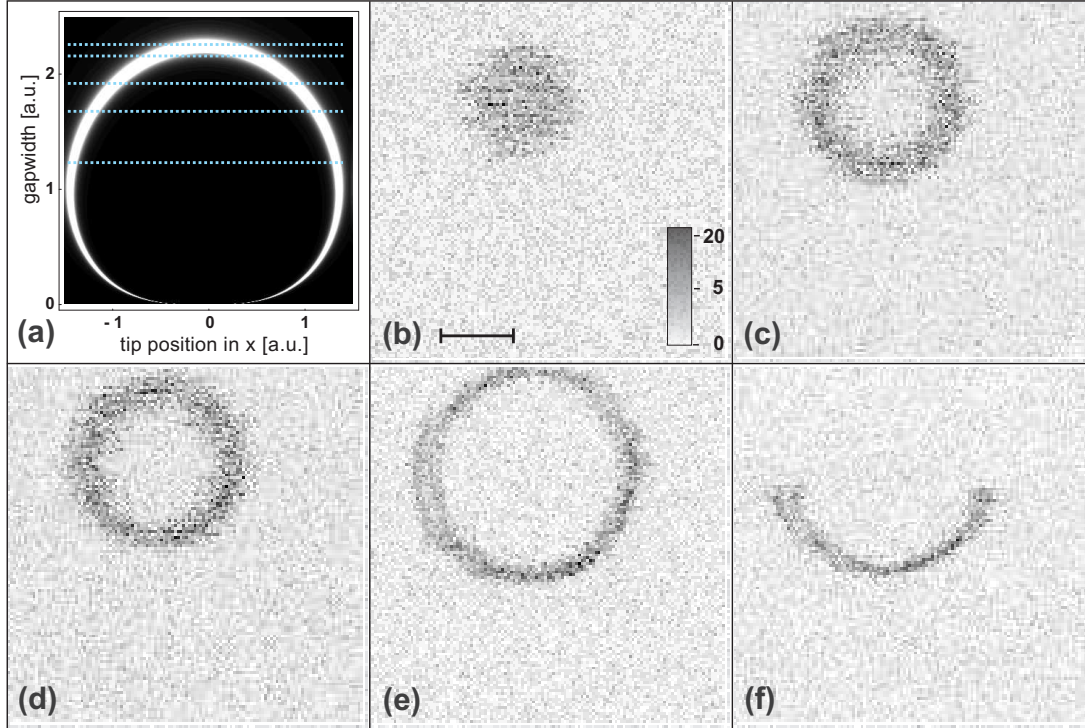
Figure 6.10: a) Vertical section along the z-axis at $y = 0$ of the calculated fluorescence of a single emitter depending on the tip position. The voltage and the detuning are kept constant. The 5 lines represent sections at different heights, where the experimental measurements have been taken. (b)-(f) Fluorescence depending on the tip position at different gap-widths. The scale bar is 1 μm, the greyscale is in counts.

width of the resonance in Fig. 6.9 (a) is $\Gamma = 26$ MHz and the zero-field resonance is $\nu_0 = -7.17$ GHz. The following images Fig. 6.9 (b)-(d) are taken at different excitation frequency at $\nu_L = -7.5$ GHz, $\nu_L = -7.425$ GHz and $\nu_L = -7.35$ GHz with a voltage of $U = -70$V. The detuning $\Delta\tilde{\nu}$ is therefore decreased from $\Delta\tilde{\nu} = 0.33$ GHz to $\Delta\tilde{\nu} = 0.18$ GHz. The diameter increases with decreasing detuning $\Delta\tilde{\nu}$, in accordance with the prediction. The lower row in Fig. 6.9, images (e)-(h), show the dependence of the Stark-shift patterns on the voltage. At an excitation frequency of $\nu_L = 7.425$ GHz, the voltage is increased, from $U = -60$ V, $U = -70$ V, $U = -80$ V to $U = -90$ V. The diameter D increases, which fits very well to the theoretical model. The determination of the width W is difficult, since only the last image shows a ring structure with a hole in the center. Even though, by visual inspection the width seems to increase with decreasing voltage.

Using the same molecule, another image-series is taken. Fig. 6.10 (b)-(f) diplays a series of Stark-shift patterns taken at a different gap-width z until in Fig. 6.10 (f), the molecule photo-bleaches. Reducing the gap-width results in an increase of the diameter D and a decrease of the width W of the circular Stark-shift pattern. This tendency confirms the theoretical model. A (x-z)-section of a numerically simulated
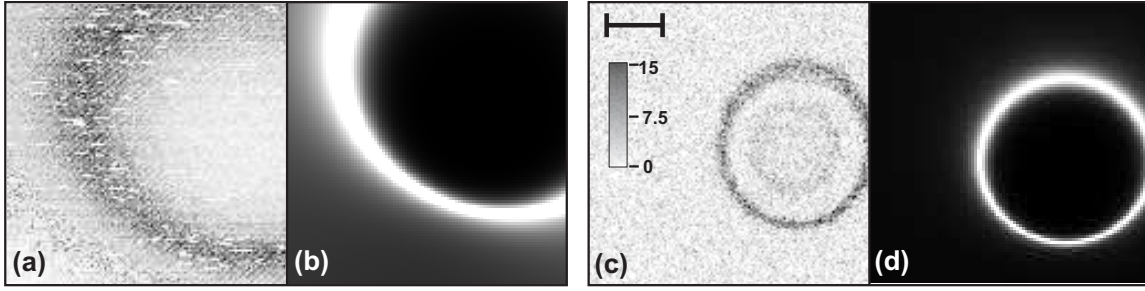
Figure 6.11: (a)Stark-shift pattern of a single molecule with a tilted permanent dipole difference. Laser power $P \sim 60$ nW , tip voltage $U = 59$ V and line width of the molecule $\Gamma = 45$ MHz. (b) Numerical simulation of the Stark-shift pattern (a) with a dipole $\Delta\mu$ tilted by $\theta = \frac{\pi}{10}$ and $\phi = \frac{2\pi}{5}$. (c) Another Stark-shift image of another single molecule with a tilted dipole difference. Laser power $P \sim 7$ nW , tip voltage $U = 80$ V and line width of the molecule $\Gamma = 26$ MHz. Scalebar is 1μm, and the greyscale is in counts. (d) Numerical simulation of the Stark-shift pattern (c) with a dipole $\Delta\mu$ tilted by $\theta = \frac{\pi}{10}$ and $\phi = \frac{\pi}{2}$.

Stark-shift pattern (see Chapter 4.3) is plotted in Fig. 6.10 (a) for comparison. The dashed lines mark the gap-width, at which the experimental Stark-shift pattern are taken. The experimental data fit nicely the predicted behavior as an increase in diameter and a decrease in ring width.

6.7   Stark-shift pattern depending on $\Delta\vec{\mu}$

The imaging of single molecules is not limited to the position determination or the discrimination between the linear and the quadratic component of the Stark shift. In Fig. 4.3 it is shown, that in the case of a dominant linear Stark shift, the orientation determination of the permanent dipole moment difference $\Delta\vec{\mu}$ is possible due to the width variation of the Stark-shift ring. Fig. 6.11 shows two examples of experimental measurements and their reproduction by the theoretical model. The orientation of the permanent dipole moment difference $\Delta\vec{\mu}$ is expressed in spherical coordinates:

$$\Delta\vec{\mu} = |\Delta\mu| \begin{pmatrix} \sin\phi\cos\theta \\ \sin\phi\sin\theta \\ \cos\phi \end{pmatrix}. \tag{6.8}$$

Here, θ is the angle between $\Delta\mu$ and the z-axis, and ϕ is the in-plane angle between $\Delta\mu$ and the x-axis. Fig. 6.11 (a) is a Stark-shift pattern obtained with a molecule embedded in a sublimated crystal. The voltage and the detuning are not optimized. The ring is very large in diameter and the width very broad. Laser power has been set to $P \sim 60$ nW and the tip voltage was $U = 59$ V. The line width of the molecule is $\Gamma = 45$ MHz. As can easily be observed the width of the Stark-shift ring increases on the upper half of the visible Stark-shift pattern. Such an asymmetry in the ring

width is an indication for a tilted permanent dipole difference $\Delta\mu$. In Fig. 6.11 (b), the experimental image has been reproduced by a numerical simulation using a dipole moment difference $\Delta\mu$ tilted by $\theta = \frac{\pi}{10}$ and $\phi = \frac{2\pi}{5}$.

Fig. 6.11 (c) shows a second example of a Stark-shift pattern of a single molecule, where a significant variation in the ring width W is visible. The upper part shows a clear broadening of the width W. The data are taken with a spin-coated micro-crystal. The laser power is $P = 7$ nW and voltage on the tip is $U = 80$ V. The line width of the resonance is $\Gamma = 26$ MHz. In Fig. 6.11 (d) the experimental image is reproduced by a numerical simulation using a dipole moment difference $\Delta\mu$ tilted by $\theta = \frac{\pi}{10}$ and $\phi = \frac{\pi}{2}$. The other striking feature in this Stark-shift image is the second Stark-shift ring in the center of the first ring. This second ring belongs to a second molecule with different spectral properties. Distinguishing the spatial positions of several molecules within a single tip scan will be discussed later on in section 6.9.

6.8 Stark-shift pattern: the interaction with a TLS

Stark-shift patterns exhibit interesting features. Taking a closer look at the images in Fig. 6.10 (e) and (f) reveals a splitting on the left side of the Stark-shift ring. The two images are shown again in Fig. 6.12 (a) and (b). The splitting is indicated by the two arrows. The splitting of Stark-shift pattern has been discussed theoretically in Chapter 4.4.2. There, the splitting of a Stark-shift ring is obtained modelling a single molecule coupled to a neighboring TLS in the matrix. The TLS is frozen in the lower state. At certain positions of the tip, a flipping of the TLS occurs. As discussed, such a flipping induces an additional shift of the molecules' resonance, which finally results in a splitting of the Stark-shift ring. A simulated image is shown in Fig. 6.12 (c). The simulated image shows a reasonable agreement with the experimental data. The same parameter estimations have been used as for the calculated images of the splitted Stark-shift ring, which are compared in the following with the experimental data. The dipole moment of the tunneling TLS is slightly tilted by $\phi = -\frac{\pi}{2}$ and the TLS is defined as:

$$
\begin{aligned}
\Delta_0 &= 0.31\,k_B T \\
\eta &= 0.096\,k_B T \\
(x)0, y_0) &= (0,0) \\
(x'_0, y'_0) &= (0.03, 0)\,\mu\text{m} \\
\alpha &= 120\,\text{MHz} \\
\Delta\tilde{\nu} &= 150\,\text{MHz}
\end{aligned}
$$

Taking line-cuts of the Stark-shift patterns gives a better indication of the splitting. Line-cuts through the center of the Stark-shift rings of the experimental data are averaged by 3 lines. In Fig. 6.13 line-cuts of the experimental and simulated Stark-
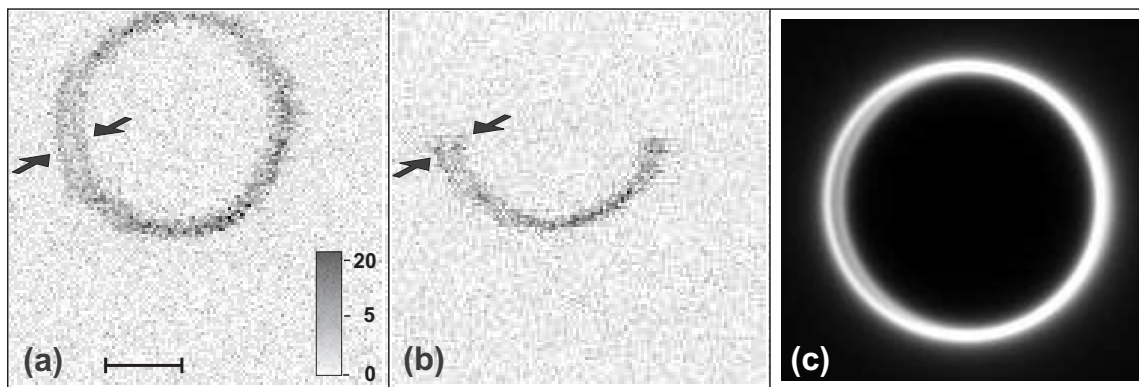
Figure 6.12: (a) and (b) are Stark-shift patterns of a single molecule where a splitting of the ring is visible as indicated by the arrows. Scalebar is 1 μm and the greyscale is in counts. (c) is a simulated Stark-shift pattern, where the splitting of the Stark-shift ring is reproduced by a coupling to a neighboring TLS (see Chapter 4.4.2).

shift rings at a large gap-width z are shown. No splitting of the Stark-shift pattern is visible. Fig. 6.13 (a) shows the line-cuts along the x-direction and Fig. 6.13 (b) shows the corresponding line-cut along the y-axis. Comparing the line-section of the experimental to the theoretical data, the model and the experimental measurement agree reasonable well, even though the peak height difference in the experimental data in Fig. 6.13 (a) is not as distinct as in the calculated line-section.

In Fig. 6.14, the line-sections of the experimental and the simulated data are shown for small gap-width. (a)-(c) show line-sections in the x-direction and (d) shows the line-cut in y-direction. The image and the line-section on the left side are the experimental data. The line-cuts are again averaged by 3 lines, since the data point in one section are quite low. The line-section and the image on the right side of Fig. 6.14 are the numerical simulated data. Fig. 6.14 (a) is a line-section directly through the area of the splitted Stark-shift ring. In the experimental line-cut, the peak on the left side is reduced in height and the peak is clearly splitted into two parts. The peak on the right side is clearly higher in amplitude. The simulated data on the right side can reproduce the difference in peak height and the splitting of the left peak. Even though, the splitting in the experimental data seems to be into two equal part in contrast to the simulated splitting, the simulated line-section nicely reproduces the feature of the experimental data. Finally, Fig. 6.14 (d) shows a line-section through the center of the Stark-shift ring in y-direction. The peak of both sides of the Stark-shift ring should not differ. Unfortunately, the Stark-shift ring in the experimental data is cut at the edge, thus the height of the right peak cannot really be determined. The comparison between experimental results and the theoretical simulation indicates, that the single molecule might be coupled to a neighboring TLS in the matrix.
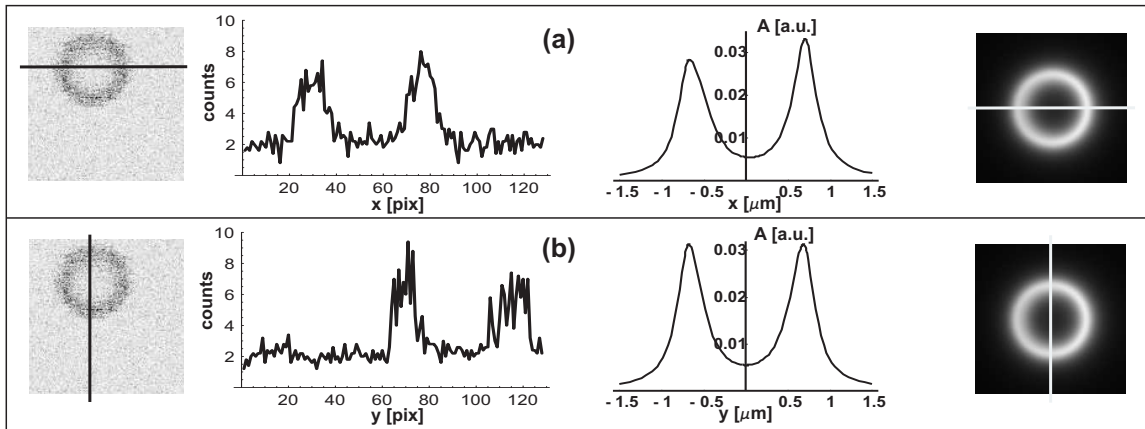
Figure 6.13: Line-sections of the experimental Stark-shift images (left side) and the simulated Stark-shift patterns (right side). The gap-width is large, no splitting of the Stark-shift pattern is visible. (a) section along the x-direction, (b) section along the y-direction.
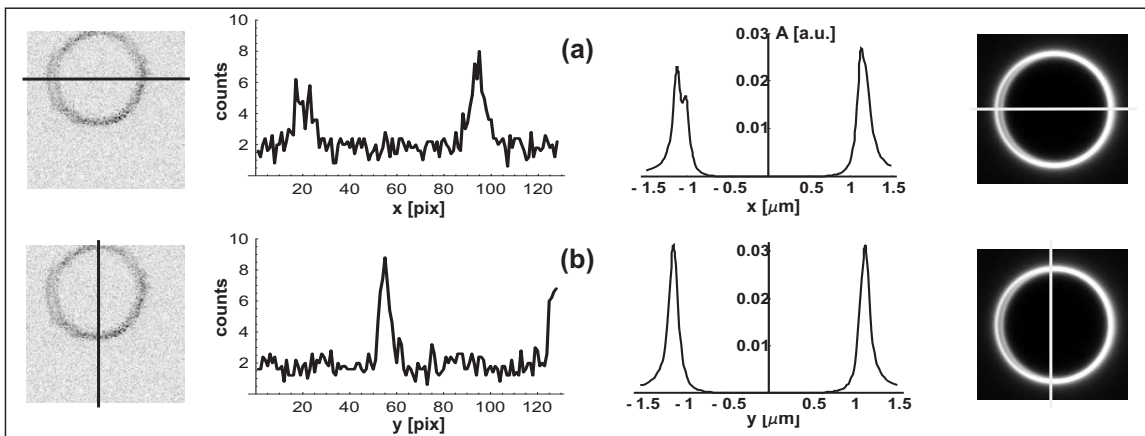

Figure 6.14: Line-sections at small gap-width, where the splitting appears. (a) Line-section in x-direction directly through the splitting. (b) Line-section in y-direction.
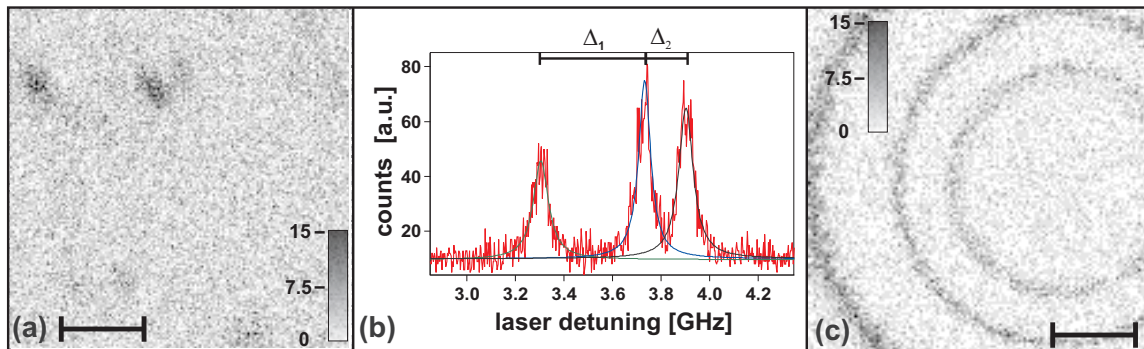
Figure 6.15: (a) Confocal image of a spin-coated micro-crystal at low temperature. (b) Spectrum where three molecules appear. Their line widths are between 30 and 38MHz and their spectral separation is $\Delta\nu_1 = 420$MHz and $\Delta\nu_2 = 170$MHz, respectively. (c) Stark-shift pattern, where the three molecules are resolved in a spatial tip scan. The scale-bar is 1 μm, the grey-scale is in counts.

6.9   Stark-shift pattern of several molecules

If more than one molecule is present in the focal volume, the positions of molecules and their respective distances can be determined with high accuracy taking advantage of the spectral information. Fig. 6.15 (a) shows a regular fixed-frequency confocal image of a sample containing several fluorescent spots. A typical frequency scan obtained in this sample area is shown in Fig. 6.15 (b). Three spectrally separated molecules are detected within the excitation volume. Their line widths are between 30 and 38 MHz and their spectral separation is $\Delta\nu_1 = 420$ MHz and $\Delta\nu_2 = 170$ MHz, respectively. By scanning the biased tip ($U = -180$ V) with an initially off-resonant laser frequency, the presence of three molecules is apparent in one spatial tip scan, see Fig. 6.15 (c). The data are taken on a spin-coated micro-crystal. The laser power is $P = 40$ nW.

A series of Stark-shift patterns has been taken at different gap-width z, which is shown in Fig. 6.16 (a)-(i). The gap-width is reduced from $z = 4.11 \pm 0.23$ μm to $z < 3.12 \pm 0.23$ μm. The Stark-shift patterns show at the beginning only two rings and a large spot in the center (see Fig. 6.15 (b)). During the approach of the tip, three circular structures appear, which correspond to three different molecules (see Fig. 6.15 (g)). Unfortunately, some spectral jumps of the molecules occur and new parameter settings have been necessary after image (i). The outer Stark-shift ring belongs to a very unstable molecule. The ring is interrupted frequently during the tip scan, except in image (g). The diameter and the width are not very stable during a scan either. These instabilities have quite a large impact on the other Stark-shift rings. As soon as the outer molecule shows a spectral activity such as a jump in the resonance frequency (equal to a jump in the diameter D), the inner two Stark-shift rings show also a jump. That behavior can be seen best in image (e), as indicated by the arrows. This fact leads to the conclusion, that the three molecules are coupled
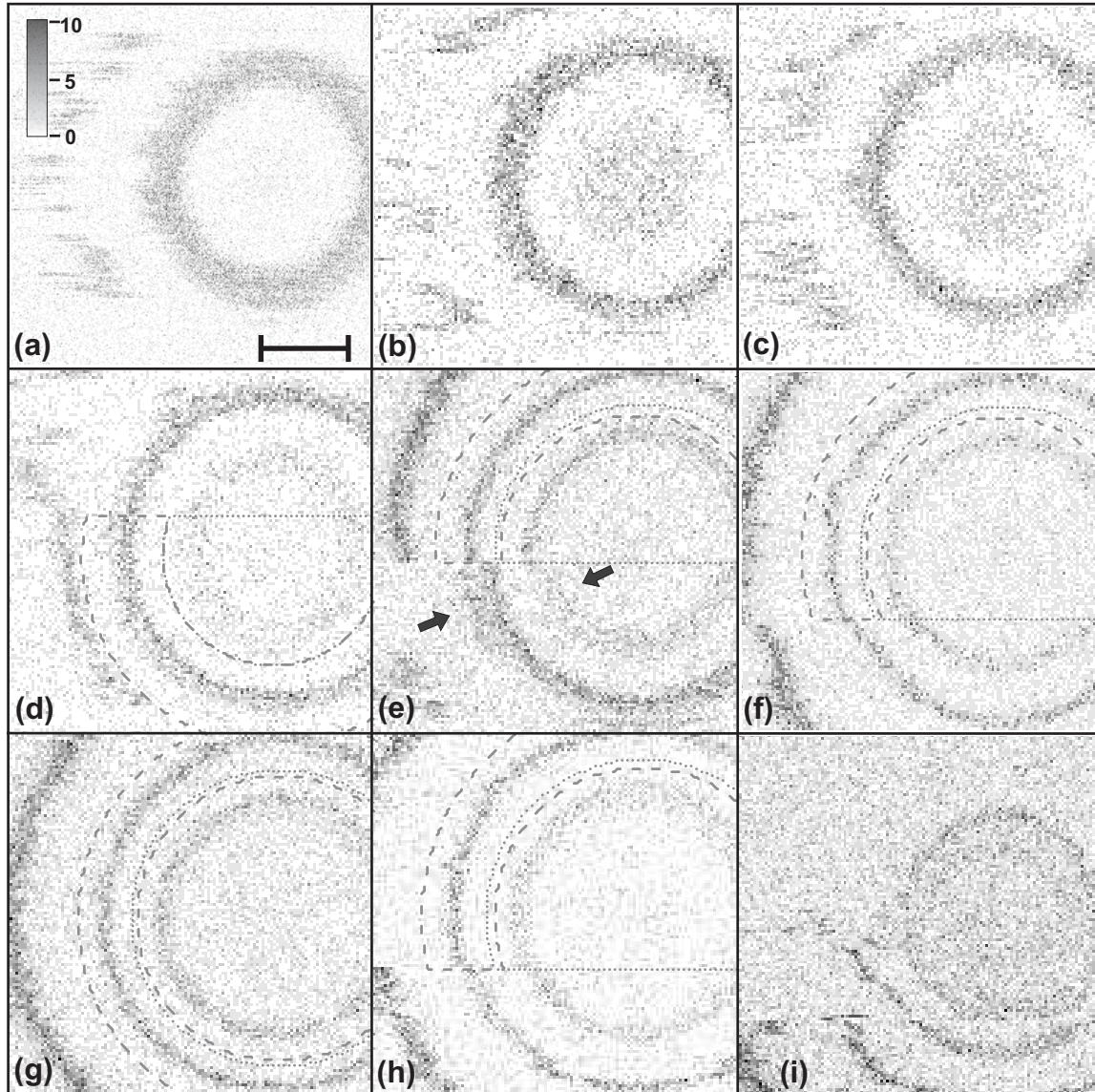
Figure 6.16: (a)-(i) Stark-shift patterns of the three molecules in the focus at different distances z, $z = 4.11 \pm 0.23$ μm (a), $z = 3.87 \pm 0.23$ μm (b), $z = 3.85 \pm 0.23$ μm (c), $z = 3.62 \pm 0.23$ μm (d),$z = 3.43 \pm 0.23$ μm (e),$z = 3.28 \pm 0.23$ μm (f),$z = 3.26 \pm 0.23$ μm (g),$z = 3.12 \pm 0.23$ μm (h), $z < 3.12 \pm 0.23$ μm (i) Scale bar is 1 μm, grey-scale is in counts. Fit-masks are outlined by a dashed line for the the outer ring, and a dotted line for the inner ring, respectively.

to each other or coupled over the same TLS in the matrix. Analyzing the data set, the fit-area has been restricted to areas where the molecules show a stable behavior. The fit-mask are outlined in Fig. 6.16 by a dashed line for the middle ring, and a dotted line for the inner ring. The outer, third Stark-shift ring could not be analyzed quantitatively, since it is too unstable.

Obtaining an estimate for the gap-width z is not an easy task since it is not measured directly. By using Eq. (5.5) and with an image-series with changing excitation frequencies, a value for the gap-width is obtained. In Fig. 6.17 (a)-(c), three Stark-shift images at $\nu_L = 4.58\text{GHz}$, $\nu_L = 4.965\text{GHz}$ and $\nu_L = 5.1\text{GHz}$ are shown. The voltage on the tip ($\sim b$) and the gap-width z is kept constant during all three scans, only the detuning $\Delta\tilde{\nu}$ is changed. Therefore, using Equation (5.5), the following formula can be deduced:

$$\delta\tilde{\nu}_{i,j} = \Delta\tilde{\nu}_i - \Delta\tilde{\nu}_j = bz \left[\frac{1}{((\frac{D_i}{2})^2 + z^2)^{3/2}} - \frac{1}{((\frac{D_j}{2})^2 + z^2)^{3/2}} \right], \qquad (6.9)$$

with $\Delta\tilde{\nu}_{i,j}$ the difference in the detuning for the image (i) and the image (j), respectively, with i,j=a,b or c, the factor b is proportional to the applied voltage to the tip, z is the distance molecule to tip and $D_{i,j}$ the diameter of the Stark-shift ring. The diameter D of the outer Stark-shift ring is used and can be derived by fitting the Stark-shift ring with Eq. 6.3. The value for $\delta\tilde{\nu}_{i,j}$ is known, since the change in laser frequency ν_L between the image (a) to (c) is known:

$$\delta\tilde{\nu}_{ab} = \Delta\tilde{\nu}_a - \Delta\tilde{\nu}_b \qquad (6.10)$$
$$= \nu_{La} - \nu_0 - \nu_{Lb} + \nu_0 \qquad (6.11)$$
$$= \nu_{La} - \nu_{Lb} \qquad (6.12)$$

where ν_{La} is the excitation frequency of image (a) and ν_{Lb} is the excitation frequency of image (b). This results in $\delta\tilde{\nu}_{a,b} = 0.27$ GHz. Following the same procedure for image (b) and image (c) results in a value for $\delta\tilde{\nu}_{bc} = 0.15$ GHz. Now, Eq. 6.9 is rearranged:

$$b = \frac{\delta\tilde{\nu}_{ij}}{z} \left[\frac{((\frac{D_i}{2})^2 + z^2)^{\frac{3}{2}} \left((\frac{D_j}{2})^2 + z^2\right)^{\frac{3}{2}}}{((\frac{D_i}{2})^2 + z^2)^{\frac{3}{2}} - \left((\frac{D_j}{2})^2 + z^2\right)^{\frac{3}{2}}} \right]. \qquad (6.13)$$

The only unknown parameter in this equation are b and the gap-width z, which have the same values for all image shown in Fig. 6.17 (a)-(c). By plotting b over z once for (i,j)=(a,b) and once (i,j)=(b,c) with $\Delta n_{b,c} = 0.15$ GHz results in the two graphs shown in Fig. 6.17 (d). The intersection yields the values for the unknown parameter: $b = 20965 \pm 700$ and $z = 105 \pm 0.49$ pix. The gap-width $z = 109 \; pix = 4.11 \; \mu$m is the start value for the approach series shown in Fig. 6.15.   With the obtained values for b and z, a value for $\Delta\tilde{\nu}$ can be obtained retrospectively by using Eq. 6.9: $n = 1.59$ GHz. Using Equation 5.5, a value for the gap-width z can be derived for
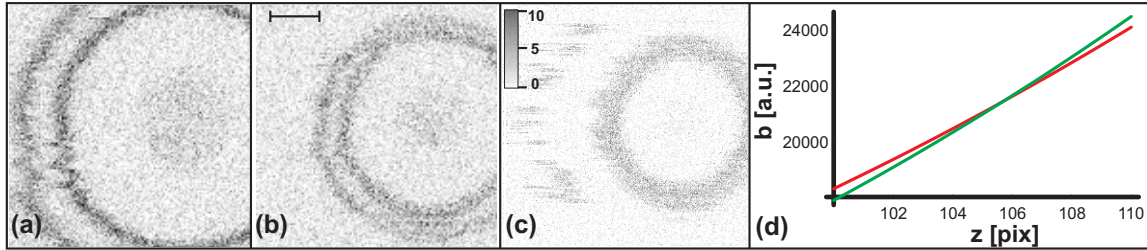
Figure 6.17: (a)-(d) Stark-shift patterns taken at different excitation frequencies, (a) $\nu_L = 4.58$ GHz, (b) $\nu_L = 4.965$ GHz, (c) $\nu_L = 5.1$ GHz. (d) Point of intersection for the two graphs, calculated with Equation (6.13).

Fig 6.16	(a)	(b)	(c)	(d)	(e)
D [μm]	2.91 ± 0.04	3.5 ± 0.04	3.68 ± 0.04	4.17 ± 0.04	4.52 ± 0.04
z [μm]	4.11 ± 0.23	3.87 ± 0.23	3.85 ± 0.23	3.62 ± 0.23	3.43 ± 0.23
Fig 6.16	(f)	(g)	(h)	(i)	
D [μm]	4.71 ± 0.04	4.75 ± 0.04	4.93 ± 0.04	> 4.93	
z [μm]	3.28 ± 0.23	3.26 ± 0.23	3.12 ± 0.23	< 3.12	

Table 6.5: Overview of the calculated gap-width z between the tip and the molecule of the middle of the three Stark-shift rings in Fig. 6.15 and the corresponding diameter D.

Figure 6.18: (a) The center coordinates depending on the gap-width z vary slightly during the approach. This can be assigned to technical reason. (b) Change of the diameter D depending on gap-width z. As predicted by the theoretical model, the diameter are increasing during the approach.

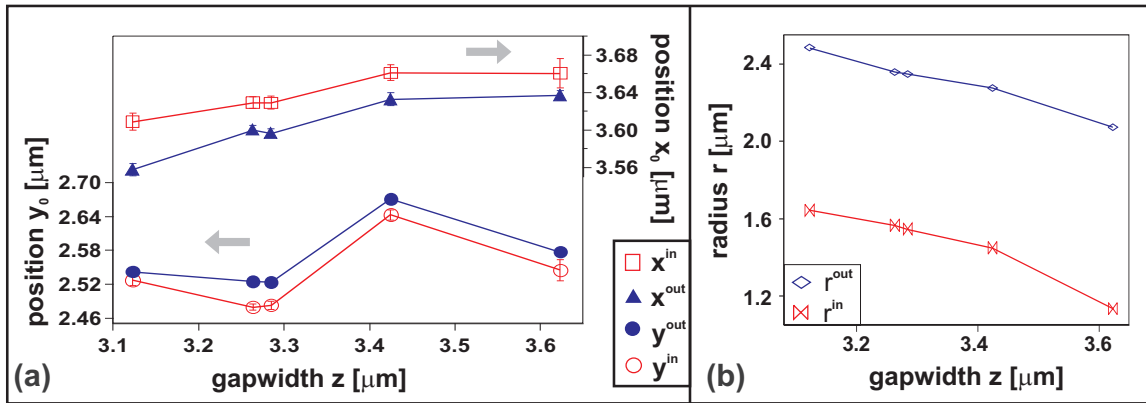every Stark-shift pattern, where the tip voltage and the detuning $\Delta\tilde{\nu} = 1.59$ GHz is kept constant. The obtained gap-width z is the distance between the tip and the molecule of the middle Stark-shift ring in Fig. 6.15. The gap-width for the other two molecule can be different, since the micro-crystal is up to 100 nm thick. The obtained gap-widths is summarized in table 6.5. The same table gives an overview of the change in diameter D of the middle Stark-shift ring in Fig. 6.15. The analysis of the Stark-shift ring has been restricted to the areas outlined by the dashed lines in Fig. 6.15.

The 2 inner rings, whose origins coincide with the molecules' positions, seem to be centered. However, careful analysis reveals that the 2 molecules are clearly separated by an average distance of $\bar{r} = \sqrt{\Delta x_0^2 + \Delta y_0^2} = 46 \pm 11$nm. The origins of the rings are obtained by nonlinear fitting of the rings according to Equation (6.3). The fits have been restricted to areas, where the outer molecule shows a stable spectral behavior, as indicated by the fit-masks in Fig. 6.16. The values for x_0 and y_0, presented in Fig. 6.18(a), vary during the approach. This is assigned to lateral jumps of the slip-stick drive which is used for the tip approach. Evidence for this explanation is the fact, that the values for both molecules shift parallel. Fig. 6.18 (b) shows the change in diameter over the gap-width z. Following the theoretical prediction, the diameter increases. As seen in Fig. 6.16, also the width of the Stark-shift rings increases, which can be reproduced by the theoretical model.

Chapter 7

Summary and outlook

In this thesis, a new technique, which we call Stark-shift microscopy, has been established for the the manipulation and the detection of single molecules and their optical properties. Stark-shift microscopy is performed combining fluorescence excitation spectroscopy for single-molecule detection and the perturbation of the molecular resonance by an externally controlled, inhomogeneous electric field of a sharp, metallized tip.

The available setup of a confocal microscope and a scanning-tip unit for low temperature application has been adapted for the use as Stark-shift microscope. Especially important has been the selection of a suitable tip, the realization of a reliable and good electrical contact to the tip and the establishment of a positioning control of the tip by optical observation. Two different preparation techniques of the sample system have been tried to optimize the properties of the sample for Stark-shift microscopy.

The experimental setup offers a large variety of control parameters for the field-molecule interaction. An experimental protocol has been elaborated to run and to control the imaging of single molecules by Stark-shift microscopy. The imaging protocol is based on operating experiences from the experimental measurements and is additionally reinforced by theoretical calculations.

A theoretical model for Stark-shift microscopy has been developed, which shade light on the interaction of the electric field of the tip with single molecules. The numerical calculation of Stark-shift patterns underlined the experimental results and contributed to their understanding. Depending on the orientation of the molecule and the Stark-shift coefficients ($\Delta\vec{\mu}$ and $\tilde{\alpha}$), the Stark-shift patterns show circular or elliptical features. The numerical calculations gave indications for further detectable effects, such as dipole-dipole coupling between molecules or the flipping of a TLS in the nearby environment. These effects are highly interesting to investigate and they can be made visible by Stark-shift microscopy.

Single molecules have been imaged by Stark-shift microscopy at cryogenic temperatures. Experimental measurements could be controlled by the tip voltage, by the detuning and the gap-width. The influence of the experimental parameter settings has been fully understood and could be controlled during the measurements. First indications of effects, such as the the orientation of the dipole moment difference and the coupling to a nearby TLS have been obtained. Several molecules, spectrally separated by 170 to 420 MHz, have been resolved in a single tip scan. Hereby, the tip has been scanned at a constant height of about 3 μm and the in-plane distance between the molecule has been determined to be $r = \sqrt{(x - x_0)^2 + (y - y_0)^2} = 46 \pm 11$ nm.

The experimental setup and control has been established. Further improvements of the experimental setup might be the implementation of a full-metal tip with a smaller apex for a stronger electric field gradient. Full-metal tips are also less fragile. For such a tip implementation, it is also necessary to develop a new mechanism for the tip positioning. Future work might be directed towards the demonstration of the simulated effects, such as the direct imaging of dipole-dipole interaction of single molecules. Stark-shift microscopy might be a very powerful tool for fascinating experiments to manipulate and tune the coupling or entanglement of single molecules [15, 98, 99, 100, 101].

Appendix A

Manual

This chapter gives a short overview of the setup preparation at room temperature and the cool down procedure. The overview can be used as a guideline for running the experimental setup.

A.1 Room temperature check

1. Motion of all piezoelectric elements
   The operation of the piezoelectric elements can be checked either by checking the resistance between the electrode and the cable connector or by observing the movements. A typical value for the resistance is around 1 Ω. Because of the thin electrodes, the resistance for the bimorph elements of the sample scanner are higher. Depending on the distance to the point of the electrical connection on the electrode, the resistance is between 35 to 60 Ω.

2. Electrical connection to the tip
   The electrical connection between the tip and the cable is tricky to check without breaking the tip. A small loop of a metal wire can be connected to the electrodes of a gauge to measure the resistance. The loop can be put around the higher end of the metallized glass-fiber tip and carefully pressed against it. Any reading of the gauge is fine.

3. Approach of the tip
   The approach of the tip is, due to the vertical slip-stick motion mechanism, susceptible to getting stuck. The surface of the sapphire balls and also the gliding surface of the tip holder has to be cleaned with ethanol.

4. Image of the tip in the focus
   The approach of the tip is controlled by observing laser light, coupled into the metallized glass-fiber tip, on a CCD camera. If the observed transmitted laser light is in the focus of the objective the approach is stopped. Since every tip produces a different laser spot at the end of the apex (depending on thickness and smoothness of the metal film), it is sometimes hard to tell, if the tip is

already in focus. A good check is, to focus onto the sample, then to remove the sample and approach the tip to the focus. The tip can be approach several times to get an idea of the expected image of the transmitted laser spot.

5. Objective

   The movement of the stepper motor for positioning the objective should be checked for a smooth operation. If it does not move smoothly, check the position of the tooth-wheel system and the resistance settings at the motor control box. The objective should be checked for any damage (scratches, cracks) of the lens and also for a clean surface.

6. Sample

   Check the distribution of the fluorescent signal over the sample. The distribution should be more or less homogeneous over the sample. Accumulation of dye molecules along grain boundaries gives problems at low temperature.

7. Thermometer readings

   It is very practical for the cool-down and warm-up procedure, to have thermometer. The reading of the thermometer should be checked several time (especially assembled with the protecting cup on top of the setup), to ensure a faultless reading.

A.2   Cool down procedure

The shielding vacuum chamber (number [3] in Fig. 3.15)should have a pressure of the order of $p \sim 10^{-6}$ mbar. The cool down procedure starts, after the full assembling of the setup inside the cryostat, with the evaporation of the setup chamber (number [1] in Fig. 3.15). After reaching a pressure of a few mbar, the chamber is flushed with helium gas. Now liquid nitrogen can be filled in the nitrogen shield (number [3] in Fig. 3.15). The nitrogen shield should be refilled at least two times and the pressure of the helium gas in the setup chamber should be kept close to 1 bar, to ensure a pre-cooling of the setup inside the cryostat. This process takes several hours and should be done over night (after the second refill). The over-night cooling results in a setup temperature of about 130 K. After the evacuation of the setup chamber, liquid helium can be transferred int the setup chamber. Since the cryostat on the optical table is higher than the helium dewar, the pressure on the helium dewar has to be high enough to guarantee a transfer. At the beginning, a pressure of about 1 to 1.5 psi on the liquid helium dewar gauge. After reaching the temperature of T$\sim$ 77 K, the pressure can be increased to 2 to 3 psi. The begin of collecting liquid helium is indicated by a sharp drop of the pressure. Now, the pressure on the liquid helium dewar can be increased a bit more to about 4 psi. If the reading of the liquid helium level meter reaches 40cm, the cryostat is full and the transfer can be stopped. Overall, the transfer of liquid helium takes about one hour. After pulling out the transfer line, the pumping on the liquid helium bath can started. Reaching the superfluid state

of the liquid helium can be observed by the backreflection of the laser light from the sample glass plate on the CCD camera. The signal goes over from a flickering, blurry spot to a clear image.

A.3 Cable connections

In Section 3.2.3, the different positioning possibilities accomplished by piezoelectric elements have been discussed. In this section, an overview of the electrical cable connection is given. Four electrical cables are guided from the main distributor box (see Fig. 3.14) to the cryogenic setup. One cable is for the stepper motor, the other three cables host the electrical connections to the piezo-electric elements. Each of the three cables is color-labelled (red, blue or yellow) and is connected by a 10-pin-connector. The following table gives an overview of the electrical connections of the piezo-electric elements and the thermometer. The connections are defined by the color-coding and the letter on the pin of the connector (female side which is connected to the top of the cryostat).

element	color coding	pin	signal
bimorph piezo (sample scanner)	yellow	B	HV_y
		D	HV_x
		E	GR
disk piezo (sample)	yellow	A	HV
		C	GR
voltage to the tip	yellow	K	voltage V
shear piezo (disk)	red	D	HV_x
		B	HV_y
		L	GR
shear piezo ($tip_{x,y}$)	red	E	HV_x
		A	HV_y
		K	GR
shear piezo (tip_z)	red	C	HV_z
		H	GR
tube piezo (tip scanner)	blue	A	HV_z
		D	HV_x^-
		F	HV_x^+
		B	HV_y^-
		E	HV_y^+
thermometer	blue	J,K	current I
		H,L	voltage V

Table A.1: Overview of the cable connections. HV is the high voltage signal from the corresponding amplifier and GR is ground. The index (x, y, z) indicates the different motion direction. The superscription $(+, -)$ for the tube piezo indicates the voltage sign for the opposite electrodes.

Appendix B

Troubleshooting

Technical problems at low temperature appear quite often, since the conditions are very demanding on the material and on the preparation. There are a few issues, which appeared more often during the experimental measurements and which are summarized in the following sections.

B.1 Technical problems

1. electrical connections and piezoelectric element
   If any piezoelectric element or the thermometer reading does not work anymore, gives a strange sound or a wrong reading, the first thing to check are the cable connections. First of all, check if everything is plugged in. If everything looks OK, check, if the electrical driving signal on the piezoelectric element looks OK. Especially in the case of the shear-piezos, the saw-tooth booster did not deliver a nice signal from time to time (burned out resistance). If the signal of the driven high voltage amplifier looks fine and arrives at the piezo-element (check directly on the piezo electrode!), problems with the electronics and broken cables can be excluded. In that case, the piezo-element might be broken. That cannot be easily checked. Only the movement of the bimorph-piezos can be checked with a piece of millimeter-paper and a lamp from above. The bending can be seen in the shadow. In the case of the shear-piezos, it has to be checked, if the sapphire ball is still attached to the surface. From time to time, the electrode becomes loose and the sapphire ball does not move with the piezo anymore. The shear-piezos give also a very high-pitched sound, if they are driven with a large amplitude. If that sound is missing, the shear piezos might have a problem with the polarization. The replacement of the piezo-element is the last solution in any kind of trouble with undefined reason.

2. objective
   For positioning of the objective, a stepper motor is used which is suitable for operation in low temperature and under vacuum. One problem was from time to time, that the objective did not move anymore. At room temperature, the

movement of the objective can be easily checked, by marking the rim of the objective and then observing the mark by switching on the motor and checking if the objective is turning. If the objective does not turn, check, if the control box of the motor is switched on and if all the cable connections are plugged together. If that is OK, check the parameter for the stepper motor. On the control box, there are different pre-resistances. With these resistances, the power of the motor can be set. If that is working fine, check the tooth-wheel system between the objective and the stepper motor. If the big wheel hits the upper holder, the tooth-wheel is blocked. Turning the tooth-wheel carefully into a lower position by hand, or loosening the screw on the objective holder and pushing down the tooth-wheel, solve the problem. If everything appear normal, check for broken cable. At low temperature, the movement of the objective can be checked by looking through the windows into the cryostat and check the turning of the objective from below. If it does not turn, check the control box and the settings for the pre-resistances. If nothing helps and the cable connections on the outside seem fine, the setup has to be warmed up.

3. tip approach
   The approach of the tip is very delicate. The tip gets stuck quite often at certain positions. At room temperature, the position of the magnet at the back of the tip holder can be changed (changing the attraction towards the shear piezos). Additionally, the sapphire balls and the sliding surface of the tip holder can be cleaned again. The driving voltage can be also increased to such a value, that movement is always possible. At low temperature, not much can be done. One trick is, to try a series of quick changes between upwards and downwards movements. After a few circles, the tip might move up and down again. Also driven the objective up and down a few times might help. The vibrations from the stepper motor are quite strong and they might loosen the tip or the tip might slip over the blocking position. Otherwise, the setup has to be warmed up again.

4. tip positioning
   The positioning of the tip over the objective is also quite delicate. If the gliding surface of the sapphire plates or the sapphire balls are not clean enough, it can happen that the tip gets stuck during the vertical position of the tip. At room temperature, they can be cleaned again with lind-free tissue and ethanol. Sometimes, the sapphire balls on the shear piezos reach the rim of the sapphire plates. At room temperature, a turning by hand is possible. At low temperature, moving the tip into another direction and trying to approach from a different side, might solve the problem. Sometimes, a fast up and down movement of the objective, causing a jump of the tip-setup might also help. Do not forget to put the tip into a save distance position first! Otherwise a warm-up is necessary. The last possibility is, that the shear-piezos have an electrical short-

cut or are operated under low vacuum conditions due to a liquid helium-level drop. At low temperatures, this can be seen, by looking from below through the windows into the cryostat and moving the shear-piezos. If a flash or a shining appear, it is apparent, that the voltage is discharged by a light-bow. Only a warm-up can solve the problem.

5. cryostat
The cryostat itself has been the source of many problems. Leaks appeared, especially at the indium seals of the windows. A leak in the cryostat can be detected at room temperature by a drop of the pressure in the outer vacuum when the inner chamber is evacuated. This is a sign of a very large leak which is located to 99% at the window which is in direct contact to the liquid helium. Another sign for a leak is an increase of the pressure of the outer vacuum when liquid helium is filled into the inner chamber. Most probably, the leak is smaller (if not already detected at room temperature), but is also located at the inner window seal. Last but not least, if the outlet line of the liquid helium chamber (to the helium bath pump) gets frozen soon after the start of transfer of liquid helium, there is a problem with the transfer. It can be a large heating source inside the cryostat, or (what happened only once) there is a leak in the transfer-line itself. Leaks at the window seals can be fixed, by taking the cryostat apart. The inner chamber can be taken out and turned upside down (after the cup on top is put on). The inner chamber can be evacuated by connecting it to a leak checker. Using helium gas (hose with a very fine needle), all rims and joints can be checked (starting from the top!). Most probably, the leak is located at the inner window! The window can be taken out and replaced by a fresh seal of indium. Best results have been obtained by a tightening procedure over three days. Every 2-3 hours, the screws are tighten slightly and always by tightening cross-wise (opposite sides). In this way, the indium seal is pressed down very slowly and homogeneously.

B.2   Artefacts in the fluorescent pattern

There are a two artefacts, appearing in the fluorescence pattern of the spatial tip-scan. One is a very high-fluorescent feature, which does not react on the change in the laser frequency or the tip voltage. This feature is a very round fluorescent circle, shown in Fig. B.1 (a). It only moves, when the tip is moved within the laser focus. This feature appears, when the tip is broken. Laser light is coupled into the tip (very effectively, if the broken surface at the tip is very smooth), and the signal collected is very high fluorescent (much higher, than from a molecule). In that case, the setup has to be warmed up and the tip has to be exchanged.

Another feature has been detected quite often, when the voltage on the tip has been comparable high and the tip has been close to the molecule. In this configura-
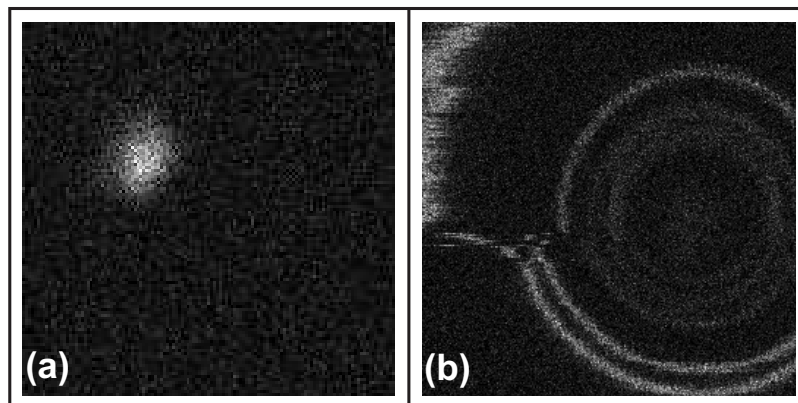
Figure B.1: Artefacts in the fluorescent pattern. (a) Highly fluorescent, round feature appears, if the tip is crashed. (b) Spectral instabilities of the molecule are induced during the tip scan, if the gap-width is small and the voltage on the tip is high ($V \sim 180$ V for this scan).

tion, the interaction between the electric field from the tip and the molecule causes spectral instabilities, shown in Fig. B.1 (b). The molecule becomes unstable, as soon as the tip moved closer to the molecule within on tip-scan. This effect can be avoided by reducing the tip-voltage.

Bibliography

[1] W. Moerner and L. Kador, Phys. Rev. Lett. **62**, 2535 (1989).

[2] M. Orrit and J. Bernard, Phys. Rev. Lett. **65**, 2716 (1990).

[3] W. Ambrose and W. Morner, Nature **349**, 225 (1991).

[4] S. Weiss, Science **283**, 1676 (1999).

[5] S. Weiss, Nature **7**, 724 (2000).

[6] G. Binnig and H. Rohrer, Rev. Mod. Phys **59**, 615 (1987).

[7] G. Binnig, C. Quate, and C. Gerber, Phys. Rev. Lett. **56**, 930 (1986).

[8] T. Basché, T. Kummer, and C. Bräuchle, Nature **373**, 132 (1995).

[9] M. Bopp, A. Meixner, G. Tarrach, I. Zschokke-Gränacher, and L. Novotny, Chem. Phys. Lett. **263**, 721 (1996).

[10] J. Skinner and W. Moerner, J. Phys. Chem. **100**, 13251 (1996).

[11] T. Basché, W. Moerner, M. Orrit, and H. Talon, Phys. Rev. Lett. **69**, 1516 (1992).

[12] T. Plakhotnik, E. Donley, and U. Wild, Annu. Rev. Phys. Chem. **48**, 181 (1997).

[13] F. Kulzer, S. Kummer, R. Matzke, C.Bräuchle, and T. Basché, Nature **387**, 688 (1997).

[14] J.-M. Segura, G. Zumofen, A. Renn, B. Hecht, and U. Wild, Chem. Phys. Lett. **340**, 77 (2001).

[15] C. Hettich, C. Schmitt, J. Zitzmann, S. Kühn, I. Gerhardt, and V. Sandoghdar, Science **298**, 385 (2002).

[16] U. Wild, F. Güttler, M. Pirotta, and A. Renn, J. Lumin. **60-61**, 1003 (1994).

[17] M. Orrit, J. Bernard, A. Zumbusch, and R. Personov, Chem. Phys. Lett. **196**, 595 (1992).

[18] M. L. Pirotta, *Optical Spectroscopy On Single Perylene Molecules In N-Nonane* (Diss. ETH Zürich No. 11887, 1996).

[19] C. Brunel, P. Tamarat, L. Lounis, J. Woehl, and M. Orrit, J. Phys. Chem. A **103**, 2429 (1999).

[20] W. Moerner, T. Plakhotnik, T. Irngartinger, U. Wild, D. Pohl, and B. Hecht, Phys. Rev. Lett. **73**, 2764 (1994).

[21] P. Bordat, M. Orrit, R. Brown, and A. Würger, Chem. Phys. **258**, 63 (2000).

[22] U. Wild, F. Güttler, M. Pirotta, and A. Renn, Chem. Phys. Lett. **193**, 451 (1992).

[23] T. Latychevskaia, A. Renn, and U. Wild, Chem. Phys. **282**, 109 (2002).

[24] M. Steiner, F. Schleifenbaum, C. Stupperich, A. Failla, A. Hartschuh, and A. Meixner, Chem. Phys. Chem. **6**, 2190 (2005).

[25] T. Basché, W. Moerner, M. Orrit, and U. Wild, *Single-Molecule Optical Detection, Imaging and Spectroscopy* (VCH Weinheim, Germany, 1997).

[26] L. Novotny and B. Hecht, *Principles of Nano-Optics* (Cambridge University Press, 2006).

[27] M. Orrit, J. Bernard, and R. Personov, J. Phys. Chem. **97**, 10256 (1993).

[28] E. Betzig and R. Chichester, Science **62**, 1422 (1993).

[29] W. Moerner and M. Orrit, Science **283**, 1670 (1999).

[30] X. Xie and J. Trautmann, Annu. Rev. Phys. Chem. **49**, 441 (1998).

[31] P. Tamarat, A. Maali, B. Lounis, and M. Orrit, J. Phys. Chem. A **104**, 1 (2000).

[32] F. Kulzer and M. Orrit, Ann. Rev. Phys. Chem. **55**, 585 (2004).

[33] A. Müller, W. Richter, and L. Kador, Chem. Phys. Lett. **241**, 547 (1995).

[34] S.Kummer, S. Mais, and T. Basché, J. Chem. Phys. **99**, 17078 (1995).

[35] K. Rebane and I. Rebane, J. Lumin. **56**, 39 (1993).

[36] K. Rebane, Chem. Phys. **189**, 139 (1994).

[37] H. Haken and H. Wolf, *Molekülphysik und Quantenchemie* (Springer Verlag, 4th edition, 2003).

[38] A. Lieb, *Mikroskopie mit Parabolspiegeloptik* (Diss. Universität Siegen, 2001).

[39] R. Loudon, *The Quantum Theory of Light* (Oxford University Press, 1983).

[40] A. Stoneham, Rev. Mod. Phys. **41**, 82 (1969).

[41] L. Kador, J. Chem. Phys. **95**, 5574 (1991).

[42] D. Orth, R. Mashl, and J. Skinner, J. Phys. Cond. Mat. **5**, 2533 (1993).

[43] W. Moerner and T. Carter, Phys. Rev. Lett. **59**, 2705 (1987).

[44] T. Carter, M. Manavi, and W. Moerner, J. Chem. Phys. **89**, 1768 (1988).

[45] H. Carmichael and D. Walls, J. Phys. B **9**, L43 (1976).

[46] B. Kohler and J. Woehl, J. Chem. Phys. **102**, 7773 (1995).

[47] M. Stepen, J. Phys. Chem. **40**, 669 (1964).

[48] J. Jackson, *Klassische Elektrodynamik* (Walter de Gruyter & Co., 2nd edition, 1993).

[49] U.Akram, Z. Ficek, and S. Swain, Phys. Rev. A **62**, 013413 (2000).

[50] Y. Jung, E. Barkai, and R. Silbey, J. Chem. Phys. **117**, 1080 (2002).

[51] E. Barkai, Y. Jung, and R. Silbey, Ann. Rev. Phys. Chem. **55**, 457 (2004).

[52] A. Heuer and R. Silbey, Phys. Rev. Lett. **70**, 3911 (193).

[53] D. Dab, A. Heuer, and R. Silbey, J. Lumin. **64**, 95 (1995).

[54] P. Anderson, Philos. Mag. **25**, 1 (1972).

[55] W. Phillips, J. Low Temp. Phys. **7**, 351 (1972).

[56] E. Geva, P. Reilly, and J. Skinner, Acc. Chem. Res. **29**, 579 (1996).

[57] A. Naumov, Y. Vainer, M.Bauer, and L. Kador, J. Chem. Phys. **116**, 8132 (2002).

[58] M. Bauer and L. Kador, J. Chem. Phys. **118**, 9069 (2003).

[59] M. Bauer, L. Kador, A. Naumov, and Y. Vainer, J. Chem. Phys. **119**, 3836 (2003).

[60] M. Bauer and L. Kador, J. Lumines. **107**, 32 (2004).

[61] E. Geva and J. Skinner, J. Chem. Phys. B **101**, 8920 (1997).

[62] E. Geva and J. Skinner, J. Chem. Phys. **109**, 4920 (1998).

[63] W. Ambrose, T. Basché, and W. Morner, J. Chem. Phys. **95**, 7150 (1991).

[64] R. Webb, Rep. Prog. Phys. **59**, 427 (1996).

[65] J.-M. Segura, *Scanning Confocal Optical Microscopy Of Single Molecules At Low Temperatures* (Diss. ETH Zürich No. 13795, 2000).

[66] A. Kramer, J.-M. Segura, A. Hunkeler, A. Renn, and B. Hecht, Rev. Sci. Instrum. **73**, 2937 (2002).

[67] P. Günther, U. Fischer, and K. Dransfeld, Appl. Phys. B **48**, 89 (1989).

[68] K. Karrai and R. Grober, Appl. Phys. Lett. **66**, 1842 (1995).

[69] J. Rychen, T. Ihn, P. Studerus, A. Herrmann, K. Ensslin, H. Hug, P. van Schendel, and J. Güntherodt, Rev. Sci. Instr. **71**, 1695 (2000).

[70] A. Ruiter, J. Veerman, K. van der Werf, and N. van Hulst, Appl. Phys. Lett. **71**, 28 (1997).

[71] A. Ruiter, J. Veerman, K. van der Werf, M. Garcia-Parajo, W. Rensen, and N. van Hulst, Ultramicroscopy **71**, 149 (1998).

[72] W. Atia and C. Davis, Appl. Phys. Lett. **70**, 405 (1997).

[73] J.-M. Segura, A. Renn, and B. Hecht, Rev. Sci. Instrum. **71**, 1706 (2000).

[74] P. Bordat and R. Brown, J. Chem. Phys. **116**, 229 (2002).

[75] P. Bordat and R. Brown, Chem.Phys.Lett **331**, 439 (2000).

[76] A. Müller, W. Richter, and L. Kador, Chem. Phys. Lett. **285**, 92 (1998).

[77] G. Harms, T. Irngartinger, D. Reiss, A. Renn, and R. Wild, Chem. Phys. Lett. **313**, 533 (1999).

[78] F. Kulzer, R. Matzke, C.Bräuchle, and T. Basché, J. Phys. Chem. A **103**, 2408 (1999).

[79] F. Kulzer, R. Matke, C. Bräuchle, and T. Basché, J. Phys. Chem. A **103**, 2408 (1999).

[80] S. Kummer, T. Basché, and C. Bräuchle, Chem. Phys. Lett. **229**, 309 (1994).

[81] S.Kummer, R. Kulzer, R. Kettner, T. Basché, C. Tietz, C. Glowatz, and C. Kryschi, J. Chem. Phys. **107**, 7673 (1997).

[82] F. Kulzer, F. Koberling, T. Christ, A. Mews, and T. Basché, Chem. Phys. Lett. **247**, 23 (1999).

[83] R. Lechner, B. Toudic, and H. Cailleau, J. Phys. C: Solid State Phys. **17**, 405 (1983).

[84] P. Bordat and R. Brown, Chem. Phys. **246**, 323 (1999).

[85] G. Wright, Proc. Phys. Soc. B **68**, 701 (1955).

[86] J. Sepiol, J. Jasny, J. Keller, and U. Wild, Chem. Phys. Lett. **273**, 444 (1997).

[87] J. Meyling, P. Bounds, and R. Munn, Chem. Phys. Lett. **51**, 234 (1977).

[88] G. Hoheisel, E. Heinecke, and A. Hese, Chem. Phys. Lett. **373**, 416 (2003).

[89] G. Hoheisel, *Hochauflsende Laserspektroskopie mittels optisch-optischer Doppelresonanz an Pentacen und laserinduzierter Fluoreszenz an Terrylen* (Diss. Technische Universität Berlin, 2004).

[90] H. Bach, *Spectral dynamics of single molecules* (Diss. ETH Zürich No. 12934, 1998).

[91] F. Güttler, M. Croci, A. Renn, and U. Wild, Chem. Phys. **211**, 421 (1996).

[92] R. Pfab, J. Zimmermann, C. Hettich, I. Gerhardt, A. Renn, and V. Sandoghdar, Chem. Phys. Lett. **387**, 490 (2004).

[93] R. Stöckle, C. Fokas, V. Deckert, R. Zenobi, B. Sick, B. Hecht, and U. Wild, Appl. Phys. Lett. **75**, 160 (1999).

[94] W. Greiner, *Klassiche Elektrodynamik* (Verlag Harri Deutsch, 5th edition, 1991).

[95] C. Cohen-Tannoudji, J. Dupont-Roc, and G. Grynberg, *Atom-Photon Interaction* (John Wiley & Sons, New York, 1992).

[96] M. Scully and M. Zubairy, *Quantum Optics* (Cambridge University Press, 1997).

[97] M. Kreiter, M. Prummer, B. Hecht, and U. Wild, J. Chem. Phys. **117**, 9430 (2002).

[98] S. Sekatskii, M. Chergui, and G. Dietler, Europhys. Lett. **63**, 21 (2003).

[99] S. Sekaktskii, Phil. Trans. R. Soc. Lond. A **362**, 901 (2004).

[100] G. Agarwal and S. Gupta, Phys. Rev. A **57**, 667 (1998).

[101] R. Tanaś and Z. Ficek, Fortschr. Phys. **51**, 230 (2003).

Curriculum Vitae

Senta Karotke
Born on September 17th 1975 in Göttingen , Germany

Studies

10/2001 - 03/2006	Phd thesis in the group of Prof. Bert Hecht at the University of Basel, Switzerland
	Title of the Phd thesis: Stark shift microscopy: interaction of a confined electric field with single emitters
03/2000 - 07/2001	Postgraduate studies and Diploma thesis in the group of Prof. Steven Anlage, University of Maryland, USA, in cooperation with the group of Prof. Helmut Wühl, Forschungszentrum Karlsruhe
	Title of the Diploma thesis: 'High frequency conductivity of superconductive Ca-doped NBCO and YBCO single crystal'
10/1995 - 07/2001	Studies in Physics at the University of Karlsruhe, Germany
08/1987 - 07/1995	Gymnasium in Karlsruhe, Germany

Appointments

10/2001 - 09/2004	lecture assistant at the University of Basel, Switzerland
01/2000 - 06/2001	research assistant at the University of Maryland, USA
02/1998 - 10/1999	research assistant in the group of Prof. Zum Gahr at the Forschungszentrum Karlsruhe, Germany

Publication

S. Karotke, A. Lieb, and B. Hecht, *Stark shift microscopy of single emitters*, Appl. Phys. Lett. **89**, 023106 (2006)

The following Professors have contributed to my eduction:
Basel: B. Hecht, D. Pohl, C. Schönenberger, H.-J. Güntherodt
Maryland: S. Anlage
Karlsruhe: M. von Renteln, M. Wegener, J. H. Kühn, Zum Gahr, W. Hollik, H. Wühl, D. Gerthsen, H. Kalt, K. Grüner, H. Genz, G. Schön, C. Klingshirn, K.-H. Kampert, R. von Baltz, P. Wölfle